Modelling of High Voltage Circuit Breakers Considering Interaction between the Driving Mechanisms and Switching Arcs

Thesis submitted in accordance with the requirements of the University of Liverpool for the degree of Doctor in Philosophy

by

Kun Cao

June 2018

Department of Electrical Engineering and Electronics
The University of Liverpool

Acknowledgement

Upon completion of this PhD thesis, I would like to take this opportunity to show my appreciation to people without whom this whole endeavour would surely be disastrous.

Firstly, my sincerest appreciation goes to my supervisor, Professor J D Yan, for his invaluable insights, encouragements and support. I'm deeply honored to have been his student and will forever be grateful.

I would like to express my gratitude to Pinggao Electrical Co. Ltd, the collaborator of this research project, for providing much needed information and support. My gratitude also goes to Dr L Jiang and Professor J W Spencer, who have provided me with guidance and training in abundance.

My warmest and dearest thank you goes to my family and all my friends. Each one of them played an incredible and irreplaceable role in my life and all their love shine like bright beacons, guiding me through the dark and rough sea.

My deepest love and gratitude belong to my girlfriend, Miss X Chen and I would like to say to her: "although you weren't here at the beginning, words cannot describe how happy I am that you are here in the end."

Abstract

With the increase of voltage and current ratings, design and test of circuit breakers have become more demanding. This is a consequence of the technical difficulties and costs in performing development tests as well as the complexity resulting from the coupling of different physical mechanisms in shaping the interruption performance of a breaker. It is well known that the performance of a circuit breaker is determined by many design and operational parameters among which the motion characteristic of the contact is a key factor. Since the motion characteristic of the contacts has a direct impact on breaker performance, it plays a critical role in the design of a circuit breaker.

Difficulties in performing tests or experiments under high voltage and power have rendered the traditional ‘cut and try’ design approach impractical. Computer simulation on the other hand, with its cost-effective and easy-to-implement nature, has become the favored approach to achieve design optimization and attracted a great amount of attention in the field of electrical engineering. An arc simulation model (Liverpool arc model) has been developed in this research group together with a circuit breaker simulation interface, featuring PHEONICS as the differential equation solver. Valuable information can be extracted from arc simulation results and help design better optimized prototypes. However, the absence of a driving mechanism model in the current arc simulation model limits its effectiveness and functionality. The travel of the contact could affect the flow cross section in the arc chamber as well as the length of the arc, and ultimately the performance of the circuit breaker. Additionally, the interaction between the arc chamber and driving mechanism, which has a significant impact on the result (most prominent under high current and long arc duration), has also been overlooked in the existing model.

Previously, the absence of a driving mechanism model is dealt with by providing the simulation with a user-defined text file containing the travel profile of the moving

contact. However, a user defined file may not reflect the true motion of the moving contact due to the unaccounted interaction between the arc chamber and driving mechanism. Consequently, a truly coupled simulation model, which is capable of calculating the travel of all moving components in real time and eliminating any inaccuracies in the predefined travel curves, is needed.

In the current research, an approach to quantify the interaction between the arc and driving mechanism has been proposed. Collectively, the resistive force (known as reaction force) imposed on the moving components in the arc chamber by the high-pressure gas can be calculated by a newly developed integral method. The existing arc model has been expanded to incorporate the calculation of reaction force. In addition, a functional mathematical model for the ZF-11-252 (L)/CYTA hydraulic driving mechanism has also been developed, based on which a number of sensitivity studies have been carried out and the key design parameters that affect the dynamic characteristics of the driving mechanism identified.

Considering both the driving mechanism model and the improved arc model (which can now calculate reaction force based on the pressure distribution in the arc chamber) a coupled circuit breaker simulation procedure has been established together with an interface which facilitates the information exchange between the driving mechanism model and the arc model. Based on this coupled model, the interaction between the arc and the driving mechanism is studied under different arcing conditions and nozzle geometries. In particular, two important factors affecting the accuracy of the predicted travel characteristics of the moving components have been identified through the studies. The first one is the need to consider the variable contact surface area between the piston rod in the hydraulic cylinder and the oil as a result of the motion of the piston. The second factor is the prediction accuracy of the pressure field around the moving components in the arcing chamber, especially when there are strong pressure waves propagating in the arcing gas. These aspects have not been studied so far.

List of Figures

List of Tables

Table of Content

Chapter 1 Introduction

1.1 Circuit Breakers in Electrical Grids

The availability of electric energy is vital for the development of economy and the quality of daily life. According to the 60th anniversary edition of the Digest of United Kingdom Energy Statistics (DUKES) report [1], the consumption of electric power within the UK was steadily increasing in the past sixty years (1948-2008). Over the period 1948 to 2008, electricity supplied to the national grid has grown on average by around 4 per cent per year (from approximately 49 TWh in 1948 to approximately 370 TWh in 2008). One crucial condition for consumers to receive reliable electric power supply is a well-constructed and protected electrical grid. An electrical grid is often defined as an interconnected network for delivering electricity from producers to consumers. It consists of generating stations that produce electrical power, high voltage transmission lines that carry power from distant sources to demand centers, and distribution lines that connect individual end-users. Figure 1.1 illustrates the layout of a typical electrical grid with its sub-systems (generation, transmission and distribution networks) highlighted in different colors.

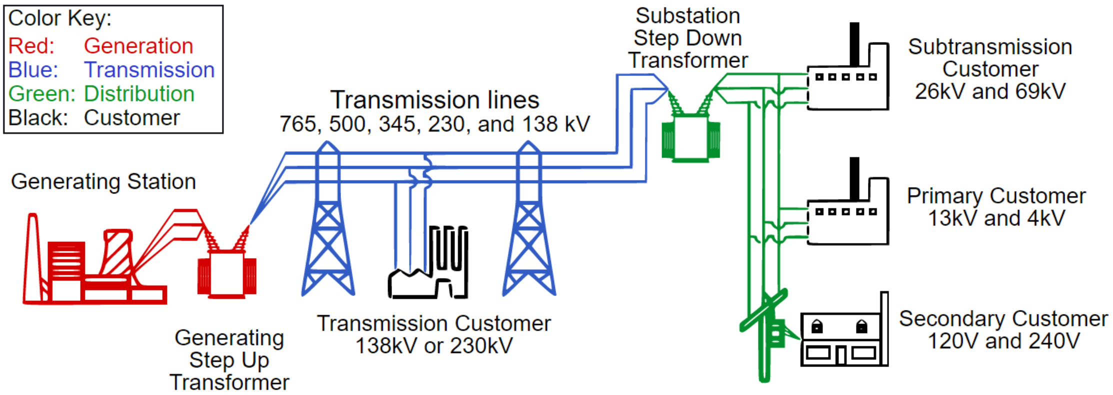

Figure 1.1 The layout of a typical electrical grid, including sub-systems such as generation, transmission and distribution networks are highlighted in different colours [2].

Such a system brings forward the need to stop the flow of current in the case of a fault occurring or maintenance of the system is required. A number of different types of switchgears have been designed to fulfill this need, including disconnector, load switch, fuse and circuit breakers. According to [3], the main difference between a circuit breaker and a generic switch is that a circuit breaker can interrupt a short-circuit fault current up to 80 kA, whereas a load switch cannot. Table 1.1 shows the different functionality of different types of switchgears.

Table 1.1 The required duty of different types of switching devices.

Device	Carry fault current	Make on fault	Break load current	Break fault current
Disconnector	yes	no	no	no
Load Switch	yes	yes	yes	no
Fuse	no	no	no	yes
Circuit Breaker	yes	yes	yes	yes

Table 1.1 indicates that circuit breakers have the most onerous duty to perform of any of the switching devices, in that it has to be capable of interrupting any current that may pass through it, up to its rated short-circuit breaking current. It must also be able to close on to the peak fault current and carry that fault current for a predetermined period of time [3]. Among all the tasks that a circuit breaker is responsible for, the interruption of short circuit current is the most challenging one. In the recent past years, due to the rapid increase of transmission voltage level as well as the capacity of the power grid, the difficulty in successfully interrupting short circuit current has increased tremendously. As a result, circuit breakers have become the most complex, expensive and indispensable among all switching devices and their reliability and performance are vital to the safe operation of electrical networks.

1.1.1 Short circuit current and transient recovery voltage

There are different fault conditions that give rise to various short circuit currents in a complex electrical grid. Figure 1.2 demonstrates a few potential fault scenarios that a circuit breaker has to deal with.

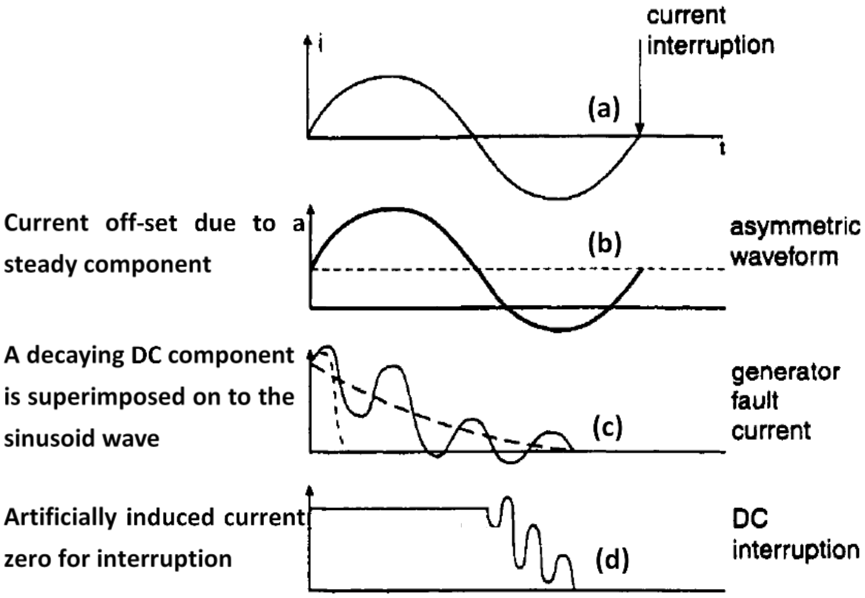

Figure 1.2 Different short circuit interruption scenarios: (a) symmetrical (b) asymmetrical (c) generator fault (d) DC interruption [4].

The simplest fault current regularly encountered by a circuit breaker is a power frequency symmetrical short circuit current (Figure 1.2 (a)). In this case, the rate of current decay before approaching current zero is relatively low. Therefore, the recovery voltage following current interruption, in this case, is also relatively low. In some other cases, the fault current may contain a steady component. As a result, the current waveform becomes asymmetrical (Figure 1.2 (b)). In the case of a generator fault, the sinusoidal power frequency wave is superimposed by an exponentially decaying component, which leads to the postponement of the current crossing its zero (Figure 1.2 (c)). All these cases above are in the scope of current interruption in AC systems. In DC systems on the other hand, an oscillation in arc current has to be artificially induced to force the current reaching zero (Figure 1.2 (d)).

The main factors that determine the magnitude and other important characteristics of a short circuit current are the capacity of the sources of current, the impedance of power sources, the characteristics of the portion of the circuit that is located between the source and the point of the fault and characteristics of the rotating machines (synchronous generators, induction and synchronous motors etc.) that are connected to the system at the time of the short circuit [5].

If current crossing zero is followed by a successful interruption, the circuit (including the external circuit which the circuit breaker is connected to) has effectively been reconfigured because the conducivity of the arc quenching medium has been reduced tremendously. As a result, a voltage is generated from the network onto the terminals of the circuit breaker as the result of energy oscillations between the energy storage elements of the network. The voltage across the breaker contacts that oscillates towards the power frequency system voltage via a transient period is called the transient recovery voltage [6].

The characteristic of the transient recovery voltage (TRV) is affected by the switching arrangement in which switches are enclosed in, or structurally associated with casings or enclosures, the type of fault as well as the characteristic of the electrical circuit, i.e., inductance, capacitance and resistance. Consequently, the TRV can have many complicated characteristics regarding its frequency response (single or double) and profile (sinusoidal, hyperbolical, saw-tooth, etc.).

It is worth noticing that based on the location of the fault, the voltage transients generated by a terminal fault (fault happens close to the circuit breaker, the reactance between the point of fault and the breaker can be ignored) and short line fault (point of fault is of some distance from the breaker, typically from a few hundred meters to tens of kilometers) are especially important. In the case of a terminal fault, the TRV has a single frequency response, and the maximum theoretical peak value of the TRV is twice the system voltage. However, in real systems the resistive components in the circuit will provide some level of damping so that the peak value of the TRV never exceeds the theoretical cap (when considering a single phase). This is demonstrated by Figure 1.3.

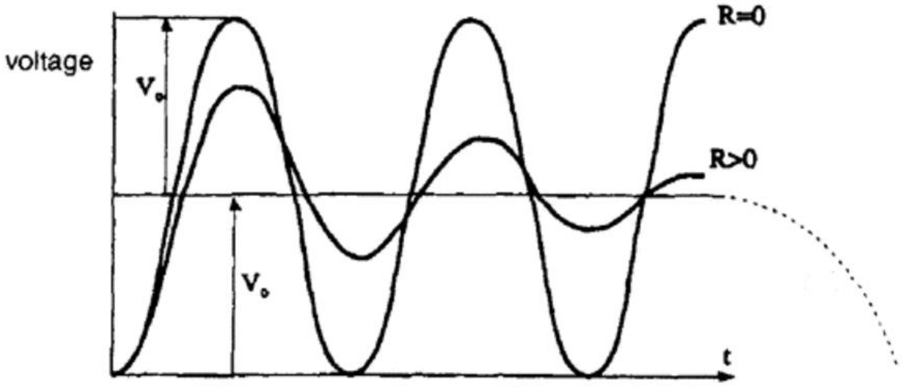

Figure 1.3 Recovery voltage induced by a terminal fault which occurs close to a circuit breaker terminal [4].

When considering TRV in three-phase networks, several types of short-circuits may occur: single-phase to earth; two-phase, with or without earth connection; and three-phase, with or without earth connection. Three-phase short-circuits are very rare but lead to the most severe stresses on the circuit breakers. Therefore, the TRV voltage values used for type testing are based on three-phase faults [7]. When interrupting a circuit with three phases, each of the three phases clears their respective current zero. While one phase is cleared first, the other two phases continue to carry current and give rise to over-voltage across the contact gap of the first phase; this is known as the first pole to clear factor. Based on the assumption that three-phase faults involve earth, according to the international electrotechnical commission (IEC) [8], for medium voltage switchgears, depending on the rated voltage and whether the system is ineffectively or effectively earthed the first pole to clear factor is between 1.3 and 1.5.

In the case of a short line fort, the TRV has a double frequency response because it is the result of two separate voltage transients each associated with one side of the circuit breaker. The superimposition of the two transients results in the most onerous TRVs as illustrated in Figure 1.4.

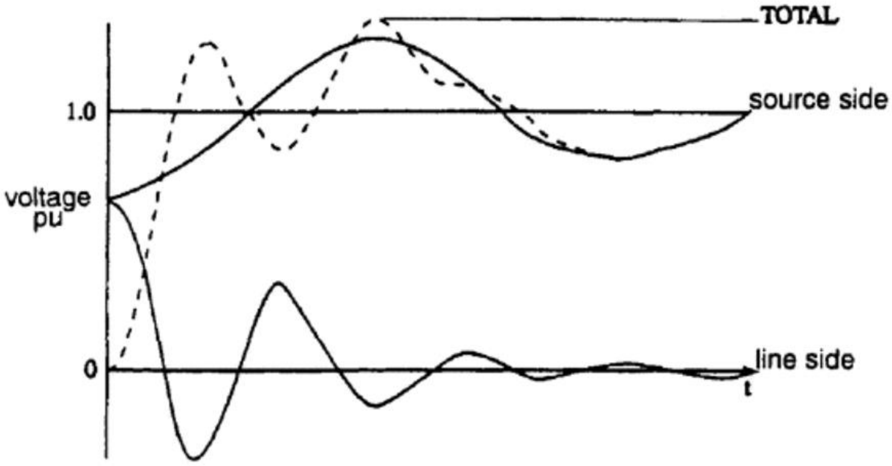

Figure 1.4 Recovery voltage induced by a short line fault which occurs some distance away from a circuit breaker terminal [4].

In circuit breaker testing, the maximum withstand voltage, the time to reach peak voltage and the critical rate of rise of recovery voltage (RRRV) are the most important factors regarding the TRV withstand capability of a circuit breaker. Figure 1.5 gives an example of the TRV waveform used in a short line fault test.

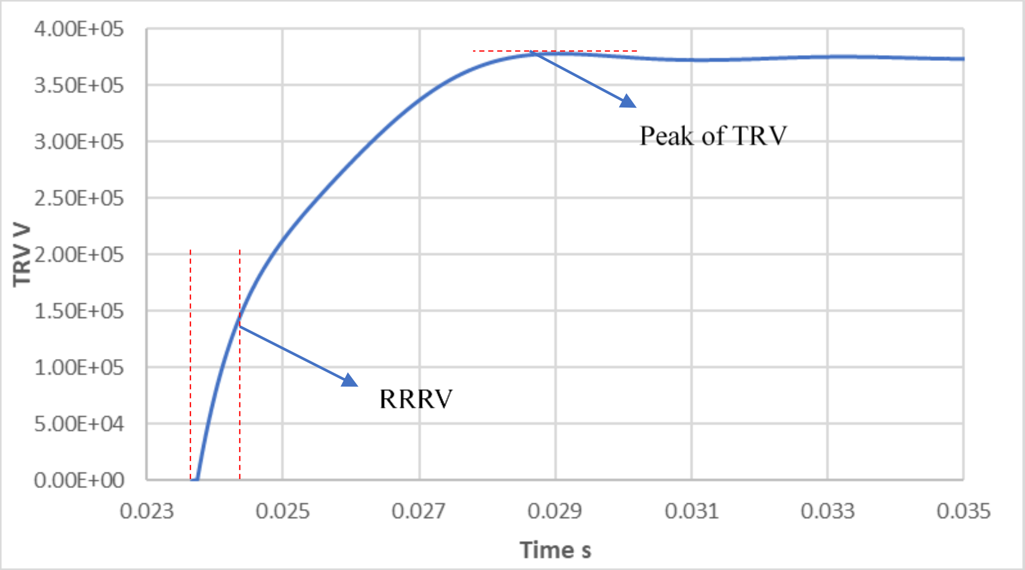

Figure 1.5 An example of the TRV waveform used in a short line fault test.

1.1.2 Thermal and dielectric recovery

Circuit interruption involving gas blast circuit breakers mainly consists of two aspects, namely the thermal and dielectric recovery processes. When a fault occurs, generally, a circuit breaker interrupts the fault current by mechanically separating a pair of conductor called “arc contacts”. Once the contacts are separated, an electric arc inevitably appears in the contact gap. Thermal recovery in its essence is the thermal energy removal mechanism immediately after current zero, such as convection and turbulence cooling, competing with the electric power input provided (Ohmic heating) to the arc. The thermal recovery process typically spans for tens of microseconds. When the arc is sufficiently cooled, the electric conductivity of the arcing medium becomes negligible. The dielectric recovery process begins. The dielectric recovery is mainly concerned with the removal of free electric charges in the contact gap. A successful dielectric recovery will allow the contact gap to gain enough dielectric strength and be able to withstand the transient recovery voltage without breaking down. A failure in dielectric recovery will allow the external electric field to accelerate remaining electrons and cause the gas to breakdown, leading to an interruption failure.

1.2 Different Types of Circuit Breakers

Although all circuit breakers share a similar working principle, details of their operations can vary substantially depending on the rating and type of the circuit breaker. The categorization of circuit breakers can be based on a number of different criteria, such as: location of installation, voltage rating, and most importantly, the method and medium used for arc quenching.

1.2.1 Oil circuit breakers

From a historical perspective, oil circuit breaker is the first practical design of a circuit breaker intended for high power applications. Refined petroleum oil had been used in almost all oil circuit breakers as the arc quenching medium. In the late 1920s, a study of the arcing process in oil was conducted at the Carville Power Station in the UK [9]. The study concluded that the arc quenching ability of the oil circuit breaker is mainly provided by the hydrogen gas generated by the decomposed oil molecules. Due to the low atomic weight, hydrogen molecules could travel at a very high velocity which is an effective way to remove thermal energy from the arc column.

1.2.1.1 Bulk oil circuit breakers (BOCB)

The main feature of the bulk oil circuit breaker is that the oil is not only used as an arc quenching medium but also an insulating medium, as a result, a large oil tank is often used to ensure the main contacts are completely submerged. Figure 1.6 shows the internal view of a typical bulk oil circuit breaker.

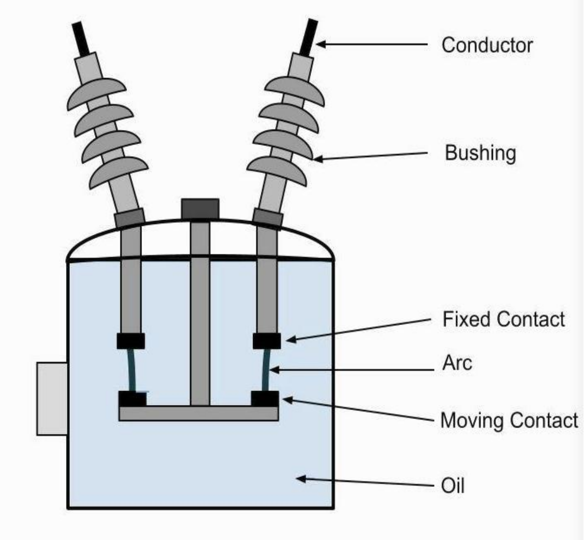

Figure 1.6 Internal schematic of a bulk oil circuit breaker.

When an arc is drawn between the contacts, the surrounding oil is quickly vaporized and decomposed, a gas bubble that consists mainly of hydrogen is formed around the arc column as a result. The high-pressure hydrogen gas bubble created by the arc energy is advantageously used to confine, compress and cool the arc. After the arc has been extinguished, the gas bubble dissipates, oil in the container then fills the contact gap and acts as insulation.

1.2.1.2 Minimum oil circuit breakers (MOCB)

The large oil tank featured in bulk oil circuit breakers raises a few maintenance and safety issues. Firstly, oil in the tank must be replaced after a certain number of interruptions since the dielectric strength of oil deteriorates after being contaminated. Secondly, high short circuit current could lead to excessively high pressure in the oil tank, causing rupture or explosion. Finally, the dielectric capability of oil and the severe pressure rise during arcing have limited the practical voltage level of bulk oil circuit breakers to 275 kV.

In order to improve performance and reduce maintenance requirement, minimum oil circuit breaker was developed as an improvement upon the bulk oil circuit breaker. The main distinguishing feature of the minimum oil circuit breaker is that oil is only used for arc quenching so a considerable less amount of it is needed. Figure 1.7 shows the internal view of a typical minimum oil circuit breaker.

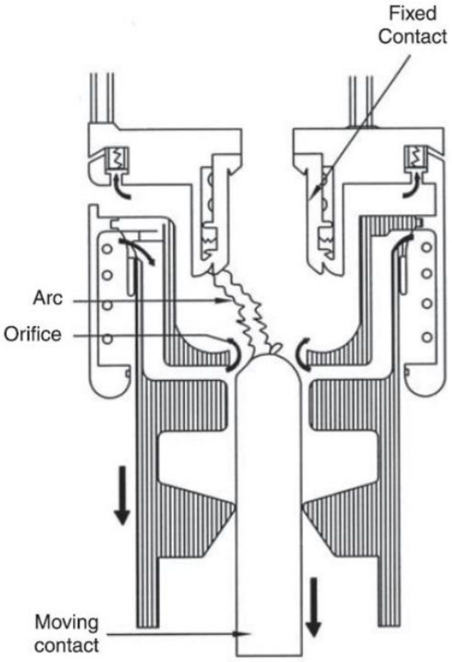

Figure 1.7 Internal view of the arc chamber of a minimum oil circuit breaker (axial venting).

To improve the interrupting performance, in most MOCB designs, oil is injected into the arc chamber. Hence, the hydrogen bubble formed by the vaporized oil is trapped inside the chamber. As the contacts continue to move, after a certain distance travelled, an exit vent becomes available for exhausting the trapped hydrogen gas. There are two different types of arcing chamber available in terms of how venting channel is oriented in the arcing chambers, namely the axial venting and radial venting orientations. The arc chamber shown in Figure 1.7 features an axial venting scheme.

1.2.2 Air circuit breakers

Due to its relatively good insulation properties under room temperature and atmospheric pressure, as well as its abundance in nature, air is one of the first arc quenching medium to be considered by engineers. A plain knife switch working in free air can be considered as the simplest air circuit breaker. However, due to the limited interrupting capability of such device, improved designs have been proposed, most notably among which are the arc chute and air-blast circuit breakers.

1.2.2.1 Arc chute circuit breakers

One of the earliest successful approaches to high power air circuit breakers was that developed by Slepian (1929) at Westinghouse, who recognized that below a certain voltage equal to the cathode voltage drop, an arc in air between two metal electrodes will extinguish automatically however small the gap and however large the current, provided melting and generation of metal vapor from the electrodes was not significant [10].

Based on this discovery, a design of arc chamber with a number of air gaps between flat metal plates (arc chutes) was developed. This design is mostly implemented within the low voltage range (<1 kV). The typical structure of the air chamber is illustrated in Figure 1.8.

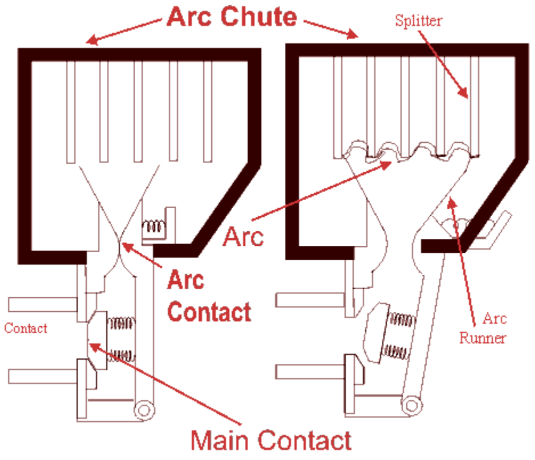

Figure 1.8 The arc chamber design of an arc chute type circuit breaker [48].

The arc chamber is designed in such a way that the arc will rise into the chutes due to heating and magnetic forces. Once the arc has been divided into segments, the total voltage drop across the arc increases, until it exceeds the system voltage and the arc becomes unsustainable and is subsequently extinguished.

1.2.2.2 Air blast circuit breakers

With the increase of rated voltage level, the requirement for the size of arc chute in arc chute circuit breaker is also elevated and the design inevitably becomes too bulky and impractical. Consequently, apart from the arc chute circuit breaker, other designs with air as interrupting medium had been attempted.

The first air blast circuit breaker was proposed at Electrical Research Association by Whitney and Wedmore in1926 [12]. The design was what’s known as an axial blast type interrupter which features a nozzle that is oriented along the axial direction. Later investigation of arc chambers with different blast configuration was carried out. Figure 1.9 demonstrates the difference between a number of blast configurations.

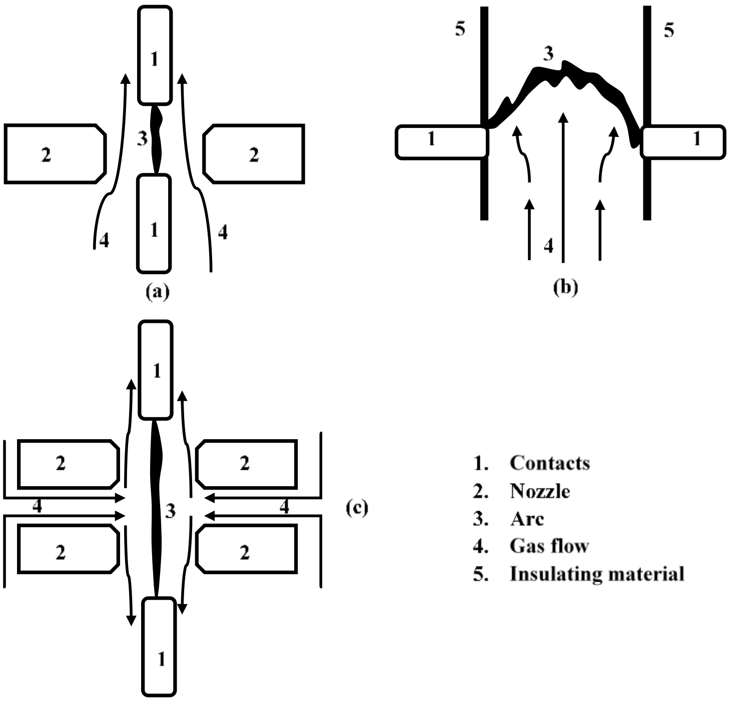

Figure 1.9 Different blast configuration of air blast circuit breakers: (a) axial blast, (b) radial blast, (c) cross blast.

Among all three blast configurations, the axial blast scheme (Figure 1.9 (a)) is the most commonly adopted one in high voltage applications. Often a converging-diverging nozzle made from insulating material (mostly polytetrafluoroethylene (PTFE)) is used to generate and direct gas flow towards the arc. Since the convective effects of an imposed flow field have a great impact on the overall arc behaviour [13], a strong and correctly timed gas flow plays an important role in arc cooling when arc current crosses zero. Tasked with both separating the contacts and generating the gas flow, driving mechanisms coupled to this type of arc chamber generally have a very high output.

1.2.3 Vacuum circuit breakers

Being devoid of free charge carriers, a vacuum, in principle, is an ideal electrical insulating medium. Due to its excellent insulating capability, the vacuum has long been used as an insulating medium in circuit breakers. Generally, similar to other types of circuit breakers, vacuum circuit breaker interrupts a circuit by separating a pair of contacts. However, the difference being the contacts are installed in an enclosed vacuum. The arc is essentially burning in ionized metal vapour, which is supplemented by vaporized contact material. A successful interruption is achieved at current zero, when the metal vapour diffuses and the arc can no longer be sustained. Figure 1.10 presents the schematic of the interrupting chamber of a generic vacuum circuit breaker.

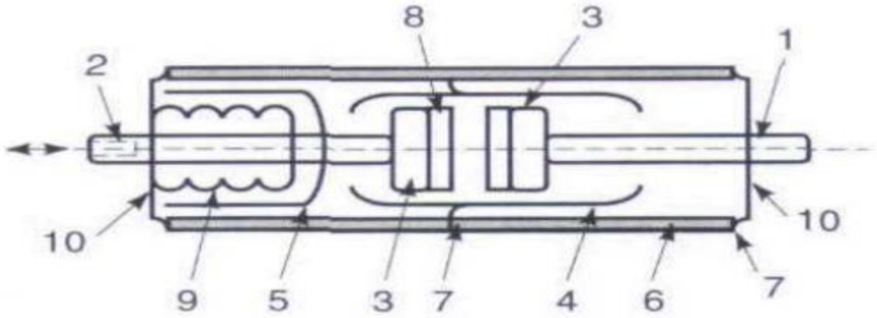

Figure 1.10 Interrupting chamber of generic vacuum circuit breaker with important components labelled: (1) fixed contact stem; (2) moving contact stem; (3) contact—arc-control geometry; (4) ion shield; (5) bellows shield; (6) ceramic or glass insulators; (7) ceramic [51].

Due to the simplicity in its design, the vacuum circuit breaker requires very little effort and attention in terms of maintenance. In addition, fewer parts in its design has led to outstanding reliability, as a result, vacuum circuit breaker has seen wide application in recent years.

1.2.4 SF_6 circuit breakers

The high dielectric strength of Sulfur hexafluoride (SF_6) mainly stems from its ability to form negative ions when collided with free moving electrons. In this process, a free electron moving in an external electric field, could potentially collide with a neutral SF_6 molecule and may be subsequently attached to this molecule and form a heavier negative ion. Under the same external electric field, compared with free electrons, heavy negative ions have more difficulty in gaining the kinetic energy required to cause further ionization. As a free electron removal mechanism, this process competes with collision ionization and gives SF_6 gas excellent dielectric strength. Electron attachment is a unique property of SF_6, it is either not observed in gases such as nitrogen, hydrogen and argon; or only to a very limited extent in gases such as oxygen and carbon dioxide [15]. Consequently, SF_6 has replaced air in gas-blast circuit breaker and gas insulated substations and become the dominant insulation material in the field of high voltage engineering.

1.2.4.1 Puffer type

The puffer type SF_6 beaker features an arc chamber that is similar to the axial air blast breaker. As shown in Figure 1.11, the puffer type arc chamber includes a stationary piston, a moving nozzle assembly and a pair of arcing contacts.

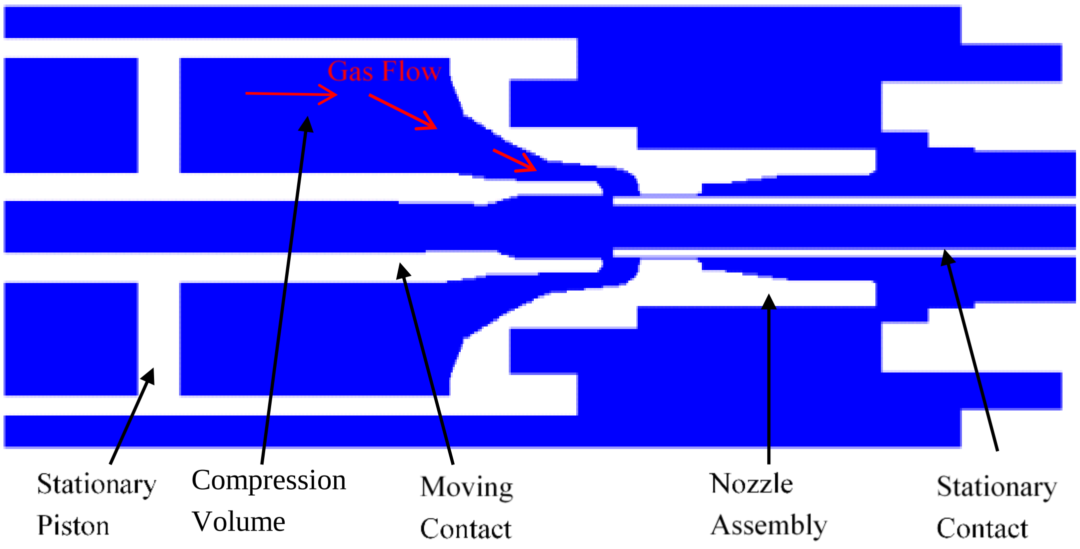

Figure 1.11 Typical structure of a puffer SF6 circuit breaker.

The moving contact and the main nozzle assembly are both connected to the driving mechanism via a linkage system, when in operation, the nozzle assembly is driven towards the stationary piston and gas flow is generated in the compression chamber.

The puffer type interrupter is intended for high-voltage switching, typically 145 kV and above, and is almost universally used at these voltages today [16]. Due to the high power and reliability requirement of this type of arc chamber, it is usually paired with hydraulic driving mechanisms, which will be introduced later in this chapter.

1.2.4.2 Self-blast type

Self-blast type interrupter has emerged as the main competitor to the technically more mature puffer circuit breakers. The main advantage of self-blast circuit breakers is that it utilizes the energy dissipated by the arc to create the required conditions for arc quenching during the current zero period and the subsequent dielectric recovery period. Thus, the energy required for the operating mechanism of a self-blast circuit breaker is much smaller than that of a puffer circuit breaker [17]. Figure 1.12 depicts the internal structure of a typical 145 kV self-blast interrupter.

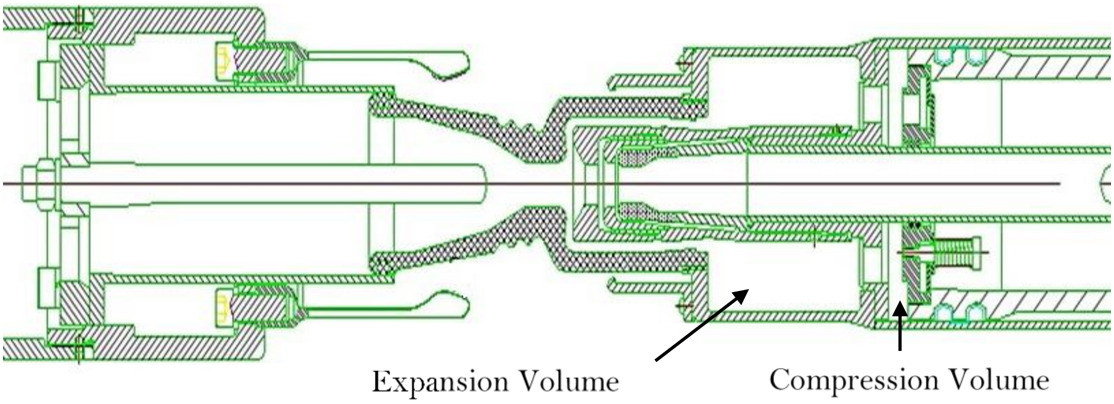

Figure 1.12 Typical structure of a 145 kV self-blast SF6 circuit breaker.

The introduction of the additional expansion volume allows the energy released by the arc to be utilized. The intense ohmic heating together with arc-induced nozzle ablation will cause the pressure inside the expansion volume to rise, combined with the compression motion, a high speed gas flow can be generated to achieve the desired arc quenching condition.

As mentioned earlier, the self-blast interrupter does not require as much operating power as the puffer type. Consequently, is it often coupled with spring driving mechanism. It is worth noticing that the forming of arc quenching condition in this type of interrupter depends heavily on the arcing history and some key design parameters (for example the geometrical shape of the main nozzle and the volume of expansion chamber). Thus, it is not as reliable as the conventional puffer type interrupter and its design has proven to be more difficult. These factors have prevented it from being used in the high and especially ultra-high voltage range. Nevertheless, there is a constant effort to increase the voltage rating of this type interrupter.

1.3 Different Types of Driving Mechanisms

The opening and closing operation of the circuit breaker is controlled by the driving mechanism. Upon receiving a command to close or open the circuit, the primary task of the driving mechanism is to accelerate the moving contact(s) and other moving components (such as the main nozzle assembly in a gas-blast circuit breaker) to a desired speed and reach the expected travel in time to create the optimum condition for arc quenching and provide insulation strength. The simple task of opening, closing and holding the contacts in a closed position can be quite demanding under extreme conditions. According to a CIGRE report, more than 40% of circuit breaker failure is originated from mechanical issues [18]. Consequently, the reliability and performance of the driving mechanism is a vital part of circuit breaker operation.

It is worth noticing that driving mechanism designs are often biased towards the opening operation. Since compared with the closing operation, opening the circuit creates more severe switching conditions and demands higher performance (in terms of opening time and contact speed). The timescale of the opening operation can vary due to different factors such as power frequency, contact release mechanism, total contact travel etc. Typically, the driving mechanism completes its operation within 3 to 5 current cycles (25 ms to 42 ms at 60 Hz and 30 ms to 50 ms at 50 Hz).

1.3.1 Hydraulic driving mechanism

The hydraulic driving mechanism features high reliability, stable and high-power output as well as low maintenance requirement due to its relatively simple design. As a result, it has been frequently paired with puffer type SF_6 arc chamber and seen wide application in high voltage transmission system (typically in the range of 500 to 1100 kV [19]).

The first hydraulic operating mechanism was invented by Perri to be used in monopole high voltage circuit breakers of 230 kV in the 1950s [20]. Although crude in its design, this system contains all important components like those used in a modern hydraulic driving mechanism. Shown Figure 1.13 is a hydraulic driving mechanism of modern design.

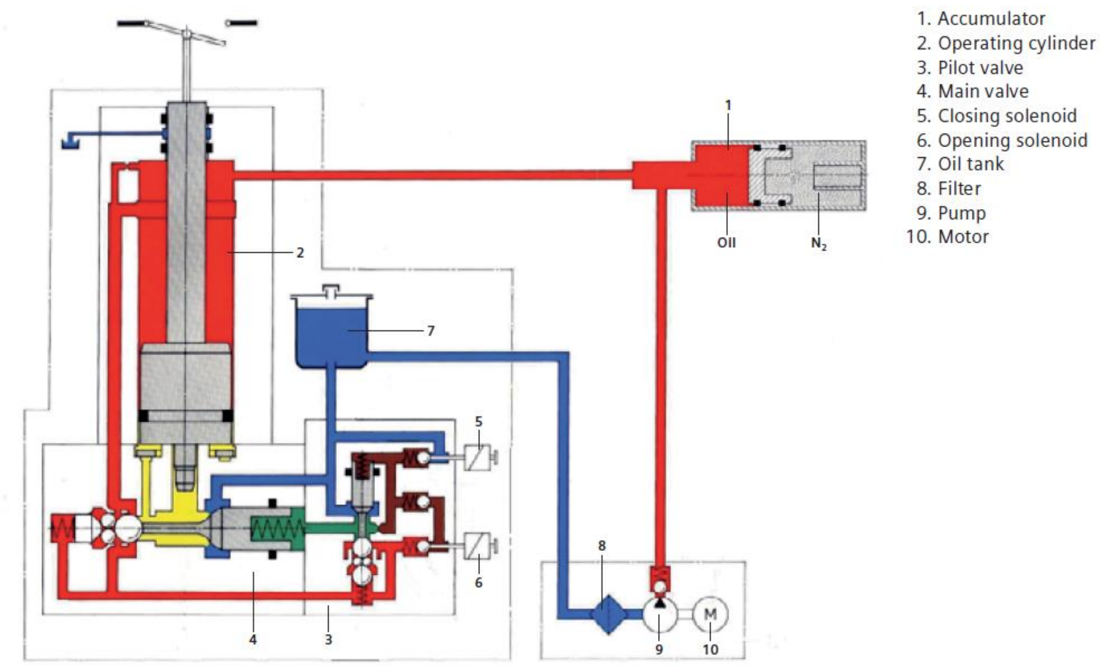

Figure 1.13 Schematic of a hydraulic driving mechanism with main components labelled [19].

The key component of the hydraulic driving mechanism of any design, is the main hydraulic cylinder, which is the main actuator in the system that converts hydraulic power into mechanical power. Its design parameters such as rated pressure and piston radius have a direct impact on the driving mechanism’s output. The operation of the cylinder is controlled by a directional valve (usually referred to as the main valve). Considering the high flow rate and fast operation time demanded by modern systems, additional control valves are sometimes introduced to form a tiered valve system. These additional valves are referred to as the pilot valves. As shown in 0, accumulators are often used to store energy in the form of fluid under pressure. This energy is in the form of potential energy of an incompressible fluid, held under pressure by an external source against some dynamic force. This dynamic force can come from three different sources: gravity, mechanical springs or compressed gases [21]. Aimed at preventing leakage and minimizing maintenance work, modern systems have increasingly opted for disc-springs to provide said dynamic force. In addition, an oil reservoir is installed in the system to store oil at low pressure. Finally, a hydraulic pump is used in conjunction with an electric motor to provide the accumulator with pressurized hydraulic fluid.

1.3.2 Spring driving mechanism

With the introduction of the self-blast breaker technology in the mid of the 80th which led to a reduction in switching energy required, the spring operating mechanisms are continuously replacing hydraulic and pneumatic operating mechanisms and are widely applied in the sub-transmission range (<200 kV) [22].

As the name suggests, spring driving mechanism utilizes springs as energy storage devices, usually there are separate springs dedicated to opening and closing operations. Figure 1.14 shows the schematic of a typical spring driving mechanism.

Upon receiving a command to open the circuit, a latch is released so the energy stored in the opening spring is transferred to other mechanical components and through the link formed by these components the moving contact is pulled away from the stationary one.

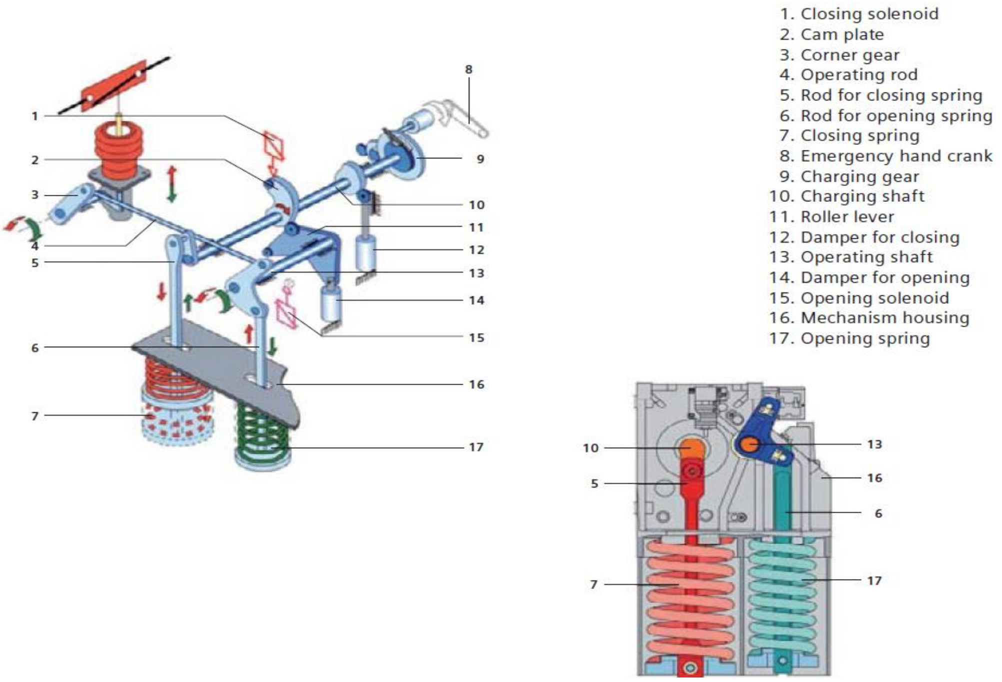

Figure 1.14 Schematic of a spring driving mechanism with main components labelled [19].

1.4 Introduction to Coupled Circuit Breaker Modelling and Simulation

The operation of a circuit breaker includes various aspects. In a typical operation, a number of mechanical (motion of the moving components, flow of the gas), electrical (the arcing process in the arc chamber), magnetic (Lorentz force on charged particles) and thermal (radiation in the arc core, re-absorption and nozzle ablation) processes are usually closely coupled. To accurately and comprehensively incorporate all these phenomena in a complete model is a challenging task. In addition, the recent expansion of ultra-high voltage transmission networks (with an 1100 kV AC transmission system in test operation in China, Japan and Russia are planning to build 1100 and 1150 kV system respectively) [23] indicates an increase in transmission system voltage and current ratings. As a result, the design and test of circuit breakers have become more difficult. The technical difficulties and high cost in performing development tests as well as the complex coupling of different physical mechanisms in shaping the interruption performance of a breaker have together made the traditional cut-and-try design approach impractical. On the other hand, computer simulation with its cost-effective and easy-to-implement nature, has become the favoured approach to achieve design optimization and attracted a great amount of attention in the field of electrical engineering. A truly coupled (incorporates both the arcing process, the operation of the driving mechanism and the interaction between the two) circuit breaker simulation package (based on a comprehensive model), capable of accurately predicting the performance of a prototype, is an invaluable tool for design engineers. Based on such simulation package, design optimization for a prototype breaker could be achieved with less investment in experiments and tests compared with the traditional cut-and-try approach.

Historically, a considerable amount of effort has been devoted to the study of arcing process in the arc chamber. An arc simulation model has been developed at Liverpool together with a circuit breaker simulation interface, featuring PHOENICS as the differential equation solver. Valuable information can be extracted from arc simulation results and help design better-optimized prototypes (explained in detail in Chapter 2). On the other hand, it is well known that the performance of a circuit breaker is determined by many design and operational parameters among which the motion characteristic of the contact is a key factor [24]. Motion of the moving contact as well as other moving components in the arc chamber is provided by the driving mechanism. As a result, the performance of the driving mechanism has a direct impact on the motion characteristic of the contact and it plays a critical role in the design of a circuit breaker.

Previously, the interaction between the driving mechanism and the arc is seldom considered in circuit breaker modelling [25][26][27]. While some focus on the steady cases (normally at a smaller scale than a full-size circuit breaker, for example in a supersonic nozzle) [26], there are other researches that managed to include the motion of moving objects in arc simulation. To incorporate moving components in circuit breaker simulation, it is a widely adopted approach to provide information regarding the travel profile of the moving components to the simulation in the form of a user-defined file [28]. The data is either obtained from measurement or given by the manufacturer of the driving mechanism. However, a fixed travel curve may not always reflect the true motion of the moving contact and any inaccuracies in the given data could be carried over to the simulation. It is known that as a result of the intense ohmic heating combined with other processes introduced by the arc (for instance nozzle ablation), the pressure field in the arcing chamber is drastically altered in the presence of a high fault current arc [29]. The pressurized gas will then act upon the moving components in the arc chamber, generating what is known as reaction forces. Because the moving components are connected to the driving mechanism, this reaction force is subsequently transmitted to the driving mechanism, altering its movement. It is also worth mentioning that the compression motion of the piston (driven by driving mechanism) located in the compression chamber also contributes to the change in pressure distribution. Collectively, the interaction between the moving components and the high-pressure gas results in a change of the speed of the moving components, which is more significant for high fault current amplitude, long arc duration cases. In addition, vaporization of the nozzle material often leads to changes in nozzle radius and surface condition. Apart from having an adverse effect on the longevity of the circuit breaker, this phenomenon also impacts the flow field and ultimately the interruption capability of the circuit breaker.

Figure 1.15 shows real examples of the nozzle surface condition after performing current interruption in experiments.

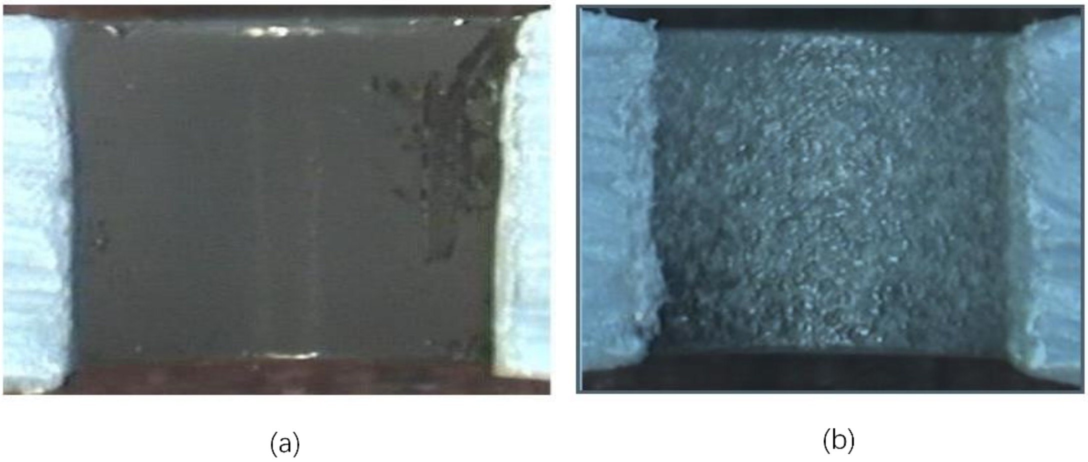

Figure 1.16 Pictures showing the surface conditions of a nozzle before (a) and after (b) current interruption [30].

The change of speed of the moving contact result in a smaller contact gap at current zero, this could in turn affect the circuit breaker’s ability to withstand the transient recovery voltage. However, pre-determined travel cannot account for this interaction. In addition, a single set of travel needs adjustment if the arcing condition is changed from that of the measurement. Furthermore, recently there’s increasing research effort in developing SF_6-free circuit breakers based on CO_2 mixtures [31][32]. There is test result showing that due to the high pressure rise in the compression chamber, the contact sometimes reverses its direction of travel, severely degrading the interruption capability. This is a new challenge that the design engineers need to address.

Despite being overlooked, this interaction does have a significant impact on the dynamic characteristics of the driving mechanism. To demonstrate the necessity of this, the comparison between two travel curves for a self-blast type circuit breaker measured under no-load and high current (50 kA) conditions is presented in Figure 1.17.

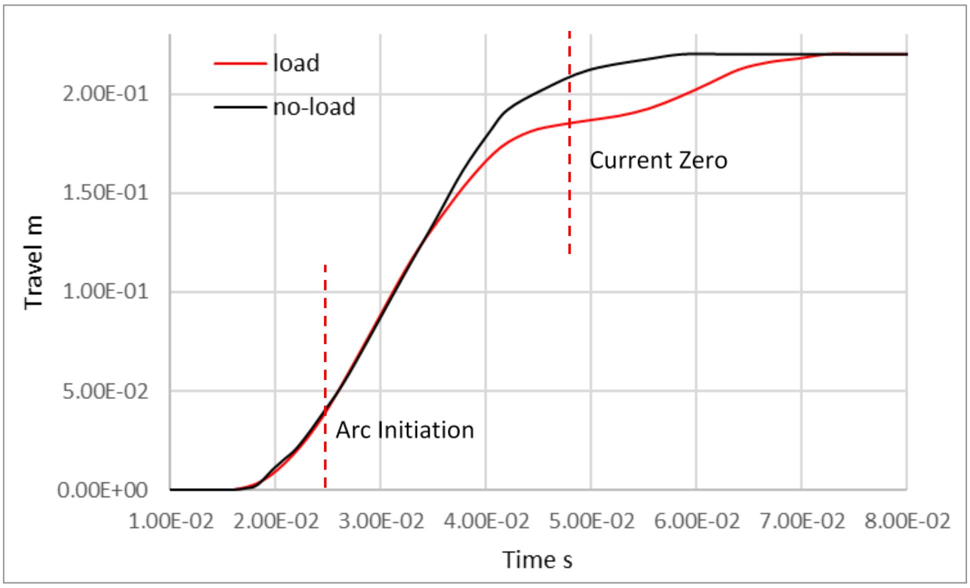

Figure 1.17 Travel curves for a 252-kV puffer circuit breaker measured under no-load and high current (50 kA) conditions.

It can be clearly observed that after arc initiation, the measured travel curves start to differ. Due to the absence of arcing in the no-load case, the discrepancy between the two travel curves can be attributed to the arc-induced pressure variation in the arc chamber. At this point, it is clearly demonstrated that the operation of the driving mechanism and the arcing process are closely coupled. Interactions between the driving mechanism and the arc will indeed affect the performance of the breaker. The absence of this interaction between the arc and driving mechanism in the existing simulation implies that:

a) the user specified travel may not reflect the true dynamic motion characteristics of the moving components when simulating different test duties, thus leading to inaccuracies in the prediction of the flow field, arc behaviour and interruption performance of the breaker.
b) it is not possible to take into account of the reaction force from the arcing chamber in the design and optimization process of the mechanical characteristics of the driving mechanisms.
c) the effectiveness and usefulness of the simulation are not maximally explored.

To sum up, without the dynamic coupling of the driving mechanism and arc model, inherent error embedded in the measured travel curves will be carried over to the simulation. In addition, the impact of Ohmic heating and nozzle ablation on pressure distribution in the arc chamber cannot be accounted for. Together, these inaccuracies could then lead to erroneous prediction of flow field, arc behavior and ultimately the performance of the circuit breaker.

To overcome these drawbacks, a model based on the real driving mechanism which is capable of calculating the instantaneous travel of the moving components as well as receiving and responding to the pressure change in the arc chamber is needed. A comprehensive arc model which considers all processes that affect the pressure distribution in the arc chamber and is capable of predicting the interrupting capability of a breaker is another crucial piece in coupled circuit breaker simulation. Moreover, since the driving mechanism model is independent of the arc model, an interface is needed to bridge the two solvers (solvers for driving mechanism model and arc model).

Few attempts have been made to develop a truly coupled circuit breaker model by solving the governing equations of the arc and driving mechanism concurrently. Literature regarding this topic is scarce. Two main shortcomings can be spotted among the majority of previous works:

a) Oversimplified arcing processes or driving mechanism models that lead to inaccuracy in arc chamber pressure and contact travel prediction.
b) Failure in showing the impact of arc-driving mechanism interaction on circuit breaker performance, thus, providing less useful guidance in terms of circuit breaker design.

For example, in [33], the opening process of an ultrahigh-voltage GIS circuit breaker equipped with a spring driving mechanism was modelled. Despite the real breaker having a fairly complicated arc chamber geometry, the model arc chamber simply includes a moving and a stationary component, forming a simple puffer cylinder. The moving part of the arc chamber was connected directly to the spring driving mechanism, together with the stationary part, they provide gas flow during the operation. Based on this arc chamber geometry, the pressure distribution in the arc chamber was calculated with the assumption that the compression motion is adiabatic. According to the result presented in [33], a considerable difference exists between the pressure prediction and measurement, the maximum difference appeared at peak pressure which could potentially be resulted from the over-simplification of the arc chamber. In addition, since all processes related to arcing are not considered, a large discrepancy can also be found between the predicted and measured contact travel, with the measured travel finishing the maximum travel distance using twice the time as the calculated travel. Clearly, resistive forces (among which the reaction force could a significant component) exerted on the moving contact had been grossly underestimated in this case. These differences prove that under high current conditions, the arc has a strong influence on the dynamic characteristics of the driving mechanism which should not be ignored.

In [34] a lumped model of the arc chamber is proposed. The arc chamber is treated as a valve controlled pneumatic cylinder, based on the travel of moving contact, the opening operation is divided into several different stages, so the gas flow can be predicted more accurately compared with the simple cylinder-piston approach. Both opening and closing operation were studied in this case and the lumped driving mechanism model was able to produce reasonable predictions of cylinder speed in both operation scenarios. However, no results regarding the pressure variation in the arc chamber were given. In addition, no indication was given in the work as to how to quantify the interaction between the arc chamber and the driving mechanism.

A complex computational domain which preserves the structural details of the real arc chamber was established in [35]. Equations governing the gas flow were solved numerically. Compared with the approach in [33], numerically solving the governing equations allows a better prediction in arc chamber pressure distribution under no-load condition. However, a clearly defined interface between the driving mechanism model and the arc chamber model which facilitates information exchange between the two independent solvers was not presented. As a result, the simulation can only be considered partially coupled, since the pressure rise in the arc chamber caused by the compression motion was accounted for. However, the true arcing process was not modelled.

In general, the model proposed in [33], [34] and [35] can provide reasonable prediction of the dynamic characteristics of the driving mechanism (hydraulic or spring) to some extent, descriptions of pressure variation in the arc chamber based on these models are largely inaccurate and due to the fact that arcing was not considered, these models are only applicable in no-load simulations.

The current continuity equation was introduced in the arc model proposed in [36] so the electrical field strength can be solved for. With such an approach, if the conductivity of the arcing medium is known, the electric power input from the arc can then be determined. However, the exact method used to determine the conductivity of the arcing medium was not disclosed as well as any result that could potentially be used to verify the electrical field calculation. Furthermore, arc-induced ablation which could also potentially affect the pressure distribution was excluded from the model without justification. According to [37], arc-induced ablation plays a critical role in nozzle clogging and pressure rise in modern gas-blast circuit breakers.

A more comprehensive arc model was used in [28]. Based on this arc model, together with a simple spring driving mechanism model. The pressure in arc chamber was predicted with reasonable agreement with the measured data under load conditions. However, the method used to calculate the reaction force was not described. In addition, no experimental result was utilized to verify the calculation. Since no parametric study was performed, key structural parameters that affect the magnitude of the reaction force cannot be identified.

To truly calculate the reaction force accurately, considering the geometrical details of the arc chamber, the forces exerted by the working gas in the direction of movement on the elementary surface of all moving components must be integrated. That is to say:

$$F_r = \int P \, d\vec{A} \cdot \vec{z} \tag{1.1}$$

where F_r is the total reaction force from the arc chamber, $d\vec{A}$ is the elementary surface vector of moving components contributing to the total reaction force, $\vec{z}$ is a unit vector in the direction of movement and P is the corresponding local pressure.

Based on above discussions, it can be concluded that the main difficulties in developing a truly coupled circuit breaker model are:

a) It is difficult to establish an arc model that includes all pressure-altering phenomena including ohmic heating, nozzle ablation, radiation and turbulence transportation.
b) It is difficult to accurately calculate the reaction force from an arc chamber with complex geometry. Over-simplification of the arc chamber geometry is commonly seen in previous researches. To included geometrical details in the reaction force calculation, the computational domain in which the arc chamber is included must be properly discretized. Meanwhile, an integral method based on Equation (1.1) should be used.
c) It is difficult to develop driving mechanism models with high levels of accuracy, especially for hydraulic driving mechanisms. This is because complex flow conditions are often encountered when modelling the hydraulic driving mechanism, which resulted in the use of semi-empirical approaches to determine the flow characteristics of some of the hydraulic components.

To overcome these difficulties, a comprehensive arc model that encompasses all important processes during arcing as well as a reaction force calculation method based on integration are introduced in the next chapter.

1.5 The Objectives of Research and Structure of the Thesis

This research project is mainly concerned with the coupled simulation (the arcing process in the interrupting chamber and the operation of the driving mechanism) of high voltage circuit breakers. As mentioned earlier, it is important to incorporate the driving mechanism into the current circuit breaker simulation, so the accuracy of the results can be further improved and more useful information can be extracted from simulations. Previously, standalone driving mechanism models (for both hydraulic and spring types) were developed. However, there lacks a successful attempt at coupling the driving mechanism model with the arc model. Therefore, the aim of the research is to:

a) develop a mathematical model of the driving mechanism so that instead of using measured data, the motion characteristics of the moving components can be calculated in real time.
b) develop a method which can calculate the reaction forces from the arcing gas towards the driving mechanism as a function of time during the arcing process.
c) develop an integrated simulation tool which couples the model for mechanical driving mechanisms with the arc model, this includes an interface between the two models which facilitates information exchange during the simulation.
d) based on the simulation tool developed, verify the model and study the interaction between the arc and driving mechanism in detail to provide guidance on the optimization of the mechanical characteristics of the circuit breaker.

The fundamentals of switching arc in SF_6 is explained in Chapter 2, together with the arc model previously developed in the research group. Important process and mechanisms during arcing such as radiation transportation, ohmic heating and nozzle ablation are introduced. In addition, based on the predicted pressure distribution in the arc chamber, a method is developed to calculate the reaction force, which is the quantitative representation of the interaction between the arc and the driving mechanism. Moreover, the development process of independent solver for the hydraulic driving mechanism model is also presented. In order to facilitate coupled simulation, interface which can bridge the driving mechanism and arc model was designed based on the parameters being exchanged between the two solvers (for arc model and driving mechanism model).

Chapter 3 presents the mathematical model of the hydraulic driving mechanisms and the sensitivity studies designed to identify important parameters within the model.

In Chapter 4, the verification of the arc model and the reaction force calculation method are conducted with the aid of experiment results. Based on the coupled simulation results, two calibration tests are also conducted, and the choice of coefficient values explained.

Further study aimed at quantifying the effect of interaction between switching arcs and driving mechanisms is carried out in Chapter 5. Different arcing conditions as well as design parameters of the interrupting chamber (nozzle parameters such as nozzle radius and nozzle throat length) are considered to determine their effect on the magnitude and profile of reaction force. To provide some guidance in terms of circuit breaker design, the relationship between reaction force and the interrupting capability (RRRV) of the breaker is discussed.

Finally, Chapter 6 summarize the research project and provides conclusions drawn from the coupled simulation results. Possible future works are also listed.

Chapter 2 Model of the Arcing Process in Gas-blast Circuit Breakers

2.1 Modelling of the Arcing Process in Gas-blast Circuit Breakers

The design, test and operation of circuit breaker revolve around the concept of switching arc. Traditionally, due to the lack of understanding of the fundamental physical processes associated with switching arc, circuit breaker design relies heavily on experience and tests [38]. Difficulties in performing tests or experiments under high voltage and power have motivated people to invest a considerable amount of effort has been devoted to the better understanding and modelling of switching arcs. Based on the newly gained insights, together with the advancement in computing technology, computer simulations were utilized to analyze the arcing process in gas-blast circuit breakers. The objective of this chapter is to present a comprehensive arc model which is an important part of the coupled circuit breaker simulation tasked with predicting the pressure variation in the arc chamber under different conditions accurately. Furthermore, based on the arc model presented, a method of calculating the reaction force is also introduced in this chapter.

2.1.1 Fundamentals of thermal plasma

The arc is a type of high intensity (in terms of current density) electrical discharge in gaseous medium which is capable of self-sustaining [39]. The pressure encountered in gas-blast circuit breakers is typically above 5 bar. At such a pressure, collisions between particles become frequent enough that through momentum exchange a single mass averaged velocity could be used to describe the macroscopic motion of an entire collection of particles. The intermolecular or atom distance is negligibly small in comparison with the system dimension. A plasma under these conditions can be treated as a continuous electrically conducting fluid [40].

When the contacts of a circuit breaker separate, the gas in the contact gap is ionized following breakdown and the gas temperature rises to a very high value (15,000 K to 35,000 K). This diminishes the insulating capability of the arcing gas and the contact gap becomes conductive. The kinetic energy of particles increases when the temperature rises. The pressure directly affects the collision frequency and mean free path of the particles. The variation of temperature and pressure changes the particle density also. The plasma state determines the gaseous material properties (i.e. density, viscosity, electrical conductivity, thermal conductivity and specific heat). The material properties are essential for switching arc simulation [41].

To make the gaseous material properties predictable, there is a need to choose an adequate approximation of plasma state which can be described theoretically using classical statistical mechanics. Therefore, it is necessary to introduce the concept of complete thermal equilibrium (CTE). For a plasma under CTE, all its constituents and their possible reactions have the same temperature. This indicates that for a plasma under CTE [42]:

a) The velocity distributions for particles of all species follow a Maxwell distribution:

$$\mathrm{d}n_r = 4\pi n_r \left(\frac{m_r}{2\pi kT}\right)^{\frac{3}{2}} exp\left(-\frac{m_r {v_r}^2}{2kT}\right) {v_r}^2 dv_r \tag{2.1}$$

where n_r is the number density of species r, m_r is the mass of particles of the same species, v_r is the magnitude of the velocity vector, T is the temperature which is the same for every species r and k is the Boltzmann constant ($k = 1.38064852 \times 10^{-23}$ J/K)

b) The population density of the excited states of every species r must follow a Boltzmann distribution:

$$n_{r,k} = n_r \frac{g_{r,k}}{Q_r} exp\left(\frac{-E_{r.k}}{kT}\right) \tag{2.2}$$

where n_r is the number density of species r and Q_r is the partition function of the same species, $n_{r,k}$ is the number of particles of species r that are at the k^{th} excited state, $E_{r.k}$ is the energy of the k^{th} state while $g_{r,k}$ is the statistical weight of the same state.

c) The number densities of charged particles can be described by the Saha equation:

$$\frac{n_{r+1}n_e}{n_r}=\frac{2Q_{r+1}}{Q_r}\frac{(2\pi m_e kT)^{\frac{3}{2}}}{h^3}exp\left(\frac{-E_{r+1}}{kT}\right) \tag{2.3}$$

where E_{r+1} is the energy required to generate a $r+1$ order ionized particle from a r order ionized particle, n_{r+1} and n_r represent the number density of the corresponding ionized particles, m_e is the mass of an electron and n_e is the electron number density. $r=0$ represents a neutral particle of the same species.

d) The radiation field within the plasma can be treated as black body radiation and described by Planck's law:

$$B_v^0=\frac{2hv^3}{c^2}\frac{1}{e^{\frac{hv}{kT}}-1} \tag{2.4}$$

where B_v^0 is the spectral radiance of a body, which describes the amount of energy if gives off as radiation of different frequencies v is the frequency, h is the Planck's constant ($h=6.626070040\times 10^{-34}$ m^2kg/s) and c is the speed of light in vacuum.

To maintain CTE, all physical processes occur in the plasma must be reversible. It should be pointed out that CTE is an idealized concept and does not naturally exist on the earth. Local thermal equilibrium (LTE) is derived from the concept of CTE and used for practical plasmas. Although radiation field no longer follows Planck's law, criteria a), b) and c) still hold true for plasma under LTE. Switching arc in gas-blast circuit breakers can generally be classified as high pressure (>1 atm). For high pressure arcs, the assumption of LTE has been widely accepted [43]-[45]. At pressure normally encountered in gas-blast circuit breakers, with a sufficiently high electron number density (it has been shown in [46], for a SF_6 nozzle arc, with an upstream pressure of 0.78 MPa and an exit pressure of 0.1 MPa, the electron number density at current zero is sufficiently high to ensure that collisional processes are dominant), collisional processes between particles becomes dominant while processes associated with photons (photon excitation or ionization) are much less potent compared with collisional processes [47]. When collisional processes dominate, due to limited average distance an electron can travel between two collisions (limited mean free path), average energy gained by electrons from electric field in between two successive collisions is insignificant compare to the random thermal energy. As a result, the same temperature is attained by all species and the arc maintains local thermal equilibrium.

Separate experiments conducted in [46] and [48] have shown that, apart from other gases such as nitrogen, LTE is a reasonable approximation for SF_6 switching arc as well.

2.1.2 A brief review of arc modelling

In modelling of electric arcs, black box models were initially used due to their simplicity [49]. Without delving into the physical processes, the black box model is only concerned with the arc's electrical behaviour in terms of current and voltage. Although being simple, by calculating the conductance or resistance in the contact gap, it is possible to use a black box model to [50]:

a) predict the circuit breaker's influence on the network (as a variable resistor).
b) assess the circuit's influence on the interrupting performance of the breaker (TRV from the system).
c) estimate the interrupting capability of the breaker under different breaking conditions (empirical parameters extracted from measured arc voltage and current during a "pre-zero" period can be used to describe the state of a circuit breaker after each test, thus roughly determining the margin of interruption capability [51]).

A black box model for arc modelling was first proposed by Cassie in the late 1930s [52]. It is found to be an acceptable approximation of high current arcs. However, it fails to predict the arc behaviour around current zero since the model does not consider the rapid temperature variation near current zero. Later Mayr extended Cassie's model in the 1940s to cover the current zero region by allowing variation in gas temperature [53]. Nevertheless, due to the lack of a comprehensive description of the arcing process and heavy reliance on test data, in the field of switching arc research, the black box models were shortly surpassed by other more advanced models.

By the mid-1960s, advancement in plasma theory had led to the establishment of fundamental arc conservation equations [54]. However, the practical aspects of arc modelling such as numerical methods and computing power had failed to keep up with the theory and were proven to be inadequate to solve the arc conservation equations in full differential form.

The introduction of boundary layer assumption had [55] greatly simplified the modelling of gas-blast arcs. The assumption states that the flow in gas-blast arcs is predominantly axial. The characteristic length of the arc in the radial direction (arc thermal radius) is considerably smaller than that in the axial direction (length of the arc column). Consequently, the radial gradient of physical quantities is much greater than their axial counterpart resulting in the neglection of axial energy and momentum diffusion. Invoking this assumption allows a gas-blast arc to be divided into two distinct regions in the current zero period, namely the external flow and the arc thermal influence region.

Based on this assumption, much progress in arc research has been made. The arc conservation equations while in full differential form, can be radially integrated, leaving only the axial derivative terms in the equations [56]. The introduction of the integral methods signified that arc modelling had transformed from guess to rigorous analysis. While different integral methods had been proposed, the main distinguishing factor is the assumptions made to close a set of integral equations [57]. Lowke and Ludwig had [58] made the assumption that the Mach number of the arc flow and the surrounding gas flow is the same and is to be calculated according to the nozzle geometry. In addition, they had adopted a top-hat shaped radial temperature profile which is more realistic (in the sense that a top-shaped radial temperature profile is the natural result under the influence of thermal conduction and turbulence at the edge of the arc) than the profile proposed in [56]. This allowed them to determine the thermal boundary of the arc when the current is relatively high (>2 kA). However, their results were not satisfactory under low current conditions, since the assumed radial temperature profile is only acceptable under high current.

In an effort to generalize the integral approach for boundary layer arc analysis, a model which includes external flow conservation was proposed in [59] by Cowley. An energy conservation equation for the arc core was later added to the model presented in [59] by Chan [60]. It has been shown that for some arcing conditions current zero arc behaviour can also be examined [61].

Apart from the theoretical investigations, measurements and experiments were also conducted. The BBC research center in Switzerland [62]-[63] had successfully measured temperature (the maximum axial temperature is 20000 K at 20 μs before current zero and 15000 K at current zero) and pressure (the maximum axial pressure is 2.2 MPa) as well as the electric field (500 V/cm at 2 μs before current zero) in a gas-blast circuit breaker with a current which has a peak magnitude of 2000 A. Moreover, an arc model with two distinct temperature regions (a high temperature arc region and a surrounding external cold flow region) was proposed in [63]. The turbulent nature of gas-blast arc is demonstrated in the study by considering turbulence momentum and heat transfer, the results showed good agreement between prediction and measurement regarding the characteristics of a nitrogen arc with a current of 2 kA.

There is no doubt that the integral method achieved a certain level of success in predicting the arc behaviour and compared with differential methods, the computational cost is relatively low. However, for the current zero period integral method has only very limited success, because the shape factors that relate the arc thermal area to the external cool region were difficult to determine. In essence, with the aid of some assumptions, the integral method replaces the radial dependency of variables with integral quantities. However, when the current is small, both the axial and radial variations of physical quantities become important. As a result, the shapes factors can no longer be relied upon to correctly reflect the radial temperature profile.

It was not until the 80s, when computers become powerful enough that solving the arc conservation equations in full differential form is possible. Nevertheless, the arc conservation equations are non-linear in nature, making the solution procedure extremely complicated. The pioneering work in applying differential method to arc analysis was done by Ragaller et al [64] at BBC in 1982. The dielectric recovery process in an axially blown SF_6 arc was investigated. Based on the Prantl mixing length model, turbulence was first integrated into the conservation equations and results were then compared with measurement data [65] in order to prove the significance of turbulence as a cooling mechanism after current zero. However, a turbulence grid was used in [65] to artificially induce turbulence in the stagnation region. Although the results show good agreement, this approach was not entirely convincing as the turbulence in the gas-blast arc was largely self-generated and presumably with less intensity. The importance of turbulence was shown in the comparison between current zero behaviour of gas-blast arcs in different gases [43][66][67]. It has been discovered that for nitrogen arcs laminar flow model can give reasonable perdition of thermal interrupting capability while the same success cannot be replicated with SF_6 arcs.

The lack of a way to accurately predict radiation transport is another factor that had hindered the development of differential methods. In the 70s, experimental studies [68][69] had laid the foundation for theoretically calculating the transport of energy by radiation. It has been proven that [74] with the use of net radiation emission coefficient, it is possible to predict the temperature profile of a wall-stabilized arc with a satisfactory degree of accuracy. The concept of reabsorption layer was later introduced in [75] to allow the method to be used in arcs in axial gas flows.

In 1999, considering all important physical processes, the arc behaviour in an auto-expansion circuit breaker was successfully simulated by Yan [17]. Then, the work is repeated by Zhang [76], but using newly calculated properties of SF_6 and PTFE vapour, which improved the prediction in 2002. Recently, the behaviour of SF_6 arcs under shock conditions has been investigated by Fang et al [77][78].

An approximate radiation model was proposed in [71] and a proper account of radiation transport was achieved. The radiation model was based on the measurement of Ernst et al [68] for wall stabilized N_2 arcs and on the detailed radiation transport calculation of Shayler and Fang [79] for N_2 and of Liebermann and Lowke [80] for SF_6.

2.1.3 Governing equations of gas-blast arcs

The interrupting chamber of gas-blast circuit breaker is often designed to be rotationally symmetric. As a result, a 2-D axis-symmetric computation domain can be used as a good approximation of the real chamber, this simplification reduces the complexity of the simulation and saves computation time significantly [81]. With the assumption that an arc is under LTE, its behaviour can be mathematically described in a 2D cylindrical coordinate system by the time-averaged Naiver-Stokes equations with important factors such as radiation transportation, ohmic heating, nozzle ablation and turbulence enhanced mass, momentum and energy transport taken into consideration:

$$\frac{\partial(\rho\emptyset)}{\partial t} + \nabla\cdot\left(\rho\emptyset\vec{V}\right) - \nabla\cdot\left(\Gamma_{\emptyset}\nabla\emptyset\right) = S_{\emptyset} \qquad (2.5)$$

where $\emptyset$ is the variable to be solved and, ρ is the density of arcing medium, $\vec{V}$ the velocity can be decomposed into w and v representing respectively axial and radial velocity components of a gas or gas mixture. The source term $S_{\emptyset}$ and the diffusion coefficient $\Gamma_{\emptyset}$ are listed in Table 2.1.

Table 2.1 Source terms and diffusion coefficients for governing equations.

Equation	$\emptyset$	$\Gamma_{\emptyset}$	$S_{\emptyset}$
Mass	1	0	0
momentum	$\vec{V}$	$\mu_l + \mu_t$	$-\frac{\partial P}{\partial z} + J_r B_\theta + viscous\ terms$
R-momentum	v	$\mu_l + \mu_t$	$-\frac{\partial P}{\partial r} - J_z B_\theta + viscous\ terms$
Enthalpy	h	$\frac{(k_l + k_t)}{C_p}$	$\sigma E^2 - q + \frac{dP}{dt}$ $+ viscous\ dissipation$
PTFE mass concentration	C_m	$\rho(D_l + D_t)$	0

Current continuity	φ	σ	0

where μ is dynamic viscosity, P the pressure, J the current density and B the magnetic flux density. θ indicates the azimuthal direction of a cylindrical polar coordinates system. k is thermal conductivity, $C_p$the specific heat at constant pressure, σ the electrical conductivity, E the the electric field, q the the net radiation loss per unit volume and time. C_m the PTFE mass concentration, D the diffusion coefficient, the subscript l denotes the laminar part of the diffusion coefficient and t the turbulent part.

The conservation equations shown above is only concerned with the main arc column. In the region near electrodes (anode and cathode), LTE no longer holds. Fortunately, these regions are normally very thin in terms of length and contribute little to the characteristics of the arc.

2.1.3.1 Radiation transportation

In electric arcs, when temperature and pressure are sufficiently high, there always exist regions where radiation is the dominant energy transport mechanism and other regions where heating from radiation is far more intense than ohmic heating [82]. Contrary to low pressure and current cases, according to [45], when pressure and current are at 10 atm and 1.9 kA respectively, radiation transport has been found to be dominant in the arc core region. To fully examine the energy balance and ultimately predict the physical behaviour of the arc, energy transportation by radiation must be accounted for.

Naturally, for arcs under LTE, the Planck's law can no longer be used to describe radiation field. Therefore, a separate radiation model is needed in order to incorporate the source term in the energy conservation equation. In this research project, a semi-empirical radiation model introduced in [75] is used after considering both the accuracy of the model and the computational cost. This model is a 1-D model based on the concept of net emission coefficient (NEC) [80] and assumes a monotonic radial temperature profile with the maximum temperature on the axis as shown in Figure 2.1.

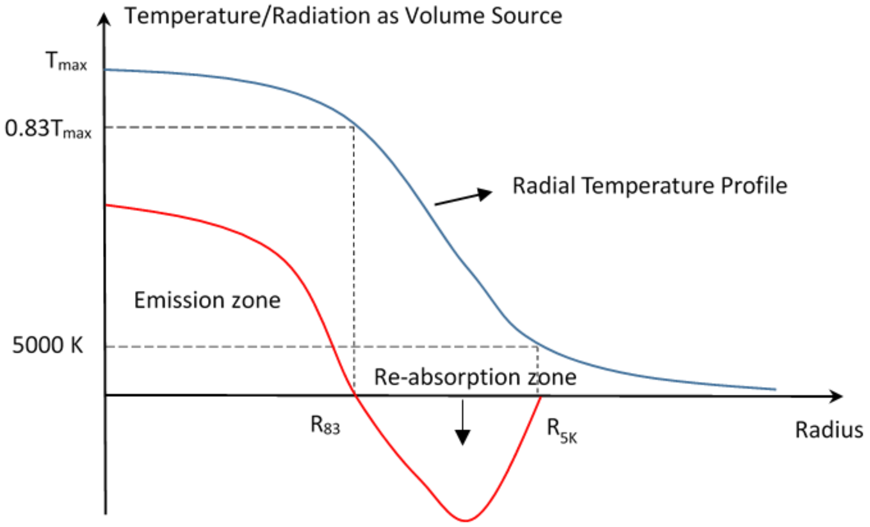

Figure 2.1 Monotonic radial temperature profile in [75] and the emission (0 ~ R83) and re-absorption (R83 ~ R5k) zones.

Based on this temperature profile, the arc core is defined by the axis and the radial position of 83% of the axial temperature (0.83 T_{max} in Figure 2.1). The arc core also marks the radiation emission zone, the net radiation loss per unit volume and time (q in Equation (2.5)) inside the emission zone is related to the NEC (denoted by ε) which is a function of pressure, temperature and arc radius:

$$q_c = 4\pi\varepsilon(P, T, R_{arc}) \tag{2.6}$$

where R_{arc}, the radiation arc radius and is defined by:

$$R_{arc} = \frac{R_c + R_e}{2} \tag{2.7}$$

R_c and R_e are the radii of arc core boundary and arc electrical boundary respectively. For different types of circuit breakers, R_e is chosen differently. For puffer circuit breakers, the 5000 K isotherm is used while for auto-expansion circuit breakers the 4000 K isotherm is used instead. The NEC data given in [80] is used and calibrated (multiplied by a factor of 1.5) by arc voltage comparison under high current conditions. The total amount of radiation from the arc core is then:

$$Q = \int_{axis}^{R_c} q_c 2\pi r dr \tag{2.8}$$

The radiation from arc core will be partly absorbed in what is known as the radiation reabsorption zone which lies between the arc core boundary and arc electrical boundary. Distribution of radiation absorbed per unit volume and time in this region is:

$$\frac{q_a(r)}{q_0} = 1.1 - \left(\frac{R_c+R_e-2r}{R_e-R_c}\right)^2 \tag{2.9}$$

where q_0 is defined as:

$$q_0 = \frac{PCT\times Q}{\int_{R_c}^{R_e}\left[1.1-\left(\frac{R_c+R_e-2r}{R_e-R_c}\right)^2\right]2\pi r dr} \tag{2.10}$$

where PCT is the percentage of the radiation energy flux absorbed in the absorption zone (for puffer circuit breaker PCT=80% and for auto-expansion circuit breaker PCT=50%, the disparity is due to in puffer circuit breakers the surrounding cold flow often has a higher axial velocity compared to the auto-expansion arc). Note that the term $\int_{R_c}^{R_e}\left[1.1-\left(\frac{R_c+R_e-2r}{R_c-R_e}\right)^2\right]2\pi r dr$ indicates the equivalent area in which the amount of radiation, $PCT\times Q$, is absorbed. In addition, position of arc electrical boundary is further away from the axis than arc core boundary, as a result, the reabsorption q_a is a negative volume metric energy source. Therefore, while considering the whole arc region, q is defined as positive, so the radiation loss q_c can be reflected as:

$$q = \begin{cases} q_c & r \le R_c \\ -q_a & R_c \le r \le R_e \end{cases} \tag{2.11}$$

2.1.3.2 Nozzle ablation

After being partly absorbed in the radiation reabsorption zone, the rest of the radiation flux from arc core eventually reaches the nozzle wall (commonly made by polytetrafluoroethylene (PTFE)). The radiation energy evaporates nozzle material (known as nozzle ablation) which is subsequently injected into the surrounding gas flow. The amount of PTFE vapour released due to nozzle ablation depends on the radiation flux reaching the nozzle surface, as well as the ablation energy ($1.19\times 10^7 J/Kg$): energy required to decompose the PTFE chain structure and raising the temperature of PTFE vapor from 300 k to 3400 k [37]:

$$\overline{m} = \frac{Q_{nozzle}}{h_v} \tag{2.12}$$

where Q_{nozzle} is the radiation flux per unit length reaching the nozzle surface, $\overline{m}$ is the rate of ablation per unit length as a mass source injected into the flow domain, and h_v is the ablation energy.

Depending on the nozzle geometry, contact position and dynamic behavior of the arc, gas surrounding the arc could be SF6 or PTFE vapor or a mixture of both. The mixing of SF6 and PTFE vapour does not have a significant impact on NEC data since both SF6 and PTFE vapour under high temperature have high fluoric content. To demonstrate this point, the NEC data of SF6 and PTFE vapour mixture at different concentration are presented in Figure 2.2.

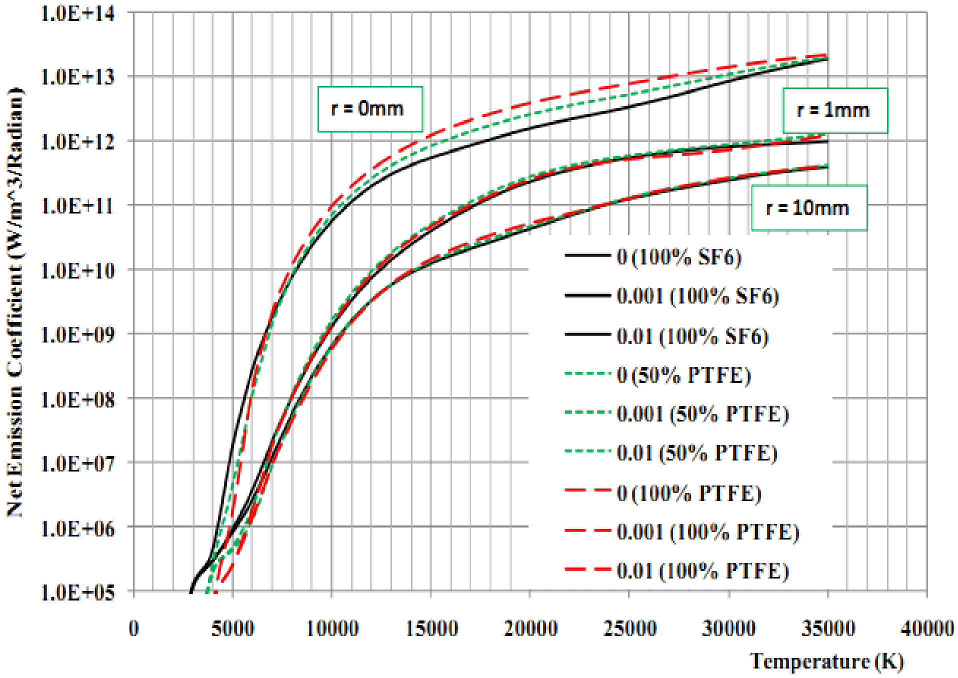

Figure 2.2 NECs of SF6 and PTFE vapour mixture at different concentrations and pressures.

Although the same NEC data can be used, the mixing of SF_6 and PTFE vapour does raise the need to solve the PTFE mass concentration equation since the density ρ as a function of temperature and pressure, as well as transport properties (laminar viscosity μ_l, the ratio of laminar thermal conductivity to the specific heat at constant pressure k/C_p, and electric conductivity σ) of SF_6 with different PTFE concentrations need to be calculated in advance. [76] has provided relevant data for SF_6 and PTFE mixture, interpolation is used to find the value of variables at a particular pressure, temperature (enthalpy) and vapor concentration. Mass concentration of PTFE vapor in a mixture with SF_6 is defined by:

$$C_m = \frac{n_{PTFE} M_{PTFE}}{n_{SF_6} M_{SF_6} + n_{PTFE} M_{PTFE}} \tag{2.13}$$

where n_{PTFE} and M_{PTFE} are respectively the molar number and molar mass of the vapor, and n_{SF_6} and M_{SF_6} are those of SF_6.

When vapour is present in the arcing flow, it is not only carried by the gas flow, but also diffuses from a high concentration region to a low concentration region. The diffusion of vapour in a mixture is a complex phenomenon when more than two species are present in the mixture. The diffusion coefficient is expressed as $\rho(D_l + D_t)$ (see Table 2.1) where D_l is the laminar diffusivity and D_t the turbulent diffusivity. With the assumptions of LTE and Local Chemical Equilibrium (LCE), a combined diffusion coefficient [83] can be used to describe the laminar diffusion of species belonging to one gas in a mixture of two gases. D_l and D_t are respectively related to the local laminar viscosity and turbulent viscosity by the laminar and turbulent Schmidt number:

$$S_{cl} = \frac{\mu_l}{\rho D_l} \;\&\; S_{ct} = \frac{\mu_t}{\rho D_t} \tag{2.14}$$

The magnitude of S_{cl} and S_{ct} are around unity and a value of 1.0 can be used for S_{ct} [84].

2.1.3.3 Ohmic heating and Lorentz force

Ohmic heating (also resistive heating) is the consequence of the interaction of a charged particle in an electric circuit accelerated by an electric field but must give up some of their kinetic energy every time they collide with ions of the conductor. The increase in kinetic or vibrational energy of the ions manifests itself as heat and an increase in the temperature of the conductor [85]. Ohmic heating is included in the energy conservation equation as a source term σE^2. To properly account for ohmic heating, both electrical conductivity of the arcing medium (σ) and the electric field (E) need to be calculated. As a function of pressure, temperature and PTFE concentration, the electrical conductivity can be obtained via interpolation based on pre-defined data sheet [76]. Electrical potential (φ) can be obtained by solving the electrical charge conservation equation:

$$\nabla \cdot (-\sigma \nabla \varphi) = 0 \tag{2.15}$$

Knowing that electric field is the negative gradient of the potential:

$$E = -\nabla \varphi \tag{2.16}$$

The electric field is then linked related to current density via Ohm's law:

$$J = \sigma E \tag{2.17}$$

or

$$\begin{cases} J_r = \sigma E_r = -\sigma \dfrac{\partial \varphi}{\partial r} \\ J_z = \sigma E_z = -\sigma \dfrac{\partial \varphi}{\partial z} \end{cases} \tag{2.18}$$

When current is relatively low (< 15000 A), the radial component of current density is negligible when compared to its axial counterpart ($J_r \ll J_z$). In this case, a simplified version of the Ohm's law can be used and the electric field is calculated by:

$$E_z = \frac{I}{\int_{axis}^{R_c} \sigma 2\pi r dr} \tag{2.19}$$

Lorentz force is generated by the interaction between the current passing through the arc and the magnetic field generated by the arcing current itself. Note in Equation (2.5), only the azimuthal component of the magnetic field (B_θ) is considered, this is concluded from the fact that the arc column is rationally symmetric. Assuming a homogeneous distribution of permeability, the azimuthal component of the magnetic field is:

$$B_\theta = \frac{\mu_0 \int_0^r J_z 2\pi r dr}{2\pi r} \tag{2.20}$$

where μ_0 is the permeability of the arcing medium and J_z is the axial current density. The Lorentz force in radial and axial directions, as volumetric forces in Table 2.1, can then be expressed as:

$$\begin{cases} F_r = -J_z B_\theta \\ F_z = J_r B_\theta \end{cases} \tag{2.21}$$

2.1.3.4 Arc instability (turbulence)

Although applicable to nitrogen arcs [63], the laminar flow model was not ideal for SF_6 arcs. With laminar flow theory applied to SF_6 arcs, a large discrepancy between the calculated and measured radial temperature profile was found [66]. This proves that SF_6 is turbulent in nature and transport mechanisms such as turbulence enhanced momentum and energy transport should be incorporated into the arc model [67].

The Prandtl mixing length model (PML) is arguably the oldest and most simple turbulence model, developed by Prandtl in 1925 [55]. The past application of the Prandtl mixing length turbulence model to arcs in supersonic flow has had proven successful [75]. The K-epsilon model is another turbulence model commonly used in simulations of turbulent flows [69]-[71]. It has been shown [72] that because of the poor understanding of arc turbulence, using the simple Prandtl mixing length model has advantages over the two-equation k-epsilon model. Therefore, in the present research, the Prandtl mixing length model is used instead of the K-epsilon model family.

The concept of eddy viscosity (μ_t in Equation (2.5)) is introduced to account for turbulence enhanced momentum and energy transfer. In the Prandtl mixing length model, eddy viscosity which signifies the turbulence enhanced momentum transfer is related to the flow field by:

$$\mu_t = \rho(cR)^2\left(\left|\frac{\partial v}{\partial z}\right| + \left|\frac{\partial w}{\partial r}\right|\right) \tag{2.22}$$

where ρ is the density, c the turbulence model parameter and R a characteristic dimension of the arc column which is defined as the radial distance from the axis to the point of 5000K for the high current phase. The definition of R is influenced by the magnitude of arcing current. When current is relatively high (above 15000 A), R is equated with the 5000 K isotherm. For low current conditions (below 15000 A), the use of 5000 K isotherm will lead to an underestimate of the size of the high-speed jet where turbulence mixing is strong. So, in the current zero period and the subsequent post arc current calculation, R is defined as the radius of 3000K isotherm. In practice, the turbulence parameter c is set to a constant value at high current. This is because while current is relatively high, the arc column usually takes up the entire diameter of the nozzle throat leaving only a very thin annular path for the ambient cold flow to pass through. Consequently, the turbulent effect is less renowned under high current conditions. When the current is low however, the turbulence parameter is set to change linearly from its high current value to a desired pre-set value for the low current phase [75]. The value of c is dependent on the circuit breaker geometry and is to be calibrated by measured arc voltage.

The turbulent thermal conductivity represents the turbulence enhanced energy transfer, it is related to eddy viscosity through the Prandtl number:

$$P_{rt} = \frac{\rho v_t}{k_t / C_p} \tag{2.23}$$

where C_p is the specific heat capacity at constant pressure, k_t is the turbulent thermal conductivity and P_{rt} is the Prandtl number. The Prandtl number is dimensionless and it has been found for the purpose of arc simulation, $P_{rt} = 1$ is sufficient since there are adjustable parameters in the turbulence model that are determined based on experiment for switching arc applications.

2.2 The Interaction between Arc and Driving Mechanism

The arcing chamber and driving mechanism are both important sub-systems of a modern gas-blast type circuit breaker. The operation of these two sub-systems is closely coupled through interactions between the arc and moving components in the arcing chamber. This interaction normally takes the form of a reacting force on the surfaces of certain moving objects applied by the highly pressurized gas. It is known that the pressure field in the arcing chamber is drastically altered with the presence of a high fault current arc. The interaction between the moving components and the high-pressure gas results in the altered speed of the moving components. This is more significant for high current amplitude, long arc duration cases.

2.2.1 Computational domain and structural grids in PHOENICS

Most of the CFD simulations require a grid system which can be used to discretize the computational domain, so a continuous distribution of a physical quantity can be approximated by values at these discrete locations.

PHOENICS only supports structural grid system and there are three types available: Cartesian coordinate system, cylindrical polar coordinate system and body-fitted coordinate system (BFC). The structured grid system takes its name from the fact that the grid is laid out in a regular repeating pattern. These types of grids utilize quadrilateral elements in 2D and hexahedral elements in 3D.

In arc simulation, geometry of the circuit breaker arcing chamber is usually two-dimensional, axis-symmetrical and with curved shapes at the contact and nozzle area. BFC grid system is used in circuit breaker simulations to incorporate curved solid objects in the computational domain. Figure 2.3 is a cross-sectional view of the BFC grid system used to represent the curved shape of the nozzle wall. The cells in the r-z plane (for a 2-D simulation, the x dimension is neglected) are quadrilateral changing from a near parallel shape near the nozzle wall to rectangular shape in the arc region.

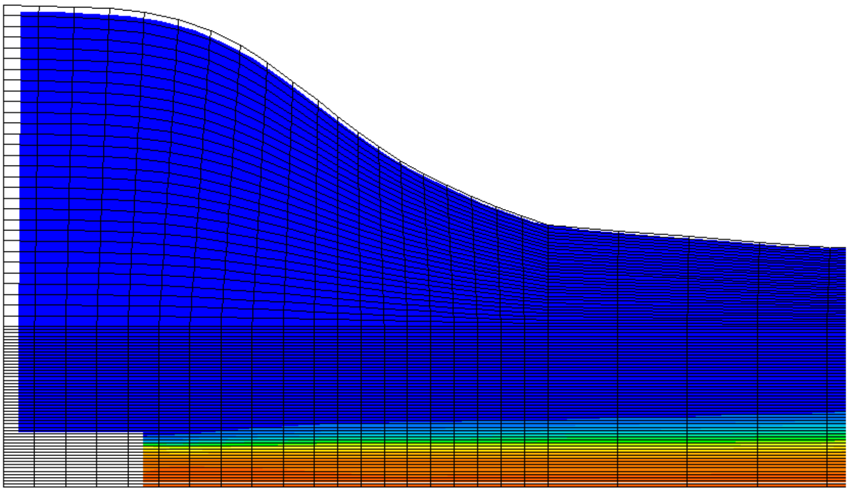

Figure 2.3 A cross-sectional view of the BFC grid system used to represent the curved shape of the nozzle wall. The cells in the r-z plane are quadrilateral changing from a near parallel shape near the nozzle wall to rectangular shape in the arc region.

As shown in Figure 2.4, a cell is addressed by its axial direction cell number (accounted from the axis up, represented by the variable JY) and its radial position cell number (counted from the lower-left corner of the domain, represented by the variable KZ). The first cell is labelled as Cell (1,1) which indicates this cell is the first cell in the radial direction (vertical direction) and also the first cell in the axial direction (horizontal direction). In this way Cell (2, 3) will indicate the second cell in the radial direction and the third cell in the axial direction, and so on. In ground() or other user-defined subroutines, if there is a need to temporarily store the values of a variable in the whole domain, it is possible to use a two-dimensional array with the first dimension for radial cells and the second dimension for axial cells. It is also worth mentioning that two other variables: NZ and NY represent the rightmost radial position cell number and the upmost axial position cell number respectively.

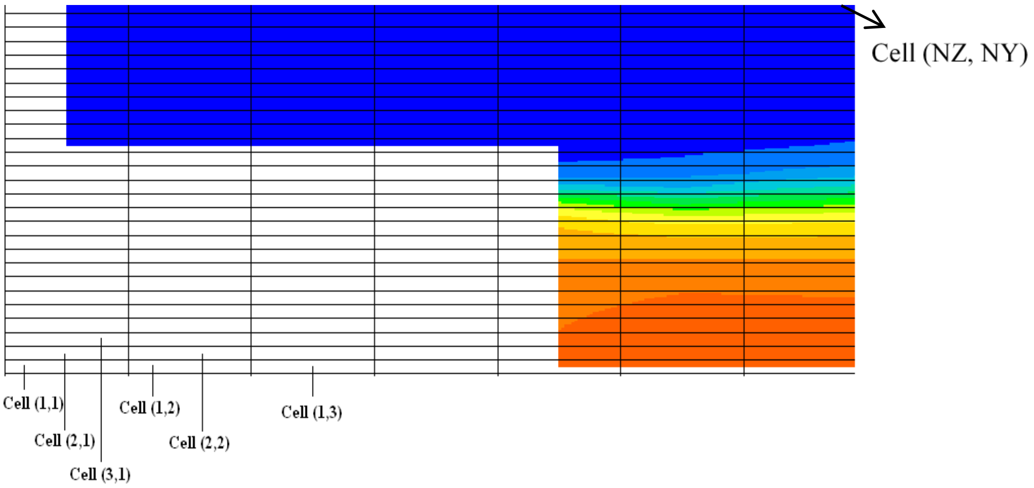

Figure 2.4 Diagram showing the address of cells in the domain. The x-direction is not shown.

In a 2-D coordinate system, as shown in Figure 2.5, a cell has four neighbouring cells, the neighbour cell located on the positive z-direction is called the cell on the High side (H cell), and the one located on the negative z-direction side is called the Low side neighbour (L cell). Similarly, the two neighbours in the y-direction are called North and South neighbours (x-direction not considered). When the value of a quantity at the cell centre is needed, the subscript P is used to represent the cell centre value and H, L, N, S are used to address the values at the cell centre of the neighbours. Sometimes values on the cell faces also needed. In this case the lower-case h, l, n, s are used in the subscripts to represent the values on the cell face.

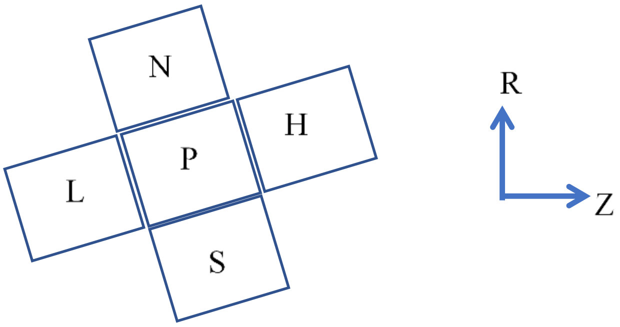

Figure 2.5 Diagram showing the naming of four neighbour cells of a particular cell. Diagram showing the naming of four neighbour cells of a particular cell.

Since the reaction force is applied on the moving components (in reality) by pressurized gas, it always points towards the solid object from the gaseous region. A PHOENICS stored variable PRPS is used to identify if a cell is solid or gas. A cell with a PRPS value of -1 is a gas cell; other PRPS values indicate the cell is solid.

2.2.2 Method of calculating the reaction force

In order to calculate the reaction force accurately, it is essential to develop a method that can identify each individual cell and its faces on which the force should be calculated.

For a typical simulation case, the number of gas cells in the domain far exceeds the number of solid cells. To simplify the calculation process and save computing time, solid objects are chosen as references in the reaction force subroutine. Any gas cell should not be taken into consideration when calculating the reaction force. To exclude all gas cells from reaction force calculation, a scan through the entire domain is necessary. The PRPS value of each individual cell is examined during the scan and any cell with a PRPS value of -1 is not considered in the following calculation. Moreover, due to the presence of some moving components, it is necessary to carry out the scan at each time step. This is because in PHOENICS, an object's movement takes place in a discrete manner, namely, a slab of solid cells may be completely evacuated at a particular instant depending on the travel of the solid object. The PRPS value of a cell can be changed as the simulation proceeds.

Apart from all the gas cells, some of the solid components should also not be included in the reaction force calculation. The operation of circuit breakers involves several moving objects such as the upstream contact and nozzle. Figure 2.6 shows a typical geometry of a high voltage circuit breaker arcing chamber.

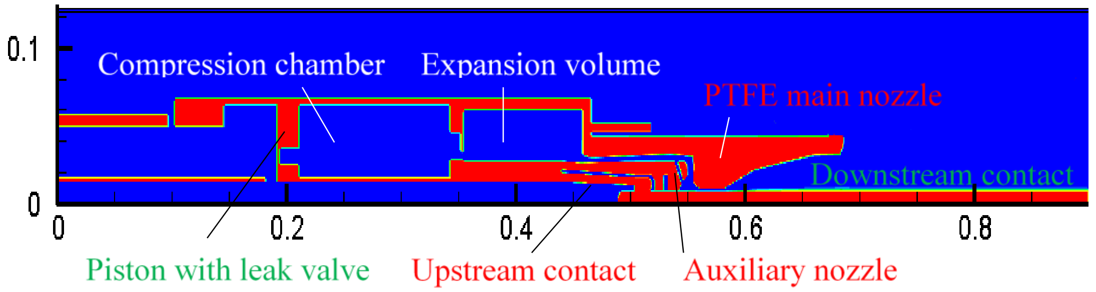

Figure 2.6 A diagram showing the geometry of an auto expansion circuit breaker arcing chamber. The real moving objects are highlighted by red characters while objects move in simulation are highlighted by green.

In reality, the driving mechanism is connected to these moving components; providing them with necessary motion to achieve the interruption of current. However, it is very difficult to deal with curved moving objects in a structural grid system. Consequently, in the Liverpool arc model, the piston in the compression chamber and the downstream contact are modelled as moving objects due to their simple geometry while the real moving components such as upstream contact and nozzle are kept stationary. This is valid because the relative motion between the real moving and stationary components remains unchanged in the simulation.

The reacting force for the driving mechanism is determined by the net force acted by the working gas on all components that move in reality. Therefore, in circuit breaker simulation, the reaction force is obtained by integrating on the surface of all stationary components the elementary forces exerted by the working gas in the direction of movement. For this reason, all components that move in simulation should not be included in the calculation of the reaction force. This can be done by identifying the four boundaries of the moving objects and updates their location as the simulation proceeds. In PHOENICS, a specially defined variable 'move' contains such information. By comparing the position of every cell against these boundary locations, any cell belongs to a moving solid object (in simulation) should not be included in the following process.

In addition, valves are often used in circuit breaker arcing chambers to control gas flow and regulate internal pressure. Typically, there are two types of valves being modelled in a circuit breaker simulation. The first type of valve is attached to a moving piston, and the second type remains stationary. The effect of valve operation is modelled by the opening and filling of the valve holes. A valve attached to a moving piston at its fully opened position is shown in Figure 2.7.

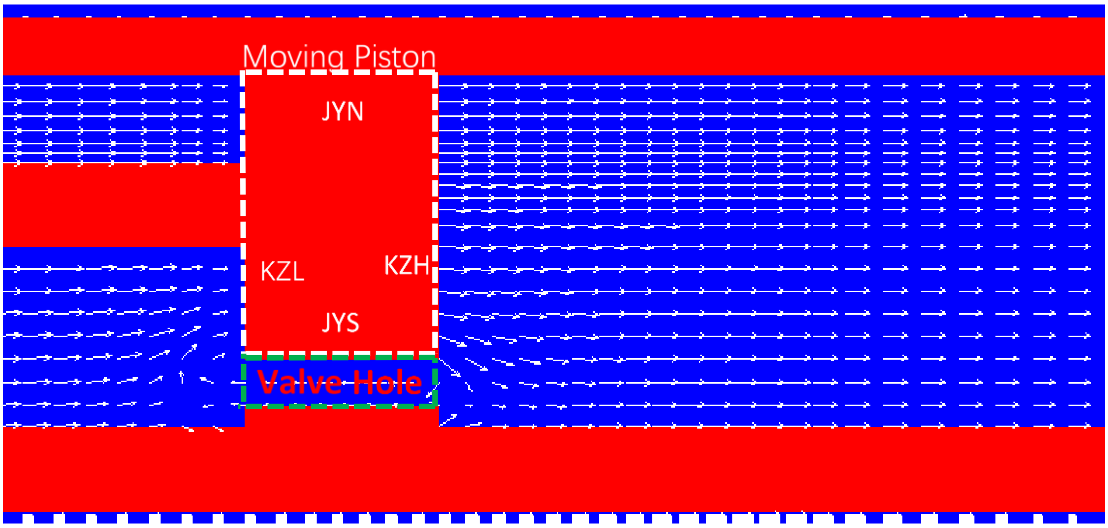

Figure 2.7 A valve attached to a moving piston. The valve is fully opened with gas flowing through the piston. A stationary vale opens in the same manner, with a valve hole turning a block solid into gas cells which allows the flow of gas.

Clearly, no matter what state the valve is in, during the simulation, it never extends beyond the domain of the moving piston (defined in Figure 2.7 by the white broken box). Since the piston is stationary in reality, the whole area surrounded by the white broken box in Figure 2.7 should be excluded from reaction force calculation despite the existence of a valve. In this way, the moving valve is effectively excluded from the calculation together with the piston.

For the stationary type valve, when it opens, a valve hole appears on the valve plate (refer to Figure 2.7). As the previously solid cells are now gaseous; the scan within each time step should recognize this change and these cells (defined in Figure 2.7 by the green broken box) will also not be considered in reaction force calculation.

After eliminating all the gas cells, it is now time to consider which of the faces of the remaining solid cells the reaction force should be calculated. This can be achieved by examining the PRPS values of four neighbouring cells of a particular solid cell. If a neighbouring cell is a gas cell, then the corresponding face should be included in reaction force calculation. For example, for cell P depicted in Figure 2.8, its north and high neighbour cells are gas cells while its south and low neighbours are solid, then the north and high face of cell P should be marked for reaction force calculation.

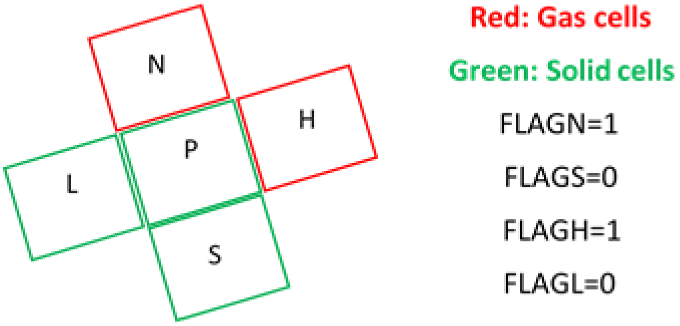

Figure 2.8 Diagram showing the definition of flag variables. A value of 0 is assigned if the corresponding neighbour is a solid cell while a value of 1 is assigned when the neighbour cell is gas.

Four flag variables (in correspondence with four faces of a cell, i.e. FLAGN, FLAGS, FLAGH, FLAGL) are defined in the subroutine to extinguish between marked and unmarked faces of a particular cell. If a cell is gaseous or in the region of a moving object (in simulation) and needed to be excluded from the calculation, one can simply set all four flag values of this cell to 0. Contrarily, with a flag value of 1, the corresponding face of a cell is taken into consideration when calculating the force.

To sum up, for a specific face of a cell to be considered in the calculation, it must meet the requirements listed below:

- The cell must be a solid cell.
- The cell must not be in the region of any moving components (in simulation).
- The corresponding neighbour cell must be a gas cell.

After eliminating all ineligible cells, it is necessary to establish a procedure to calculate the elementary reaction force on each cell face. According to four flag values defined earlier, four independent cases exist when calculating the elementary reaction force (note these cases can exist simultaneously), namely, the gas cell is on north, south, high or low face of the solid cell. If a flag value is detected to be 0, then the corresponding calculation of the elementary force is simply skipped by the program.

Here, the case where the gas cell is on high face of the solid (see Figure 2.9) is chosen as an example to demonstrate the derivation of equations used in calculating the elementary force.

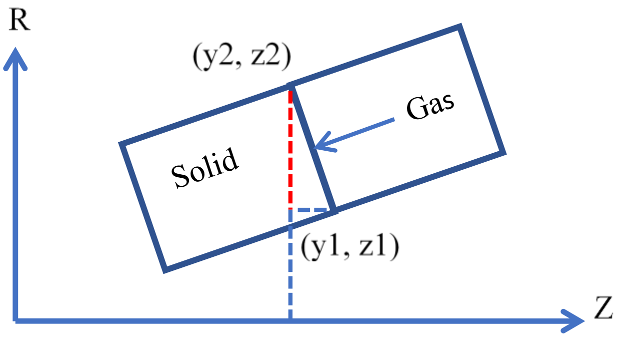

Figure 2.9 Diagram showing the gas cell is on the high face of the solid cell and the position of (y1, z1) and (y2, z2).

The vector pointing from (y1, z1) to (y2, z2) can be expressed as:

$$\overrightarrow{V_{12}} = (y_2 - y_1)\hat{y} + (z_2 - z_1)\hat{z} \tag{2.24}$$

According to vector theory, the vector that is perpendicular to $\overrightarrow{V_{12}}$ is:

$$\overrightarrow{V_h} = (y_2 - y_1)\hat{z} + (z_2 - z_1)\hat{y} \tag{2.25}$$

Therefore, the unit vector that is perpendicular to the solid-gas interface is:

$$\overrightarrow{V_{hu}} = \frac{(y_2-y_1)\hat{z}+(z_2-z_1)\hat{y}}{\sqrt{(y_2-y_1)^2+(z_2-z_1)^2}} \tag{2.26}$$

Since it has been already established that the reaction force is only acting in the direction that is parallel to the z-axis, only the z-direction component is needed for the calculation:

$$\overrightarrow{V_{huz}} = \frac{(y_2-y_1)\hat{z}}{\sqrt{(y_2-y_1)^2+(z_2-z_1)^2}} \tag{2.27}$$

Now consider the area of the solid-gas interface, in reality, it is the area of a circular ring in a cylindrical coordinate system. In a 2-D domain, using the coordinates of (y1, z1) and (y2, z2), it can be expressed as:

$$A_h = \pi\sqrt{(y_2-y_1)^2+(z_2-z_1)^2}(y_1+y_2) \tag{2.28}$$

Finally, the elementary reaction force on the high face equals:

$$F_h = -A_h \cdot \overrightarrow{V_{huz}} \cdot P_{gas} \tag{2.29}$$

Where P_{gas} is the pressure inside the gas cell, in this case the cell one the high face. The negative sign on the right hand side of the equation indicates that the force on the high face of any cell is always in the negative direction. Therefore:

$$F_h = -P_h \cdot \pi({y_2}^2 - {y_1}^2) \tag{2.30}$$

Similarly, when the gas cell is on low face of the solid (Figure 2.10), the elementary force can be calculated as:

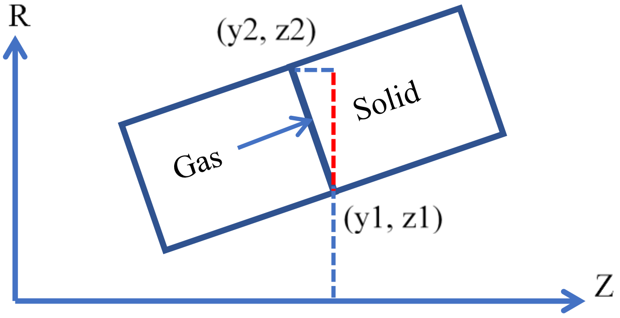

Figure 2.10 Diagram showing the gas cell is on the low face of the solid cell and the position of (y1, z1) and (y2, z2).

$$F_l = A_l \cdot \overrightarrow{V_{huz}} \cdot P_{gas} = P_l \cdot \pi({y_2}^2 - {y_1}^2) \tag{2.31}$$

Since the positive direction for reaction force has been defined as the same as positive z-direction, by default, the elementary force on the south face is also negative. So the reaction force is:

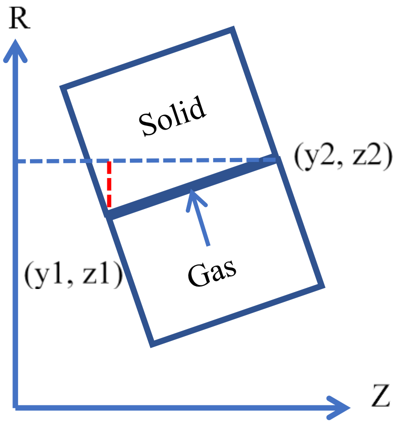

Figure 2.11 Diagram showing the gas cell is on the south face of the solid cell and the position of (y1, z1) and (y2, z2).

$$F_s = -A_s \cdot \overrightarrow{V_{huz}} \cdot P_{gas} = -P_s \cdot \pi({y_2}^2 - {y_1}^2) \tag{2.32}$$

Finally, if the gas cell is on the north face of the solid gas, then the reaction force is:

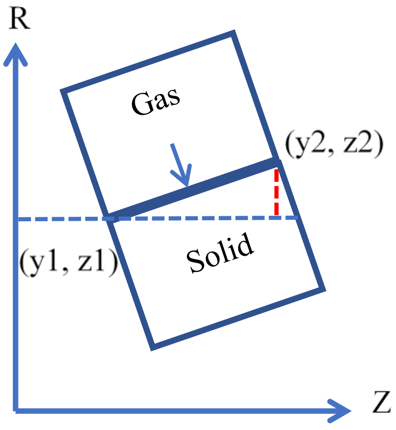

Figure 2.12 Diagram showing the gas cell is on the north face of the solid cell and the position of (y1, z1) and (y2, z2).

$$F_n = A_n \cdot \overrightarrow{V_{huz}} \cdot P_{gas} = P_n \cdot \pi({y_2}^2 - {y_1}^2) \tag{2.33}$$

After the elementary force on each face has been calculated, a net reaction force applied on a single cell is obtained and then added to the slab total reaction force. Once the loop through all slabs has been complete, the total reaction force of the whole field at the current time step is updated and then passed on to the driving mechanism model.

Figure 2.13 is the flow chart showing the logical structure of the subroutine as well as the execution sequence of the code. The subroutine is placed in the ground.for file at group 19, section 8 (explained in Section 2.2.3). This means the subroutine will be executed repeatedly at the end of every time step during a circuit breaker simulation. Currently the subroutine has one input, namely, the number of moving objects. Based on the geometry of the circuit breaker arcing chamber, the user has to manually provide PHOENICS with this information. Although the number of moving components differs from case to case, a method that can identify the number of moving object automatically may be favourable.

As can be seen in Figure 2.13, the subroutine should work in the following sequence:

1. With the user-defined input: number of moving components, loop through and record the boundary locations of every moving component.
2. Sweep the whole computational domain at the last sweep of each time step, slab by slab, i.e. from KZ=1 to NZ (where NZ is the number of slabs of the computational domain in Z-direction).
3. For each cell in each slab (i.e. let JY=1, NY, where NY is the total number of radial cells in a slab), identify whether it is in solid or gas regions. If it is in gaseous region, then set all four of its flag values to 0 and go to the next cell. If the cell is in solid region, then go to Point 4.
4. For each solid cell, compare its position with the boundary locations of moving objects obtained in step1, if this cell belongs to any moving solid object, set all flag values to 0 and move on to the next solid cell. If the cell does not belong to any moving components, move on to point 5.
5. For the rest of the solid cells, examine the PRPS value of its surrounding cells and then assign appropriate values to each of the flag variables.

6. Based on the flag values obtained in step 3, 4, 5, calculate the net reaction force in each cell.
7. Add the obtained cell value together to calculate the slab reaction force, then move on to the next slab and repeat step 3, 4, 5, 6.
8. After the last slab has been processed, sum all slab-wise reaction force to obtain the total net reaction force that is applied to the driving mechanism.
9. Output force and end.

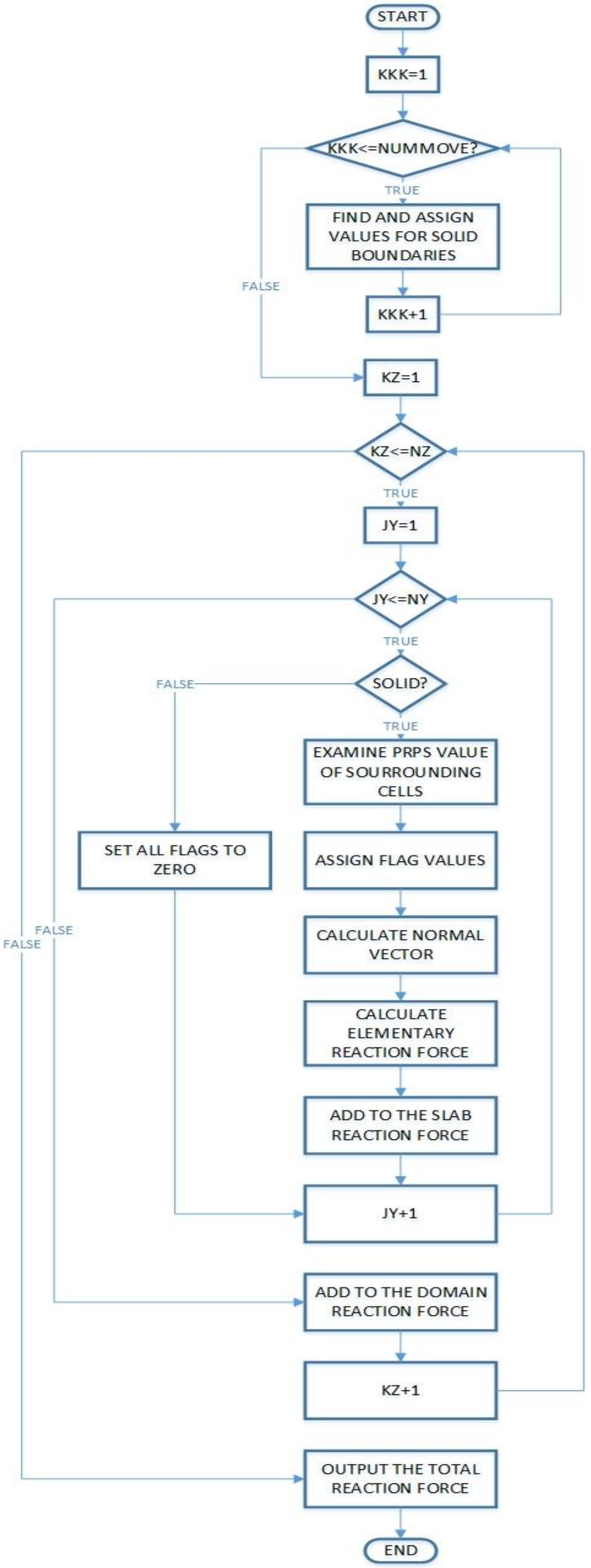

Figure 2.13 Flow chart showing the logical structure of the subroutine.

2.2.3 Coupled simulation interface design

After obtaining the value of reacting force, an interface between PHOENICS and driving mechanism solver is needed in order to exchange information. Coupled simulation cannot be performed without such interface.

Figure 2.14 explains the information exchange scheme between the arc model and driving mechanism solver. After solving arc governing equations, PHOENICS is able to predict the pressure distribution in the arc chamber. Upon obtaining this pressure distribution, together with the aforementioned method of calculating the reaction force, a PHOENICS subroutine is called to calculate the instantaneous reaction force. Considering the reaction force is not directly exerted on the driving mechanism, it is necessary to take the linkage mechanism (between arc chamber and driving mechanism) into consideration. If the linkage mechanism does not operate in a linear fashion, then additional equations should be formulated to convert the reacting force into the real force that is directly applied to the driving mechanism. In the meantime, with the instantaneous reacting force accounted for, the driving mechanism solver is responsible for calculating the speed and displacement of all moving components, movement of these components will in turn affect the pressure distribution in arc chamber, forming a complete information loop, which reflects the true interaction between the driving mechanism and the arc. Figure 2.15 illustrates the parameters exchanged (refer to Equation 3.29) between the two models.

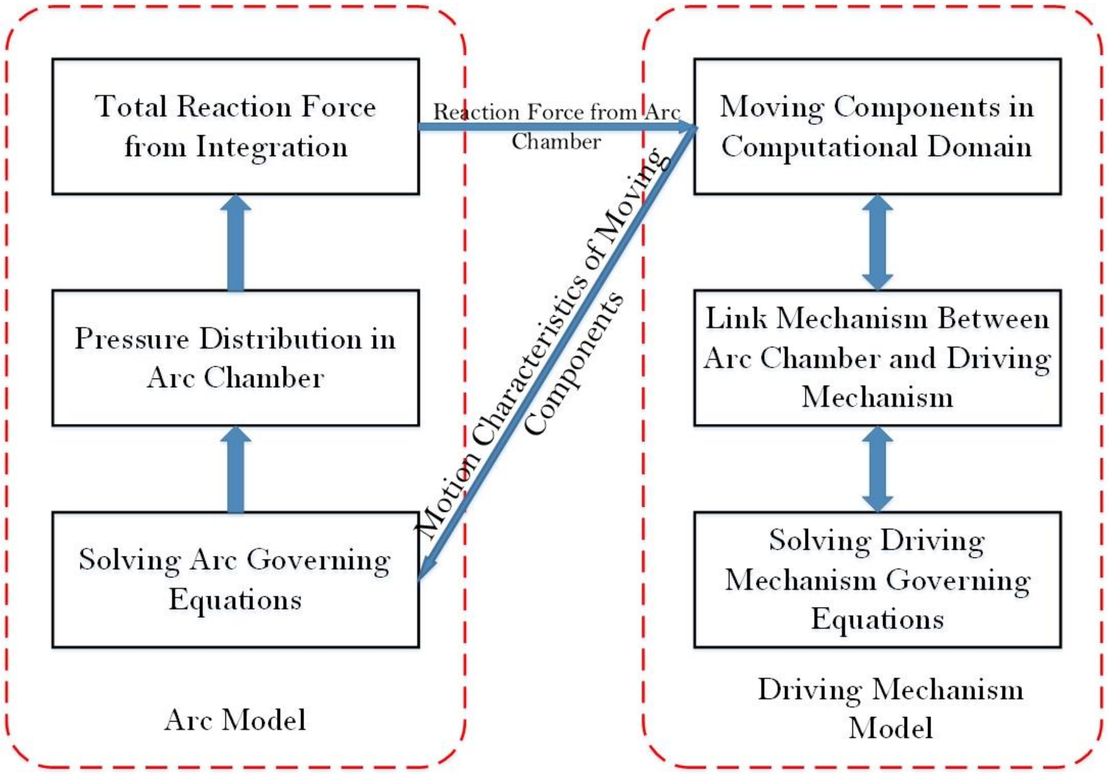

Figure 2.14 Interface between arc and driving mechanism model.

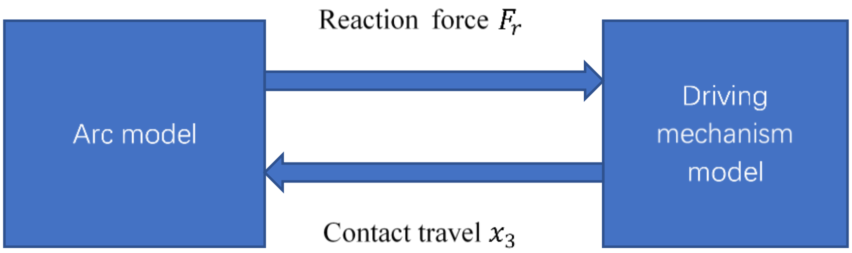

Figure 2.15 Parameters exchanged between the arc and driving mechanism model (refer to Equation 3.29).

In PHOENICS, a simulation process is divided into a sequence of time steps, as a result, theoretically, to achieve truly coupled simulation, the value of the reacting force and travel characteristics of moving components should be updated for every iteration within a time step. The code designed to calculate reaction force is organized into the form of a PHOENICS subroutine (an independent code module that can be called by PHOENICS) and placed in ground.for which is a file that contains a subroutine of the PHOENICS solver to provide interfaces for user-defined codes. The reaction force calculation subroutine is called at the end of each time step and the value of the reacting force will be updated accordingly.

The hydraulic driving mechanism model is formed by a system of ordinary differential equations (ODEs) which are complicated and non-linear in nature due to the interaction between various hydraulic components. Therefore, they cannot be solved analytically. Alternatively, they need to be solved numerically by applying a proper numerical method. After comparing with other numerical methods such as Dormand–Prince method (with the orders of 5) and Runge-Kutta Fehlberg method (with the orders of 7 or 8), the fourth-order Runge-Kutta method (RK4) was chosen as the numerical method in solving the mathematical model of the hydraulic system. This is because all three methods generate the same results, indicating the fourth-order Runge-Kutta method is accurate enough for this application and the fourth-order Runge-Kutta method requires the least computation time.

Solver for the driving mechanism model is compiled as DLL (Dynamic-Link Library) using an internal C++ command (“extern "C" _declspec(dllexport)”). This approach was adopted to take advantage of the “Boost” open source library [86] in which the sub-library “odeint” provides the subroutine of an ODE solver utilizing the fourth-order Runge-Kutta method. Since the ODE solver subroutine is coded in C++ and PHOENICS lacks the corresponding interface, the DLL approach provides a solution to the interface problem. Placing the DLL file under the corresponding PHOENICS root directory allows PHOENICS to call the solver. Based on the process mentioned above, PHOENICS is capable of calculating the travel and reacting force as well as exchanging the data automatically, the user only needs to provide appropriate initial conditions at the beginning of the simulation.

Within PHOENICS, the software into which the arc model is implemented, solution to the governing equations at each time step is obtained by an iterative process that is called sweeping, the details of which can be found in the PHOENICS handbook [87]. A true coupling of the two models will require the reacting force updated and the driving mechanism model solved to obtain the displacement of the moving components in each Sweep.

Theoretically a subroutine to calculate the reaction force and another subroutine to solve the driving mechanism model should be called at the beginning of each Sweep. This means two subroutines are called in the Start of Sweep section of Group 19 of the PHOENICS Ground subroutine, which consumes a significant amount of computing time. Therefore, instead of at the beginning of each sweep, the subroutines are called at the end of each time step. This leaves the accuracy of the current coupling method in question. This issue can be resolved by examining the typical change of reaction force and travel in a single time step. Given a typical circuit breaker simulation time step in PHOENICS is up to 10 μs, the calculation shows that, with a the fastest rate of change found during the simulation, the difference between travel at the beginning and end of a single time step is in the order of 1×10^{-5} m while the difference between reaction force in a similar scenario is in the order of 1×10^{1} N. In this example, the difference in travel and reaction force in a single time step amount to 0.015% and 0.013% of their instantaneous value (139.463 mm and 21485.2 N). This indicates that the change of travel and reaction force in a single time step can be safely ignored. Considering that the value of reaction force and travel will be updated at the end of each time step, the accumulative effect of inaccuracy introduced by the current coupling method is also quite limited. Thus, the accuracy of the current coupling method is considered to be acceptable.

Sections of ground.for which calls the hydraulic driving mechanism solvers are listed below:

1) CALL HDSOLVE(DT, TIM, ISTEP, XEM1, VEM1, XX1, VEL1, XX2, VEL2, PP2, XX3, VEL3, PP3, FRACTOTT)

Meaning of the parameters exchanged between the driving mechanism solver and

PHOENICS is explained in Table 2.2.

Table 2.2 Parameters exchanged between hydraulic driving mechanism and arc model.

Parameter	**Type**	**Mathematic Symbol**	**Variable Name (Solver)**	**Variable Name (PHOENICS)**
time step size	input	dt	a1	DT
current time	input	t	a2	TIM
current step	input	N/A	i	ISTEP
pilot valve displacement	output	x_1	AA1	XX1
pilot valve speed	output	v_1	AA2	VEL1
main valve displacement	output	x_2	AA3	XX2
main valve speed	output	v_2	AA4	VEL2
main valve control chamber pressure	output	P_{c2}	AA5	PP2
piston displacement	output	x_3	AA6	XX3
piston speed	output	v_3	AA7	VEL3
cylinder head port pressure	output	P_{c3}	AA8	PP3
reaction force	output	F_r	ractForce	FRACTOTT

The simulation time parameters (such as current time and time step size) are all provided by PHOENICS, this ensures the synchronicity of the coupled simulation.

2.3 Conclusion

The detailed governing equations of gas-blast arcs were introduced in this chapter. All arcing related phenomena such as radiation transfer, nozzle ablation, ohmic heating, Lorentz force, and turbulence enhanced momentum and energy transfer were explained. The methods used to incorporate these processes into the arc conservation equations were also presented in detail.

Based on the grid structure in PHOENICS and the geometrical feature of the circuit breaker arc chamber, an integral method was developed to calculate the reaction force imposed by high pressure gas in the arc chamber. The coupling mechanism and the accuracy of the coupling was also analyzed. In addition, interface between the driving mechanism model solver and arc model solver was also presented. Verification of the arc model and reaction force calculation method will be presented in Chapter 4.

Chapter 3 Mathematical Model of Hydraulic Driving Mechanisms

3.1 Introduction to Hydraulic Driving Mechanisms

A fluid power (mechanical power) system converts, transmits, controls or applies energy via a pressurized fluid (gas or liquid). Such systems can transmit enormous forces at variable speed with rapid reversing capabilities [88]. The main components of a conventional hydraulic driving mechanism are: hydraulic pump, oil reservoir, control valves, hydraulic cylinder, accumulator and control circuits. In order to achieve contact separation in a circuit breaker, upon receiving an electrical signal, the electrical signal is converted into a mechanical one via electromagnets and then magnified by multiple tiers of control valves. Finally, the hydraulic cylinder operates, the main piston is connected to all moving components in the arc chamber and it propels all of them to the open position. When the system is not in operation, the accumulators are top-upped on a regular basis to ensure the system can operate under appropriate pressure level. Compared with other types of driving mechanisms, hydraulic driving mechanisms has high output power, low response time, low noise, low maintenance requirement and long operational life.

3.2 Mathematical Model of the Hydraulic Driving Mechanism

The key issue in modelling the hydraulic driving mechanism is to construct a functional diagram representing the mechanical components comprising the driving mechanism. This functional diagram depends on the actual structure of the mechanical system (ZF-11-252 (L)/CYTA type hydraulic driving mechanism, provided by the collaboration company Pinggao Electrical Co. Ltd), and is presented in Figure 3.1. Differential equations are then to be derived to describe the dynamic characteristics of the system in response to a changing load. Approximations will be introduced to make the model implementable in the simulation package. However, all important approximations and assumptions are justified based on operational evidence or sound theoretical arguments to ensure that the results are not affected in any significant way.

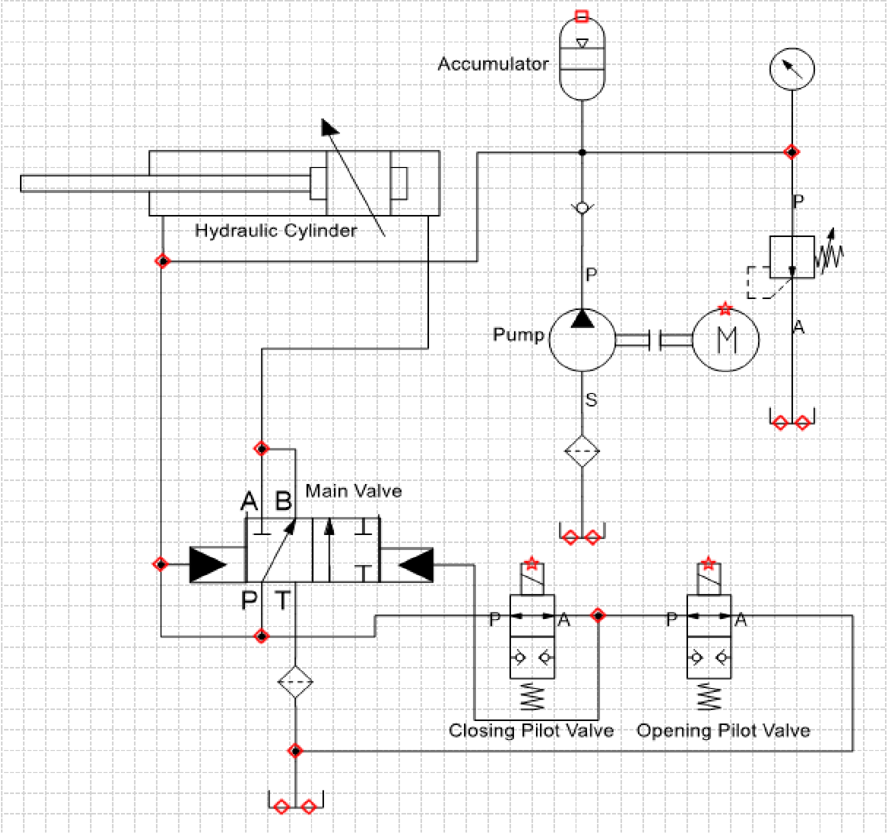

Figure 3.1 A functional diagram of the ZF-11-252 (L)/CYTA type hydraulic driving mechanism, the main components are: 1. closing pilot valve 2. opening pilot valve 3. hydraulic pump 4. accumulator 5. main valve 6. hydraulic cylinder.

3.2.1 Operating principle of the ZF-11-252(L)/CYTA hydraulic driving mechanism

The ZF-11-252 (L)/CYTA hydraulic driving mechanism prototype used in this project is a two-tiered system. The system in its closed (Figure 3.2 (a)) and opened (Figure 3.2 (b)) position is shown in Figure 3.2. It is worth pointing out that in this project, only the opening operation is of significant importance, arc-initiation and post-arc analysis are also included, but the closing operation is not examined. The modelling explained in detail in this chapter is based on the opening operation of the system.

Figure 3.2 depicts the basic process of an opening operation of the system: first the opening pilot valve operates upon receiving a signal, this leads to a pressure drop in the control chamber of the main valve. The main valve is then activated under the pressure difference created by the pilot valve, this leads to a pressure drop in the cylinder head port in a similar fashion. Oil in cylinder head port enters the main valve through orifice Z, and is then discharged to the low-pressure reservoir via orifice T. Based on the process mentioned above, the opening operation can be modelled mathematically**.**

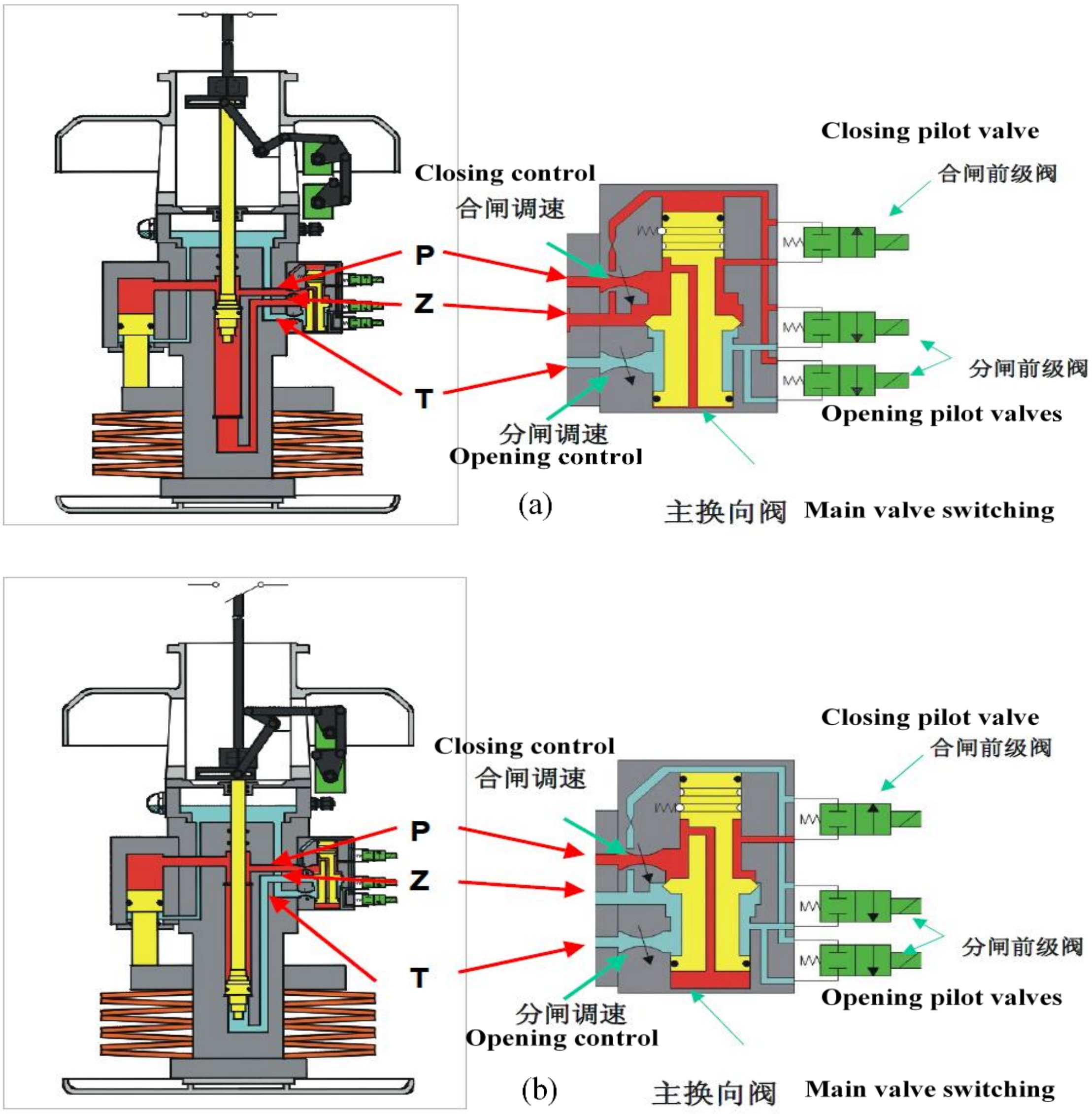

Figure 3.2 Real system diagram of the hydraulic driving mechanism in both closed (a) and opened (b) positions, flow directions of oil during closing and opening operations are shown in the diagram.

3.2.1.1 Operating principle of pilot valve

As can be seen in Figure 3.1, three pilot valves are installed in the system, one of them is dedicated to the closing operation and the rest are for opening operation (one as backup). Structure of the opening pilot valve is illustrated by Figure 3.3. Before the operation commences, the exit of the valve is blocked by a steel ball (component 18 in Figure 3.2). When the opening signal is received, the armature of the electromagnet pushes downwards and come into contact with the valve spool, together they push the steel ball and unblock the exit. Thus, oil in main valve control chamber can flow through the pilot valve to the reservoir. To model this process, the following aspects need to be considered:

a) Movement of the valve spool (component 16 Figure 3.3), which affects the instantaneous flow rate through the valve orifice.

b) The flow rate through the valve orifice, which in turn affects the pressure in main valve control chamber and the movement of the pilot valve spool.

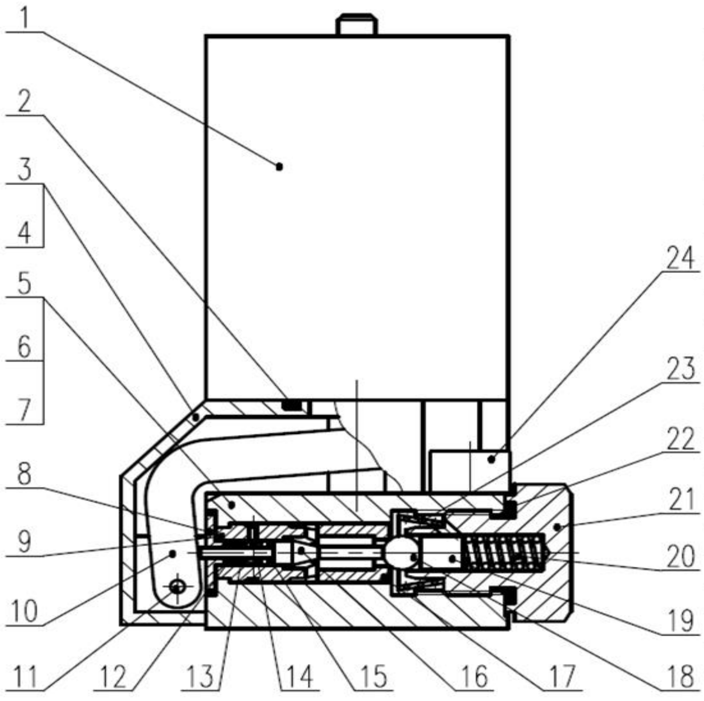

1	Solenoid assembly
2	O-ring seal
3	Base plate
4	M3*8 bolt
5	Valve plate
6	M4*20 bolt
7	9.5*1.9 O-ring seal
8	Top cap
9	Valve sleeve
10	Lever
11	Hinge pin
12	Check ring
13	O-ring seal
14	Valve sleeve
15	Top cap
16	Valve pin
17	Valve sleeve
18	4.0 Steel ball
19	Spring retainer
20	Reset spring
21	Plug
22	O-ring seal
23	Cover
24	M5*25 bolt

Figure 3.3 Schematic of pilot valve-solenoid assembly.

3.2.1.2 Operating principle of the solenoid

Used as an actuator, the solenoid initiates the operation of pilot valves, according to data provided by the manufacturer, the typical response time of the solenoid is 3 ms. Structure of the solenoid is shown in Figure 3.4.

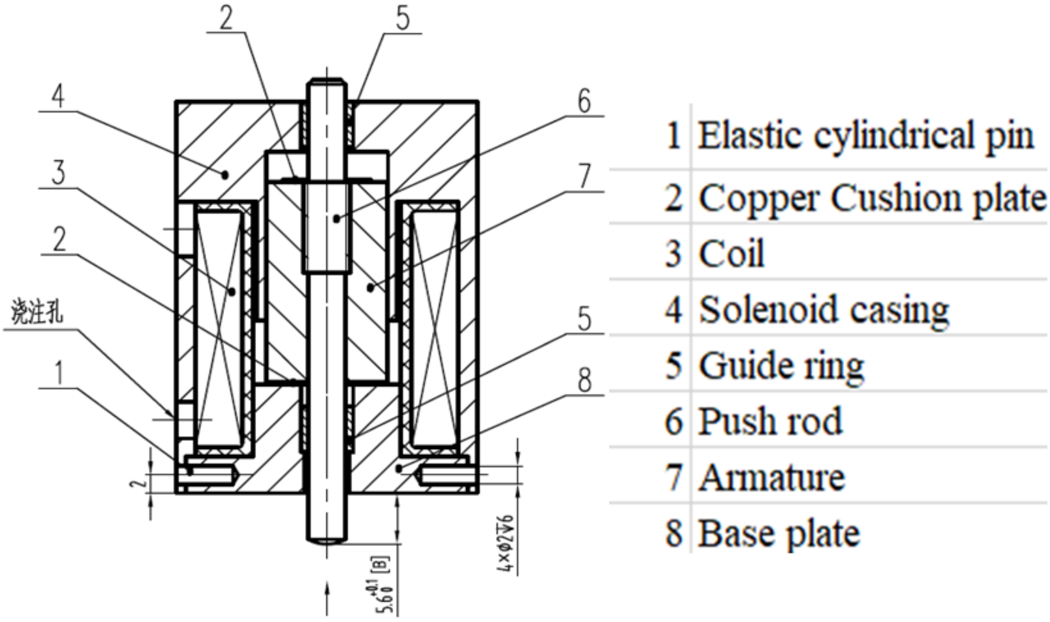

Figure 3.4 Schematic of the solenoid.

The basic operating principle for the solenoid is: the coil converts electric energy into magnetic energy and stores it in the magnetic circuit (permeability of air far smaller than other ferrous material in the magnetic circuit, therefore, the majority of magnetic energy is stored in the air gap), this energy is then released in the form of magnetic force which then propels the armature to create desired motion.

3.2.1.3 Operating principle of the main valve

Figure 3.5 shows the structure of the main valve. When opening operation commences, the pilot valve opens, creates a pressure difference across the spool of the main valve. The spool then moves towards its open position to establish a flow channel for the hydraulic cylinder to discharge. To model this process, the following aspects need to be considered:

a) Pressure change in the control chamber of the main valve.

b) Opening process of orifice Z.

c) The instantaneous flow rate through orifice Z.

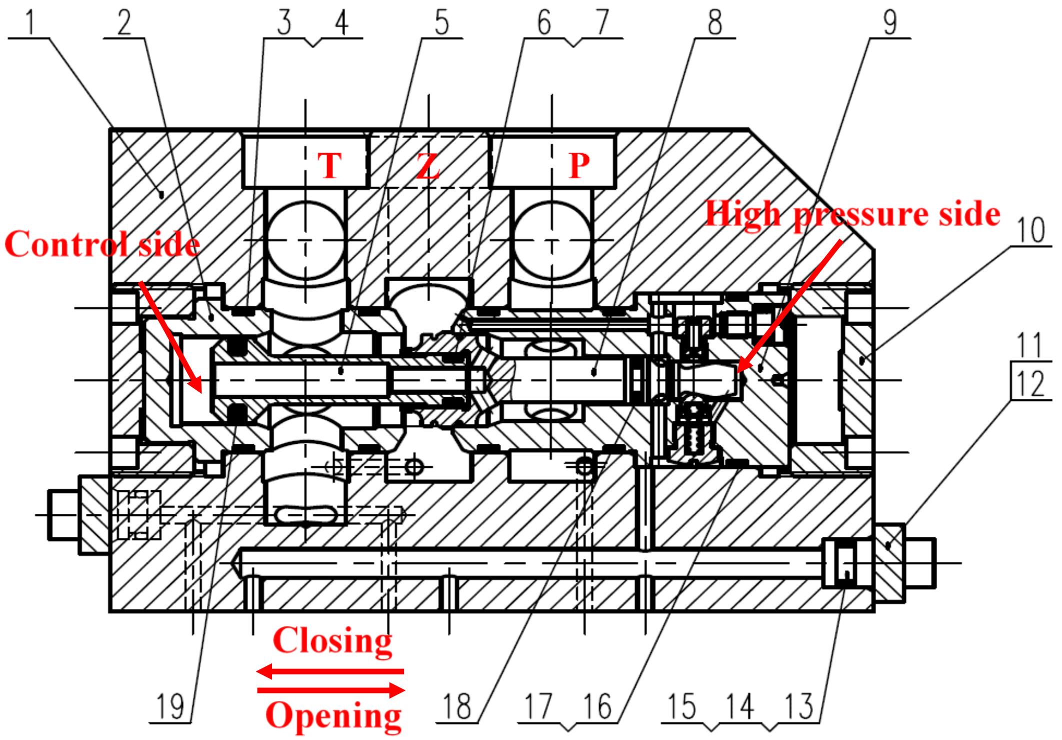

1	Valve housing	5	Valve spool	9	Valve sleeve assmbely	13	Plug	17	36*33*1.25 Check ring
2	Valve sleeve	6	O-ring seal	10	Plug	14	10*1.9 O-ring seal	18	PT0000100-T46N Glyd ring
3	30*1.9 O-ring seal	7	11*8*1.25 Check ring	11	End plate	15	10*1.25 Check ring	19	PT0100180-T46N Glyd ring
4	30*27*1.25 Check ring	8	Valve spool	12	M8*16 Bolt	16	36*1.9 O-ring seal		

Figure 3.5 Schematic of the main valve.

3.2.1.4 Operating principle of the main hydraulic cylinder

Figure 3.6 shows the structure of the main hydraulic cylinder. In opening operation, oil in the head port is discharged through the main valve, due to the resulting pressure difference, the piston will move to the open position, together with all moving components that are connected to the piston via the connecting rod. Several aspects need to be considered during modelling:

a) Pressure change in cylinder head port.

b) Movement of the piston-rod assembly.

c) Cushion system which slows down the piston near the end of travel.

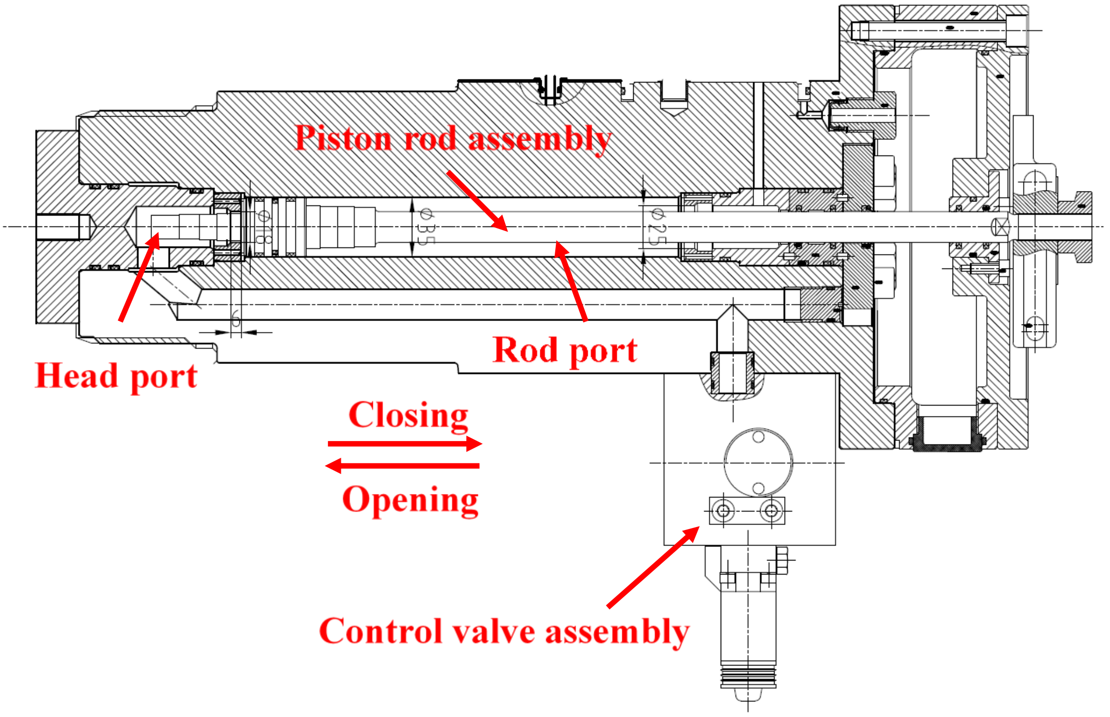

Figure 3.6 Schematic of the hydraulic cylinder.

3.2.2 Governing equations of the opening process of the ZF-11-252(L)/CYTA hydraulic driving mechanism

3.2.2.1 Equations of pilot valves

The pilot valve is actuated by its attached solenoid. During its operation, the valve spool is subjected to friction and the resistive force generated by the reset spring. The reset spring is used to:

a) When the pilot valve is closed, the pre-load force on the spring ensures the steel ball blocks the valve exit completely, this will prevent any leakage in the system.

b) When the spool is moving towards the end of travel, the re-set spring provides a certain level of cushion, this will keep the components from being damaged and reduce mechanical impact to a minimum.

Displacement and velocity of the pilot valve pin can be calculated based on basic dynamics. Applying Newton's second law considering all forces acting on the valve pin results in:

$$m_1 \frac{d^2 x_1}{dt^2} = F_m - F_{v1} - F_{s1} \tag{3.1}$$

$$v_1 = \frac{dx_1}{dt} \tag{3.2}$$

where m_1 is the total mass of moving components including valve spool and steel ball, v_1 is the velocity of valve spool, F_{v1} is the frictional force experienced by the valve spool during its movement, this can be quantified as: $F_{v1} = B_{v1} dx_1/dt$, B_{v1} is the viscous friction coefficient, F_{s1} is the resistive force generated by the re-set spring, this force is governed by hook's law, which writes: $F_{s1} = kx_1 + F_{s10}$. k is the stiffness of the spring, F_{s10} is the pre-load force on the spring and F_m is the driving force generated by the solenoid.

Considering most orifice flow occurs at high Reynolds numbers where the flow is turbulent, in this case, the pressure drop across the orifice can be contributed to the acceleration of fluid particles from upstream velocity to the higher jet velocity at downstream. The pressure difference required to accelerate fluid particles from a typical upstream velocity (v_u) to the downstream jet velocity (v_d, velocity measured at the vena contracta, where the diameter of the jet is the least and the fluid velocity is at its maximum) can be found by applying Bernoulli's equation [89]:

$${v_u}^2 - {v_d}^2 = \frac{2}{\rho}(P_u - P_d) \tag{3.3}$$

where P_u and P_d are the upstream and downstream pressure respectively, and ρ is the density of hydraulic oil. In the case of the pilot valve, it connects the main valve control chamber (with a pressure of P_{c2}) with the low-pressure reservoir (with a pressure of P_{back}). Therefore, the instantaneous low rate through the pilot valve orifice is written as:

$$Q_1 = C_{d1} A_{v1} \sqrt{\frac{2(P_{c2} - P_{back})}{\rho}} \tag{3.4}$$

where P_{c2} is the pressure inside the control chamber of the main valve, which is calculated by another governing equation, P_{back} is the back pressure, which is equivalent to the oil pressure inside reservoir. For the system under investigation, assuming the height of the reservoir does not exceed 1 meter, then the maximum oil pressure inside reservoir is $P_{back} = \rho g h = 8330\ \mathrm{Pa}$, compared with the pressure which the system operates at (45 MPa), the back pressure can be safely ignored. A_{v1} is the instantaneous orifice area which is a function of spool displacement: according to the orifice structure depicted in Figure 3.7, A_{v1} can be calculated using:

$$A_v = \pi r_o D \left(1 - \frac{{r_b}^2}{D^2}\right) \tag{3.5}$$

$$D = \sqrt{\left(\sqrt{{r_b}^2 - {r_o}^2} + x\right)^2 + {r_o}^2} \tag{3.6}$$

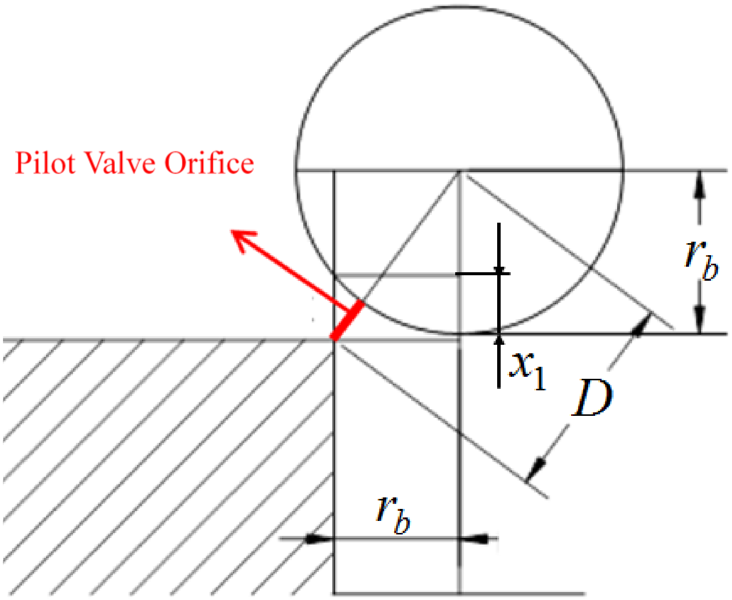

Figure 3.7 Pilot valve orifice area calculation. Dimensions in Equations (3.5) and (3.6) are marked in the diagram.

Finally, C_{d1} is the discharge coefficient of the pilot valve orifice. Generally, the discharge coefficient is a dimensionless coefficient and can be expanded into:

$$C_d = \frac{C_v A_d}{\sqrt{1-(A_d/A_u)^2}} \tag{3.7}$$

where C_v is the velocity coefficient introduced to account for the speed reduction (due to viscous effect) of the flow between upstream and vena contracta. To relate the cross-section area of the flow at vena contracta (A_d) to the orifice area (A_v), a contraction coefficient is needed:

$$C_c = \frac{A_d}{A_v} \tag{3.8}$$

so the discharge coefficient becomes:

$$C_d = \frac{C_v C_c}{\sqrt{1 - {C_c}^2 (A_v/A_u)^2}} \tag{3.9}$$

It can be seen that the discharge coefficient is representative of two effects:

a) The speed reduction of the flow caused by viscous friction.

b) The contraction effect caused by the fact that in most valve applications, the orifice area A_v is considerably smaller than the upstream flow area (A_u).

Many have proved that due to the small scale of modern hydraulic components, the effect of viscous friction between upstream and vena contract is negligible [90], bring the value of C_v to unity. The contraction coefficient on the other hand, is dependent on orifice geometry, Reynolds number and the extent to which cavitation occurs downstream of the orifice. As a result, the discharge coefficient is commonly determined through measurements. Although the discharge coefficient varies with Reynolds number [91], it has been found that for a fully developed turbulent flow, experimental evidence shows that the coefficient can be considered constant with respect to the Reynolds number [92]. Considering the flow in hydraulic control valves is largely turbulent, the use of a single Reynolds number is justified (with the assumption of a fully developed turbulent, Newtonian, incompressible flow). Experiments conducted by both von Mises [93] and Stone [94] have confirmed that for poppet valves (the pilot valve used in the system can be considered as a type of poppet valve), in terms of orifice geometry, the discharged coefficient is related to the poppet angle. At 45-degree poppet angle, value of the discharge coefficient is found to be 0.63.

3.2.2.2 Output force of the solenoid

Both resistance and inductance contribute to the voltage drop across the coil. Therefore, the total voltage drop is:

$$V = Ri + \frac{d\lambda}{dt} \tag{3.10}$$

where R is the resistance of the coil, i is current, λ is the magnetic linkage, which is affected by both the current i and the length of air gap x. Since λ is a function of

i and x, Equation (3.10) can be rewrite as:

$$V = Ri + \frac{\partial\lambda(i,\ x)}{\partial i}\frac{di}{dt} + \frac{\partial\lambda(i,\ x)}{\partial x}\frac{dx}{dt} \tag{3.11}$$

The first term on the right-hand side of Equation (3.11) represents the voltage drop caused by winding resistance, while the second term represents the induced electromotive force caused by coil magnetic field, the last term is the so-called motion electromotive force generated by the moving armature.

In a self-inducting circuit, the magnetic linkage can be written as:

$$\lambda(i,\ x) = L(i,\ x)\cdot i \tag{3.12}$$

Therefore, Equation (3.11) can be further expanded into:

$$V = Ri + L\frac{di}{dt} + i\frac{dL}{dx}\frac{dx}{dt} \tag{3.13}$$

In terms of energy, the output force of the solenoid is a gradient of the co-energy stored in the magnetic circuit. Thus, the output force of the solenoid is:

$$F_m = \frac{\partial E(i,\ x)}{\partial x} \tag{3.14}$$

where F_m is the output force of the solenoid, E is the co-energy stored in the magnetic circuit, x is the length of the air gap. In its essence, co-energy is magnetic linkage integrated over current, co-energy can be expressed as:

$$E(x,\ i) = \int_0^i \lambda(i,\ x)di \tag{3.15}$$

Since x and i are independent variables, they can be differentiated under the integral sign, then the output force becomes:

$$F_m = \int_0^i \frac{\partial\lambda(i,\ x)}{\partial x}\Big|_{i=const} di \tag{3.16}$$

In order to obtain the instantaneous value of F_m in a very small duration, x should be treated as a constant (since the characteristic time of mechanical systems is far larger than electrical systems):

$$F_m = \frac{\partial\lambda(i,\ x)}{\partial x}\cdot i \tag{3.17}$$

In terms of mechanical characteristics, the armature of the solenoid together with the pilot valve spool can be treated as a single-mass spring system, whose dynamic behaviour is governed by:

$$mx_p'' = F_m - B_{p1}x_p' - kx_p \tag{3.18}$$

where m is the mass of all moving components, x_p is the displacement of the moving mass assembly. Depending on the structure of the solenoid, length of the air gap x is a function of x_p.

$$x = f(x_p) \tag{3.19}$$

Together, Equations (3.17) and (3.18) are the governing equations of the solenoid. Solving these equations simultaneously requires $\frac{\partial\lambda}{\partial x}$ and $\frac{\partial\lambda}{\partial i}$, information that should be made available by the manufacturer. Interpolation can be used in order to produce a continuous output profile of the solenoid.

3.2.2.3 Equations of the main valve

Based on previous discussions, during an opening operation, the pressure inside the control chamber of the main valve depends on the instantaneous flow rate through pilot valve orifice. In addition, movement of the main valve spool itself will also affect this pressure.

The thermal expansion coefficient of the hydraulic fluids is generally small (for aviation hydraulic fluid it is 0.0005 1/°C). Therefore, it is reasonable to assume that isothermal conditions exist in the flow. Consequently, instead of writing:

$$\rho = f(P, T) \tag{3.20}$$

with a constant temperature, the equations of state can be reduced to:

$$\rho = \rho_i + \frac{\rho_i}{\beta}P \tag{3.21}$$

where ρ_i and β are the mass density and bulk modulus of the fluid at zero pressure. With this simplification, the continuity equations can be written as:

$$\sum W_{in} - \sum W_{out} = g\rho\frac{dV_0}{dt} + gV\frac{d\rho}{dt} \tag{3.22}$$

where W are mass flow rates and $W = g\rho Q$. Therefore, based on volumetric flow rate, the continuity equation combined with equatthe ion of state gives:

$$\sum Q_{in} - \sum Q_{out} = \frac{dV_0}{dt} + \frac{V_0}{\beta}\frac{dP}{dt} \tag{3.23}$$

After rearranging, the control chamber pressure is determined by:

$$\frac{dP_{c2}}{dt} = \frac{\beta}{V_{c2}}(A_{c2}x_2' - Q_1) \tag{3.24}$$

where β is the bulk modulus of hydraulic oil, V_{c2} is the instantaneous volume of the control chamber, which is a function of main valve spool displacement, x_2 is main valve spool displacement and Q_1 is the flow rate through pilot valve, which is calculated by Equation (3.4)

Similar to the pilot valve, the motion of main valve spool is also determined by dynamic equations. Based on the information offered by Figure 3.5, the dynamic equations for the main valve can be written as:

$$m_2\frac{d^2x_2}{dt^2} = P_{h2}A_{h2} - P_{c2}A_{c2} - F_{v2} \tag{3.25}$$

$$v_2 = \frac{dx_2}{dt} \tag{3.26}$$

where m_2 is the mass of main valve spool assembly, x_2 is main valve spool displacement, v_2 is main valve spool velocity, F_{v2} is the frictional force exerted on main valve spool, it can be characterized by: $F_{v2} = B_{v2}dx_2/dt$, in which B_{v2} is the viscous friction coefficient of valve spool, P_{h2} and P_{c2} are the pressure inside main valve high-pressure and control chamber respectively, finally, A_{h2} and A_{c2} are the effective area of the spool on high-pressure and control side respectively.

Similarly, the flow rate through main valve orifice is:

$$Q_2 = C_{d2}A_{v2}\sqrt{\frac{2(P_{c3}-P_{back})}{\rho}} \tag{3.27}$$

where C_{d2} is the discharge coefficient of main valve orifice, P_{c3} is the pressure inside cylinder head port, P_{back} is the back pressure, A_{v2} is the main valve orifice area which is a function of main valve spool displacement.

3.2.2.4 Equations of the main hydraulic cylinder

During opening operation, the pressure inside cylinder head port is determined mainly by the flow rate through main valve and the movement of the piston itself:

$$\frac{dP_{c3}}{dt} = \frac{\beta}{V_{c3}}(A_{c3}x_3{}' - Q_2) \tag{3.28}$$

where V_{c3} is the instantaneous volume of cylinder head port, which is calculated by: $V_{c3} = V_{c30} - A_{c3}x_3$, in which V_{c30} is the initial volume of cylinder head port, Q_2 is the main valve flow rate, which is calculated by Equation (3.27)

The dynamic equation for the piston can be written in a similar fashion to pilot and main valve spools:

$$m_3\frac{d^2x_3}{dt^2} = P_{h3}A_{h3} - P_{c3}A_{c3} - F_{v3} - F_r \tag{3.29}$$

$$v_3 = \frac{dx_3}{dt} \tag{3.30}$$

where m_3 is the total mass of piston-rod assembly and any other moving object in the arc chamber attached to the connecting rod, x_3 is the displacement of the piston, F_{v3} is the frictional force on the piston during its movement, which is calculated by $F_{v3} = B_{v3}dx_3/dt$, P_{h3} is the rod port pressure while P_{c3} is the head port pressure, A_{h3} and A_{c3} are the effective area of the piston on rod and head side respectively and F_r is the reacting force from arc chamber which is calculated by another PHOENICS subroutine.

In order to slow down the piston near the end of its travel and reduce the mechanical impact, an internal cushion system is installed in the hydraulic cylinder, its detailed structure can be seen in Figure 3.8. Near the end of travel, when the cushion spear (located on the piston) enters the cushion seal, the flow channel through which oil can leave cylinder head chamber is drastically reduced, this will result in a pressure rise in cylinder head port creating an opposing force and effectively slows down the piston. At this critical moment, the cross-sectional area of the flow channel formed by the cushion spear and seal is crucial in calculating the head port pressure P_{c3}, and since the spear is step shaped, this critical cross-sectional area changes with the piston displacement. Diameter of each step of the cushion spear and the corresponding piston displacement is shown in Table 3.1.

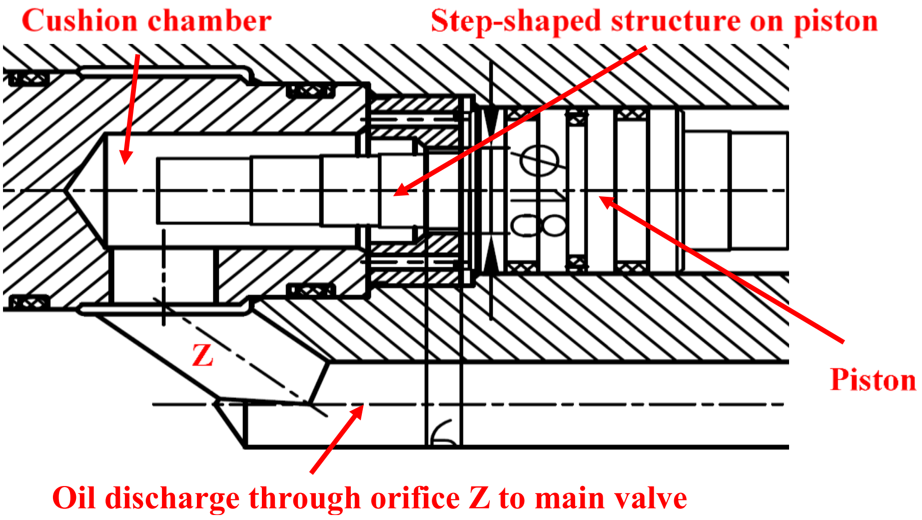

Figure 3.8 Diagram depicting the cushion system.

Table 3.1 The change of throttling area in the cushioning process with the change in piston displacement.

$x_3 < 168\ mm$	$A_{v2} = wx_2$
$168\ mm < x_3 \leq 174\ mm$	$A_{v2} = 52.12\ mm^2$
$174\ mm < x_3 \leq 182\ mm$	$A_{v2} = 38.25\ mm^2$
$182\ mm < x_3 \leq 192\ mm$	$A_{v2} = 30.44\ mm^2$
$192\ mm < x_3 \leq 204\ mm$	$A_{v2} = 28.12\ mm^2$
$204\ mm < x_3 \leq 220\ mm$	$A_{v2} = 26.69\ mm^2$

Based on the data presented in Table 3.1. A continuously changing cross-sectional area of the flow channel can be plotted against piston displacement using linear interpolation. Figure 3.9 shows in a typical case; the flow channel area gradually decreases as the piston travels further. Also included in Figure 3.9 is the pressure profile in cylinder head port. It can be observed that during the cushion period, pressure in the cylinder head port rises significantly. As the cushion spear and seal forms an annular orifice, the same equations (Equations (3.24) and (3.28)) derived to calculate the flow rate through valve orifices can also be used in the cushion stage, although as the flow channel area is significantly smaller than a fully opened valve orifice, different discharge coefficients should be used.

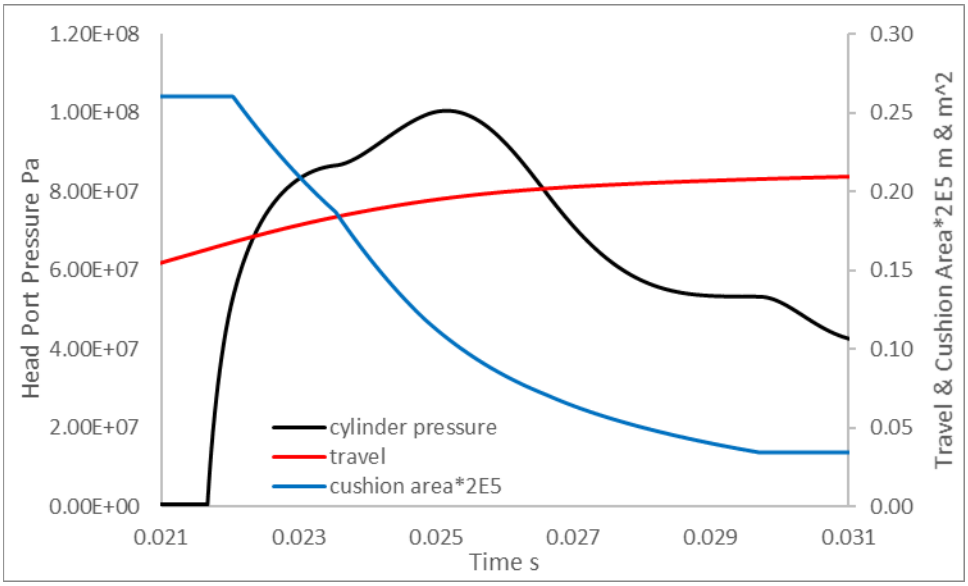

Figure 3.9 The profile of cylinder head port pressure, piston travel and cushion area in a typical cushion process.

Differential equations involved in the hydraulic driving mechanism model are summarized in Table 3.2 so the total number of unknown variables as well as the order of the system can be clarified.

Table 3.2 Differential equations involved in the driving mechanism model.

Component	Equations	Unknown Variable
Pilot Valve	$m_1\frac{dv_1}{dt} = F_m - F_{v1} - F_{s1}$	v_1
	$v_1 = \frac{dx_1}{dt}$	x_1
Main Valve	$\frac{dP_{c2}}{dt} = \frac{\beta}{V_{c2}}(A_{c2}x_2' - Q_1)$	P_{c2}
	$m_2\frac{dv_2}{dt} = P_{h2}A_{h2} - P_{c2}A_{c2} - F_{v2}$	v_2
	$v_2 = \frac{dx_2}{dt}$	x_2
Cylinder	$\frac{dP_{c3}}{dt} = \frac{\beta}{V_{c3}}(A_{c3}x_3' - Q_2)$	P_{c3}
	$m_3\frac{dv_3}{dt} = P_{h3}A_{h3} - P_{c3}A_{c3} - F_{v3} - F_r$	v_3
	$v_3 = \frac{dx_3}{dt}$	x_3

The connections between each component in terms of their effect on other components during the solution of these equations are highlighted in Figure 3.10.

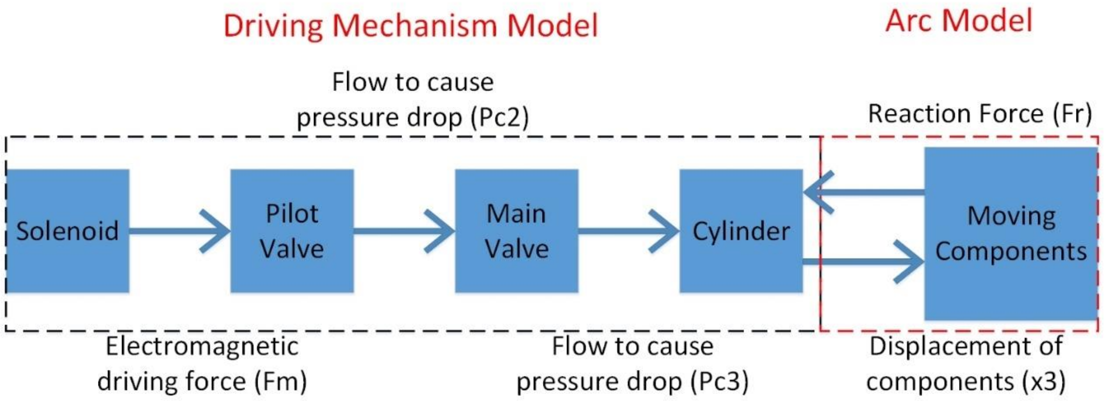

Figure 3.10 The block diagram of the ZF-11-252 (L)/CYTA hydraulic driving mechanism.

Values of all other parameters involved in the hydraulic driving mechanism model is listed in Table 3.3.

Table 3.3 Parameters used in hydraulic driving mechanism model.

No	**Parameters of Hydraulic Oil**		
1	ρ	density	850 kg/m^3
2	β	bulk modulus	1.6×10^9 Pa
Parameters of Solenoids			
3	μ_0	Permeability of air	1.26×10^{-6} N/A^2
4	N	Number of turns	2200
5	I	coil current	2 A
6	S	cross-sectional area of the magnetic circuit	1.77 mm^2
7	g_0	initial air gap length	2 mm
Parameters of Opening Pilot Valve			
8	m_1	the total mass of moving components	0.013 kg
9	Ps	system oil pressure	45 MPa
10	r_b	steel ball diameter	2 mm
11	r_0	orifice diameter	1.55 mm
12	B_{V1}	viscous friction coefficient	100 N/(m/s)
13	k_{V1}	stiffness of re-set spring	10.14 N/mm

14	$F_{S1}(0)$	pre-load force on re-set spring	0.1 N
15	C_{d1}	discharge coefficient	0.63
16	$\mathrm{P_{back}}$	back pressure	not considered
Parameters of Main Valve			
17	m_2	the total mass of moving components	0.4 kg
18	P_{h2}	pressure in the high-pressure chamber	45 MPa
19	A_{h2}	high-pressure side spool area	50.27 mm^2
20	A_{C2}	control side spool area	215.98 mm^2
21	V_{C20}	initial control chamber volume	3300 mm^3
22	B_{V2}	viscous friction coefficient	100 N/(m/s)
23	C_{d2}	discharge coefficient	0.7
24	$\mathrm{P_{back}}$	back pressure	8330 Pa
Parameters of Hydraulic Cylinder			
25	m_3	total mass of moving components	25 kg
26	P_{h3}	cylinder head port pressure	45 MPa
27	A_{h3}	piston rod side area	770.00 mm^2
28	A_{C3}	piston head side area	962.11 mm^2
29	V_{C30}	initial volume of head port	320000 mm^3
30	B_{V3}	viscous friction coefficient	1250 (m/s)

The hydraulic driving mechanism. Verification of the driving mechanism model will be presented in Chapter 4.

3.3 Key Parameters in Hydraulic Driving Mechanism

In order to determine the design parameters that have the most impact on the travel characteristics of the cylinder piston, a number of design parameters are selected and set to deviate from their standard value by a fixed percentage (increase by 10%, 20% and also decrease by the same percentage) in a number of sensitivity studies while all other parameters and conditions remain unchanged. By examining their impact on the travel characteristics, their importance can be evaluated. Standard values of all parameters involved in the study are presented as in Table3.2. Since this study is aimed at identifying the key design parameters within the driving mechanism, the reaction force from the arc chamber is not considered (arc chamber parameters that could potentially affect the magnitude of reaction force will be presented in Chapter 5). The total operation time of the driving mechanism is defined as the total time needed by the system to complete the entire travel (total trip time) subtracted by the initial delay time (see Figure 3.11). The relationship between this total operation time and other parameters is an important indicator while evaluating the performance of a driving mechanism.

3.3.1 Total mass of moving components

With other conditions remain the same, the system outputs the same force, altering the mass of the moving components (including piston-rod assembly, linkage system and the moving components in the arc chamber) effectively changes the load that the system is carrying throughout the operation. It is easy to predict that a heavier load will result in the system taking a longer time to finish the same travel and vice versa. Ideally, a shorter operation time of the system can be achieved by using lighter (whilst maintaining the structural strength) material, this is demonstrated by travel curves obtained with different load masses shown in Figure 3.11. By examining the data, it can be seen that all travel curves in this case all have the same amount of delay since other components (pilot and main valves) in the system are not affected and together they determine the duration of the delay. With a standard load (25.0 Kg), the initial delay is 2.0 ms and the 220 mm travel is finished at t=39.9 ms, making the total trip time of 37.9 ms. For 10% and 20% heavier loads (27.5 and 30.0 Kg), the total trip time is 38.4 and 38.8 ms, an overall time increase of 1.3% and 2.4% respectively. On the other hand, for 10% and 20% lighter loads, the total travel times are 37.4 and 36.9 ms. The results show that a 10% increase in load mass does not equate to 10% increase in total travel time, since the system is non-linear in nature. However, the increase and decrease mass by the same amount does have the same amount of impact on the total travel time, albeit in the opposite direction.

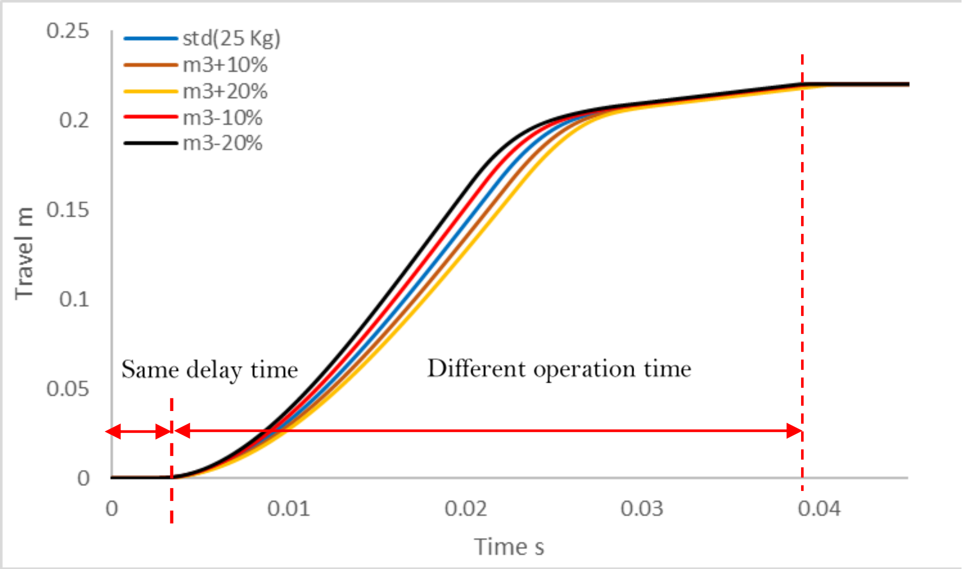

Figure 3.11 Travel curves obtained with different load masses: 25.0, 27.5, 30.0, 22.5 and 20.0 Kg.

It is worth noticing that although the change in mass was carried out incrementally, with each increment, the impact (in terms of total travel time) is getting less renowned. This can be illustrated by further increasing the total mass of the load (up to 100%) with the same increment. For each different mass (from 25.0 to 50.0 Kg), an actual distance travelled at t=20.0 ms is recorded and then compared with the distance travelled assuming a constant rate of reduction (caused by the increase of load mass). This comparison is featured in Figure 3.12.

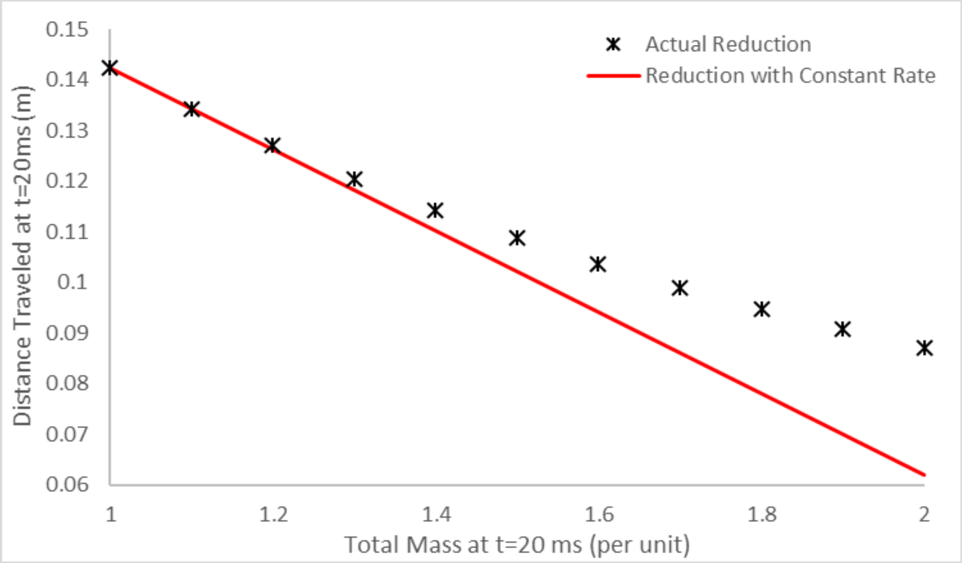

Figure 3.12 Diagram comparing the actual effect of load mass increase with an

imaginary constant rate of decrease in distance travelled. Comparison made at t=20.0 ms.

It can be seen that with the further increase in load mass, the effect (in terms of travel) diminishes. The same can be said for mass reduction, after the initial impact, further reduced the load mass will have little impact on the total operation time of the system.

In terms of piston speed, with the standard mass, the piston is able to achieve the maximum speed of 12.6 m/s at t=13.8 ms, as shown in Figure 3.13. Also shown in Figure 3.13 is the fact that with a lighter load, the piston is able to reach higher top speed (12.9 and 13.2 m/s for 10% and 20% mass reduction respectively). In addition, it can be observed that the lighter the load, the sooner the top speed is achieved (t=12.4 ms and t=10.8 ms for 10% and 20% mass reduction respectively). Conversely, for greater load masses, the top speed is 12.4 and 12.1 m/s for 10% and 20% cases, reached t=15.3 ms and t=16.3 ms respectively.

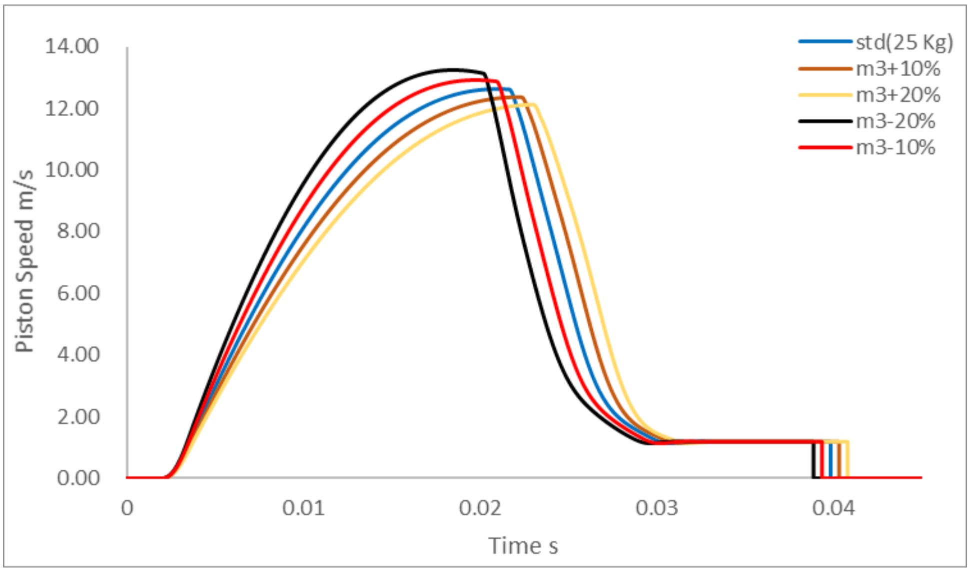

Figure 3.13 Piston speed obtained with different load masses: 25, 27.5, 30, 22.5 and 20 Kg.

Counterintuitively, the lightest load which resulted in the highest contact speed does not cause the highest pressure-rise in the cushioning process. This is reflected by the pressure profiles in Figure 3.14. In this case, compared with the standard result, the maximum pressure achieved (100.21 MPa for the standard case) is considerably lower at only 84.13 MPa. This indicates that apart from shortening the system operation time, reducing the load mass has the additional benefit of limiting the pressure-rise during the cushioning process. Excessive pressure-rise in the system results in severe mechanical stress and could potentially damage components and affect the longevity of the system adversely.

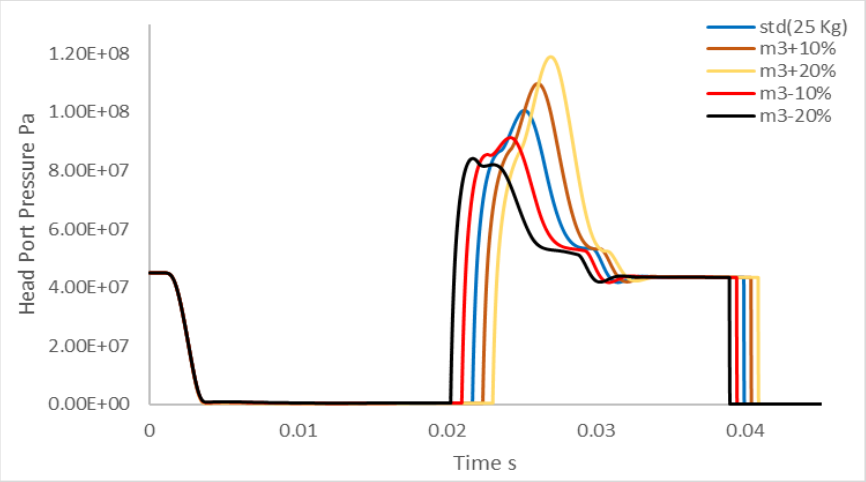

Figure 3.14 Pressure profiles obtained with different load masses: 25, 27.5, 30, 22.5 and 20 Kg.

3.3.2 System pressure

The standard operating pressure of the system is 45 MPa. Since the system is compact enough that any frictional and local pressure loss along the connecting pipelines can be safely ignored. As shown in Figure 3.15, changing the system pressure has a significant impact on the dynamic characteristics of the driving mechanism. The operation time is shortened by increasing the system pressure and lengthened by reducing it. Notice the effect of change in operating pressure is not limited to the main hydraulic cylinder, instead it has an overall effect on all components in the system. This means each different operating pressure corresponds to a different delay time, but since the overall response times of the pilot and main valve are small, the change in delay time for the cylinder is barely noticeable (0.06 ms difference between the most extreme cases) and from a design perspective, not worth considering. In terms of system total operation time, with a 20% increase in system pressure, the piston managed to complete the 220m travel in 36.5 ms, with a 2.1 ms delay time, making the total trip time 34.3 ms which is

9.5% faster than the original time. A 20% decrease in system pressure resulted in a 43.9 ms travel time. Compared with the earlier study, this indicates that the system operation time is more sensitive to change in system pressure than load mass.

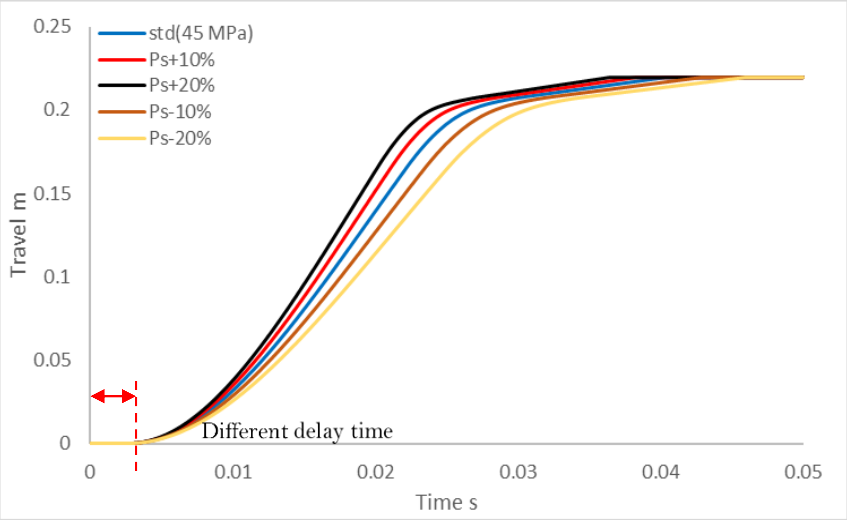

Figure 3.15 Travel curves obtained with different system pressures: 45.0, 49.5, 54.0, 40.5 and 36.0 MPa.

By using the same comparison used in the load mass study, it can be shown that the effect of increasing or decreasing system pressure also ‘saturates’, the comparison is demonstrated in Figure 3.16.

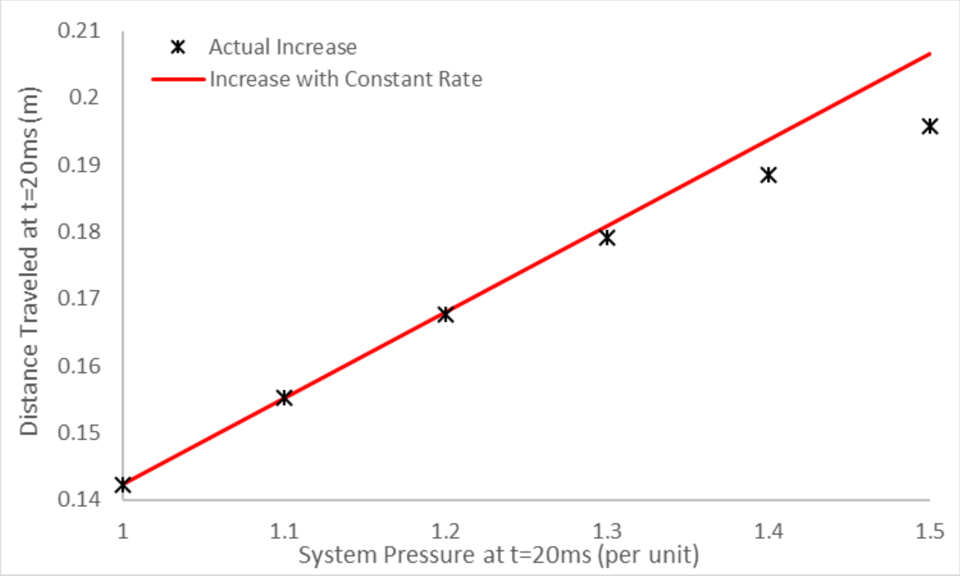

Figure 3.16 Diagram comparing the actual effect of system pressure increase with an imaginary constant rate of increase in distance travelled. Comparison made at t=20.0 ms.

As shown in Figure 3.17, an increase in system pressure leads to a higher maximum pressure during the cushioning process and vice versa. In the case of a 20% increase, the maximum pressure reached 130.65 MPa. This is a factor to be considered, although increasing the system pressure can effectively reduce the total operation time, excessive pressure-rise in the cushioning process could potentially compromise system safety. Therefore, an optimum value for system pressure should be selected with the acceptable limit.

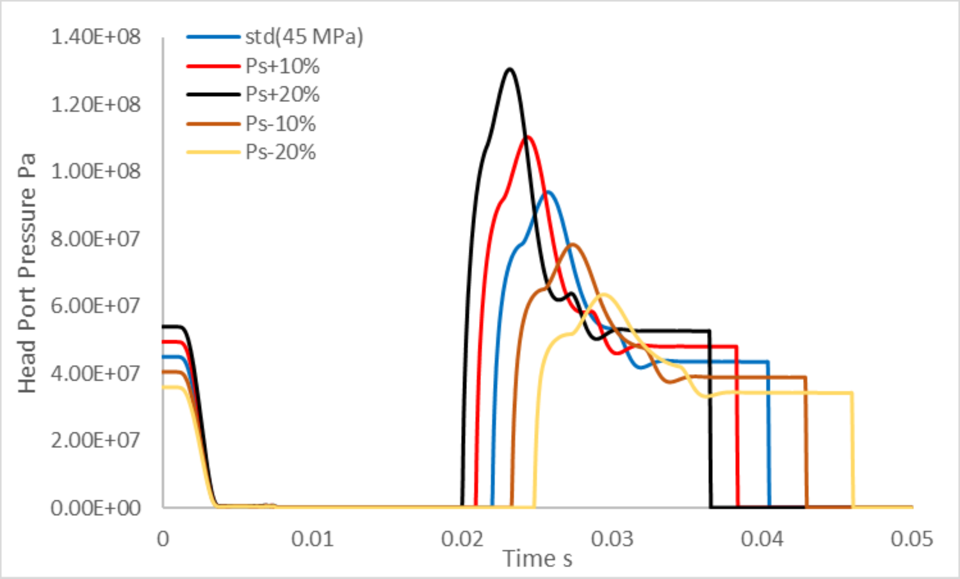

Figure 3.17 Pressure profiles obtained with different system pressures: 45.0, 49.5, 54.0, 40.5 and 36.0 MPa.

The highest top speed in this case reached is 13.78 m/s, when the system pressure is increased by 20%, as shown in Figure 3.18, while the lowest top speed is 10.22 m/s, corresponds to the 20% decrease case.

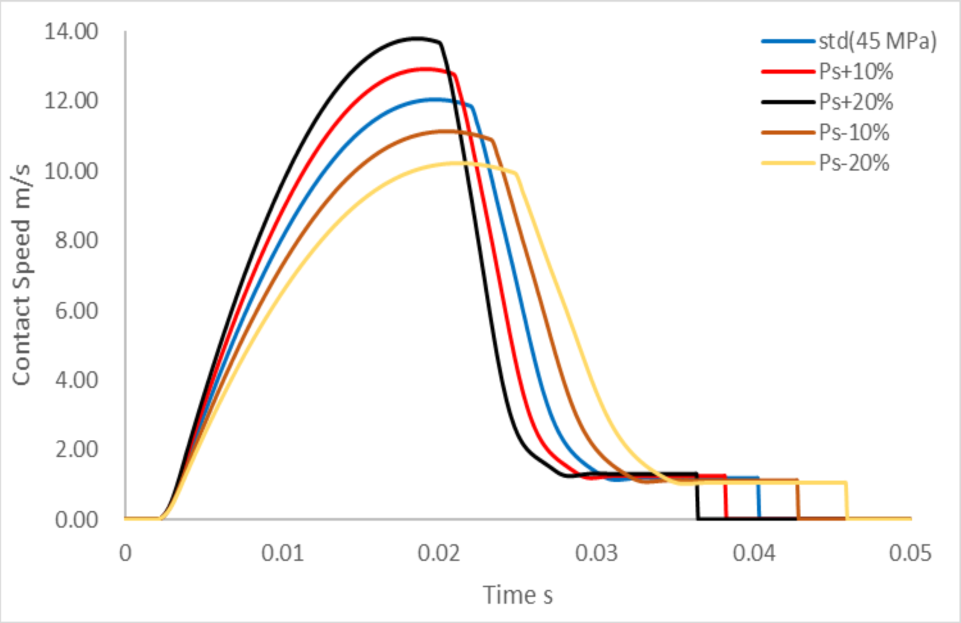

Figure 3.18 Piston speed obtained with different system pressures: 45.0, 49.5, 54.0, 40.5 and 36.0 MPa.

3.3.3 Piston rod side area

Another important parameter to consider is the piston rod side area. This is the surface area of the piston that is directly under constant high pressure during an opening operation. As a structural parameter, an attempt to change the piston rod side area will often result in the change of other parameters such as the head side area (A_{c3}) or parameters related to the cushion structure. Nevertheless, it is worthwhile examining the effect of a changing piston rod side area, since this is one of the most direct and effective way to manipulate the dynamic characteristics of the driving mechanism. Travel curves obtained with different piston rod side areas are presented in Figure 3.19.

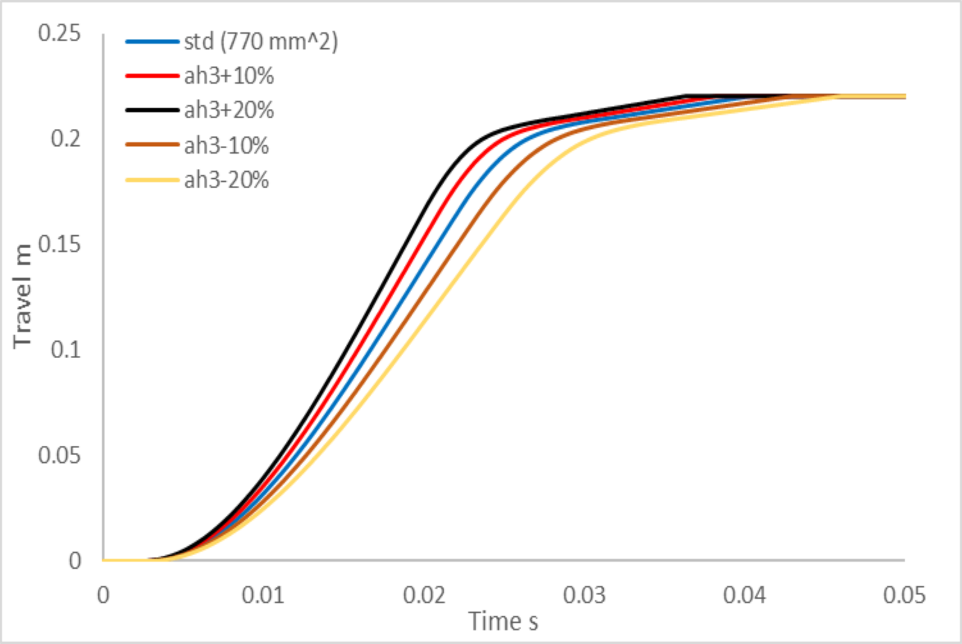

Figure 3.19 Travel curves obtained with different piston rod side areas: 770.0, 784.0, 924.0, 693.0 and 616.0 mm^2.

With a 20% increase in piston rod sided area, the total operation time is reduced to 34.6 ms, although the operation time is slightly longer than 20% increase in system pressure case, the trip in this case is 36.4 ms, 0.1 ms shorter than the 20% system pressure case. The effect is equally significant on the opposite side, by reducing the area 20%, the operation time of the driving mechanism reaches 43.6 ms. Together with the information presented in Figure 3.15 and Figure 3.19, it is observed that increasing the piston rod side area has a very similar effect as increasing the system pressure. This can be easily concluded by examining Equation (3.29). Since the rod side of the piston is always under high pressure which is assumed to be the system pressure, the pressure force that drives the piston is in fact the product of piston area and system pressure, i.e.:

$$F_P = P_{h3}A_{h3} = P_sA_{h3} \tag{3.30}$$

Therefore, a change either one of these parameters will have very similar general (in terms of the dynamic characteristics of the piston travel) effects (as can be seen in Figure 3.20 and Figure 3.21).

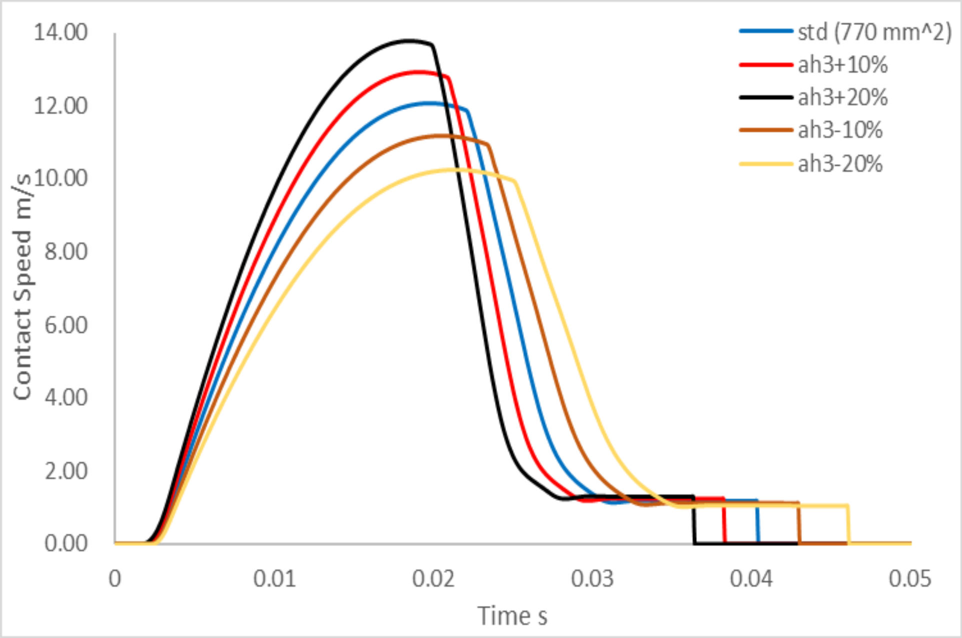

Figure 3.20 Piston speed obtained with different piston rod side areas: 770.0, 784.0, 924.0, 693.0 and 616.0 mm^2.

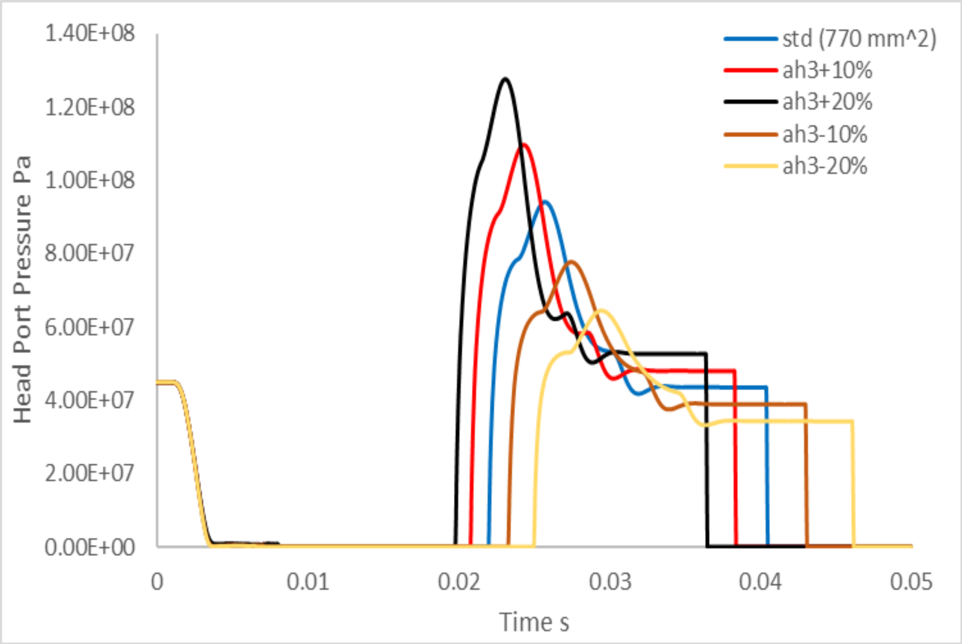

Figure 3.21 Pressure profiles obtained with different piston rod side areas: 770.0, 784.0, 924.0, 693.0 and 616.0 mm^2.

3.3.4 Main valve parameters

Components such as the main valve will also have an impact on the operation time of the system. Enlarging the maximum main valve orifice could potentially lead to a faster discharge process in the cylinder head port and subsequently reduce the total operation time. This is verified by the cylinder head port pressure change shown in Figure 3.22. However, the pressure discharge process in the cylinder has a very short duration and is not sensitive to the change in main valve orifice area

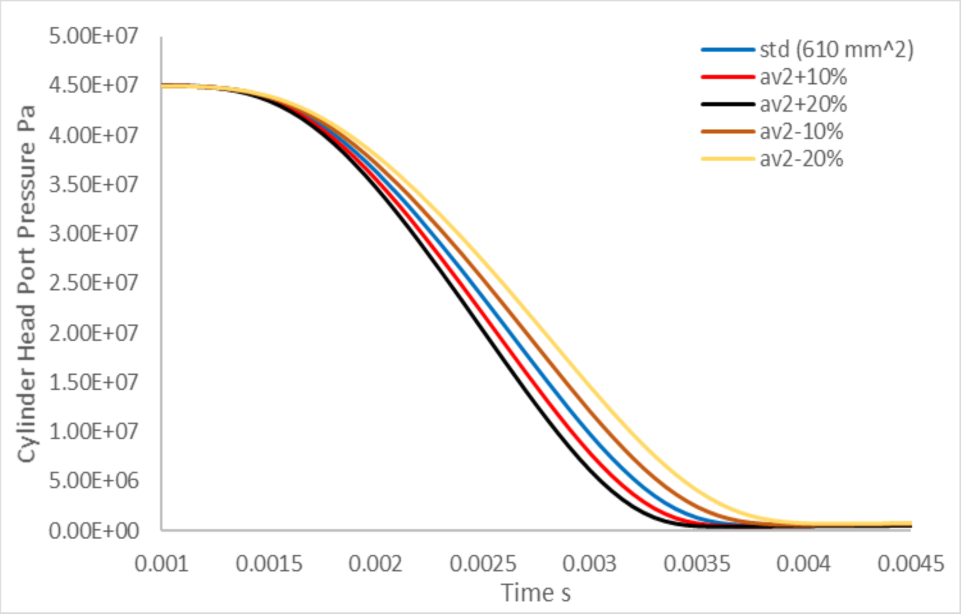

Figure 3.22 Pressure drop in cylinder head port with different maximum main valve orifice areas: 610.0, 671.0, 732.0, 549.0 and 488.0 mm^2.

Consequently, simulation results show that maintaining the same increment, enlarging the main valve orifice area by 20%, the resulting change in operation time is miniscule. Figure 3.23 shows the travel curves with different main valve orifice areas enlarged at the beginning (a) and near the end of the travel (b). As can be seen, increase in the main valve orifice area does lead to a shorter operation time but the effect is insignificant. A 20% increase in maximum orifice area only resulted in a 0.6 ms difference in operation time. A similar conclusion can be drawn for the main valve maximum displacement. In theory, shortening the maximum displacement of main valve spool can have a similar effect to enlarge the orifice area, this measure also leads to a faster discharge process in the cylinder, but as demonstrated in Figure 3.24, the result is also quite limited.

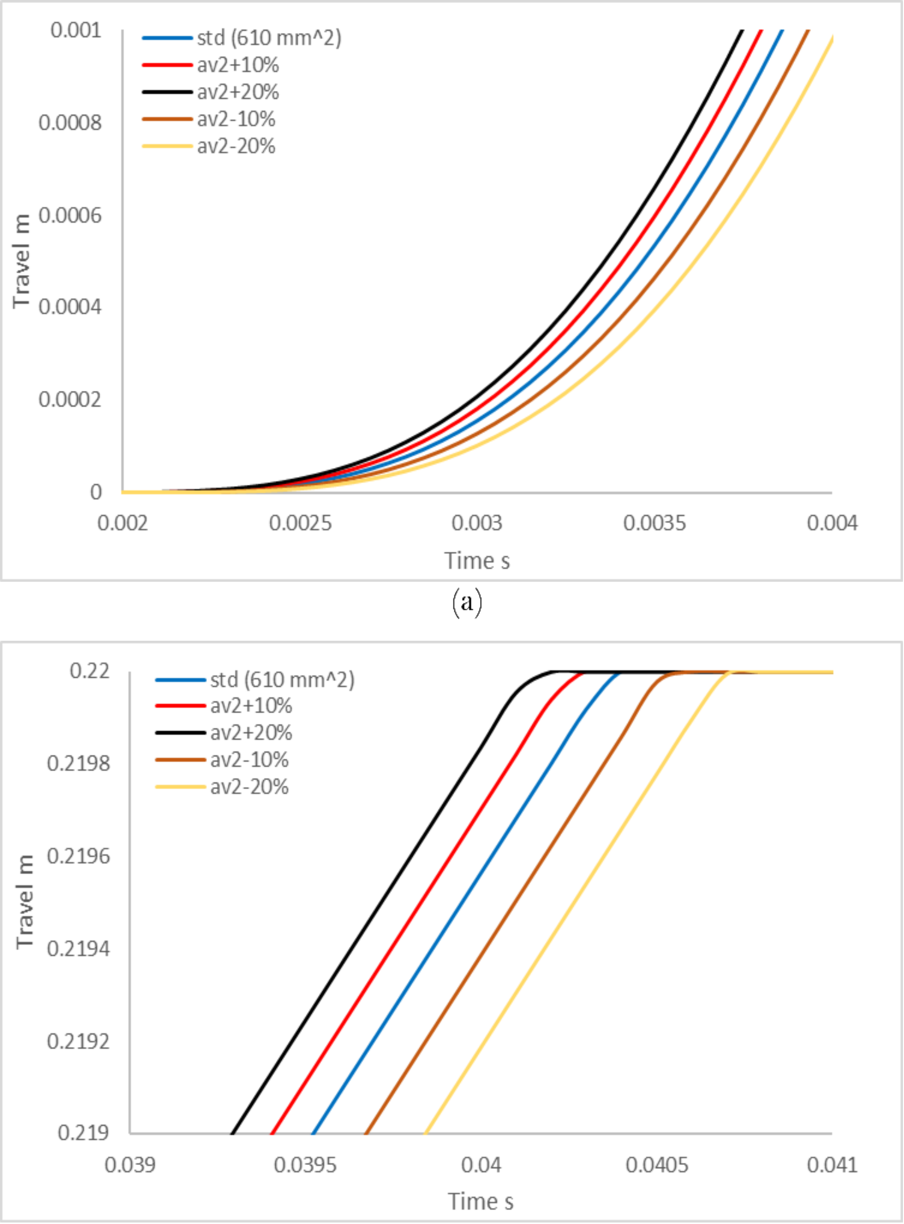

(a)

(b)

Figure 3.23 Travel curves obtained with different maximum main valve orifice areas: 610.0, 671.0, 732.0, 549.0 and 488.0 mm^2, enlarged at the beginning (a) and near the end of the travel (b).

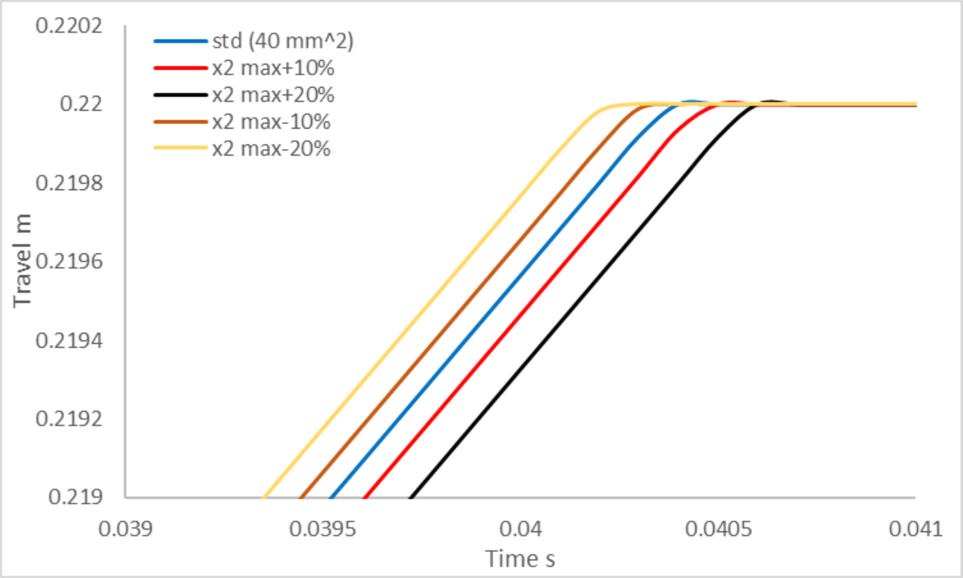

Figure 3.24 Travel curves obtained with different maximum displacements of main valve spool: 40.0, 44.0, 48.0, 36.0 and 32.0 mm, enlarged near the end of the travel.

From the above analysis, it can be concluded that load mass, system pressure and piston rod side area are all important parameters that could potentially be altered in order to attain a desired travel profile. Although not as effective as the changing other parameters, reducing the load mass has the additional benefit that the pressure rise during the cushioning process is also lower and smoother. On the other hand, parameters related to the main valve barely impact the final travel of the piston.

3.4 Conclusion

The basic operating principle of the ZF-11-252 (L)/CYTA hydraulic driving mechanism was explained in this chapter. Based on the understanding of these fundamental processes, a model for the ZF-11-252 (L)/CYTA hydraulic driving mechanism was also established. Equations governing the operation of each individual hydraulic components were explained in detail.

A number of sensitivity studies have been conducted in order to determine the important design parameters of the hydraulic driving mechanism. It was found that:

a) The system is most sensitive to changes in system pressure and piston rod side area. A change in the load mass can also affect the dynamic characteristics of the system considerably (although not to the same extent as system pressure and piston rod side area). On the contrary, the system does not respond to any change in the main valve parameters (orifice area and maximum spool displacement) in any significant way.

b) Increasing the system pressure and piston rod side area can substantially reduce the operation time of the driving mechanism and vice versa. For example, with a 20 % increase in system pressure, a massive 10 ms reduction in the total travel time (the standard total travel time is 45 ms) can be observed. In accordance with this observation is the fact that with a 20% increase in system pressure, the maximum piston speed is increased to 13.5 m/s (with the standard maximum piston speed being 10 m/s). A very similar effect can be observed when increasing piston rod side area by the same proportion. In the meantime, having a heavier load leads a longer operation time and a slower overall piston speed.

c) The effect of changes in both system pressure and piston rod side area are not proportional to the change itself. This should be noted when attempting to optimize the performance of the system.

Chapter 4 Coupled Circuit Breaker Simulation Verification

4.1 Verification of the Arc Model

In order to verify the arc model introduced in Chapter 2, we need to demonstrate the model is capable of:

a) predicting the pressure rise in the interrupting chamber caused by the motion of moving components with reasonable accuracy;

b) predicting the pressure distribution in the interrupting chamber under high current conditions with reasonable accuracy;

c) predicting the characteristics of the arc in terms of arc voltage.

A typical 252 kV puffer circuit breaker has been chosen as an example, based on which two sets of reference simulation have been conducted under different current levels. The calculation results are then compared with available measurement date in order to verify the arc model. 10 and 50 kA fault currents have been selected due to the fact that at 10 kA, the current is relatively low and the arc duration is also short. Thus, the arc has a minimal impact on the pressure distribution in the interruption chamber. As a result, this is an ideal condition to verify pressure predictions caused by compression. For verifying the arc model, arc voltage measurement is also extremely important since it directly reflects how satisfactorily the arc column is modelled. However, arc voltage measurement is less reliable at low current conditions due to the unstable nature of arc. Consequently, another verification test with a higher fault current is needed. At 50 kA, the arc is more stable compared to the low current case. It can be shown that the arc voltage is very sensitive to the size of the arc column for a given current. A small segment of confined arc column can take up a considerable proportion of the overall arc voltage [95]. Therefore, agreement in arc voltage is a key indicator of reasonable prediction of arc size and total energy dumped into the contact space. A reasonably predicted arc column size will lead to a correct prediction of flow cross-sectional area, especially in the main nozzles where the flow is most confined. Therefore, arc voltage comparison under high current conditions can prove convincingly that the arc model is capable of predicting the (electrical and aerodynamical) characteristics of the arc.

The structure of the interrupting chamber used in the verification tests is shown in Figure 4.1. Both the moving and stationary contacts in this case are known as “hollow” contacts as in there are no solid material filling the interior of the contacts and gas are allowed to through. The interrupting chamber can be considered as rotationally symmetric; thus a 2-D axial symmetric domain can be used. Important components in the interrupting chamber are also highlighted in Figure 4.1. The initial filling pressure in the chamber is 0.7 MPa for both cases. Measured contact travel curves are (see Figure 4.4 and Figure 4.9 for 10 and 50 kA cases respectively) used to simulate the movement of the components because this is the most accurate way to assess the arc model only.

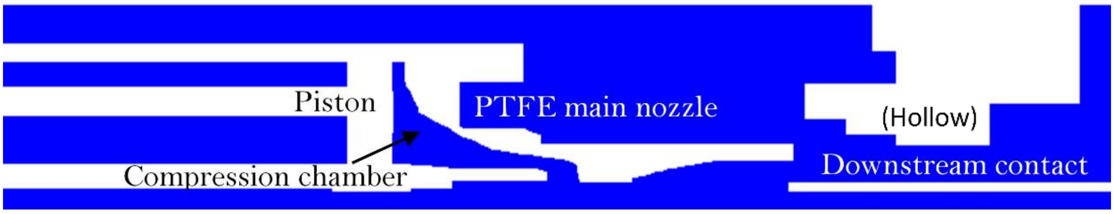

Figure 4.1 Structure of the interrupting chamber of a Puffer 252 kV SF6 circuit breaker.

The 50 kA case can be divided into four different phases, namely: cold flow, high current, current zero and post arc phases. The purpose of the cold flow phase is to allow the flow field to be initialized before arcing. In addition, there is a 40 mm overlap between the contacts. Within the cold flow phase, the contacts are allowed to separate, when a 5-8 mm gap between contacts is established, the cold flow phase ends and the high current phase begins. In the high current phase, the arc is introduced by initiating a hot column with the temperature gradually decreases from the axis toward the radial direction. The radius of the hot column in this case is 5 mm with an axis temperature of 28000 K. If the current at the initial instant is very high, for computational considerations, a special code is used to ramp the current from 3 kA to its true instantaneous value within 0.2ms. An instantaneous current of 15 kA before the final current zero demarks the high current and current zero phase. The reason for choosing this particular value as the boundary between high current and current zero phase is explained in [76]. The current zero period deals with rapidly decreasing arc current and the arc column can become very thin. The post arc simulation starts from the end of the current zero simulation and runs up to the point where the downstream contact has reached maximum travel, 220 mm in this case. The instantaneous current in the 10 kA case never exceeds 15 kA, as a result, the 10 kA case does not include a high current phase.

During the verification tests, four strategically located monitor points (see Figure 4.2) are used to record the pressure variation in the arc chamber. Monitor point 1 is well inside the compression chamber where it is far away from the arc region. Point 2 is located near the exit of the compression chamber, which is close to the arc. Collectively, pressure recorded at monitor point 1 and 2 provide a general description as how pressure is building up at the upstream of the nozzle (see Figure 4.2). By comparing results recorded by point 1 and 2, some insight on how the arc affects pressure distribution in the arc chamber can be gained. Point 3 is positioned at the flat nozzle throat while point 4 is near the downstream region of the nozzle.

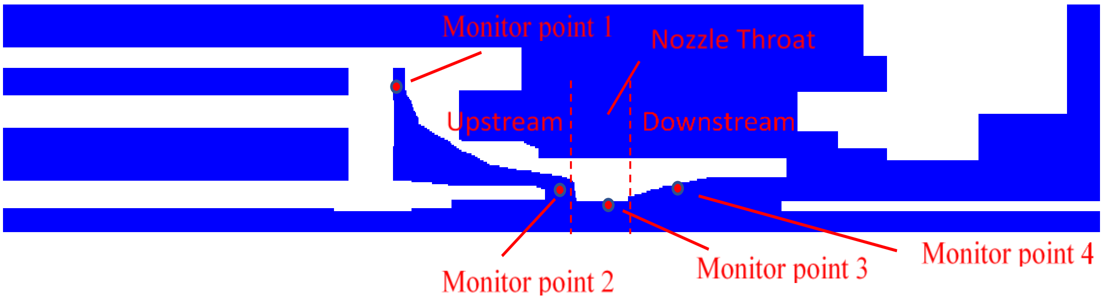

Figure 4.2 Locations of pressure monitor points during the arc model verification tests.

The pressure measurements were conducted at Pinggao Electrical Co. Ltd [96]. The ZF-11-252 (L)/CYTA type hydraulic driving mechanism is coupled with the same 252-kV puffer type chamber, based on this experiment platform, fibre optic and piezoresistive (Endevco model 8530B-500) pressure sensors were used to measure the arc chamber pressure under both 10 and 50 kA current conditions. Figure 4.3 shows the overall arrangement of sensors during pressure measurements.

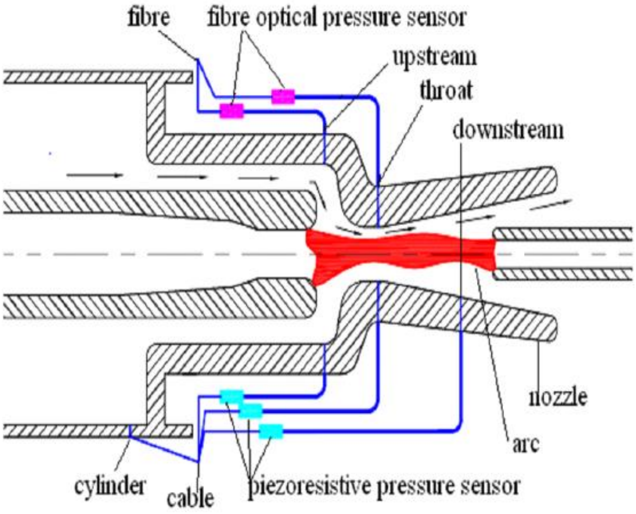

Figure 4.3 The installation of fibre optic and piezoresistive pressure sensors during pressure measurements conducted by Pinggao Electrical Co. Ltd [96].

The Endevco pressure sensor has a maximum range up to 34.5 bar and a sensitivity of 10.4 mV/bar. With 750 kHz dynamic response, the piezo sensor is capable of capturing the pressure transients during arcing, the fibre optic sensors were used as references in order to assess the measurement system. Contact travel and arc voltage were also measured under the same current conditions.

4.1.1 10 kA case

The measured current, contact travel as well as arc voltage for the 10 kA case are presented in Figure 4.4 The red dot marks the contact separation point (at 47 mm travel), it is at this instant that the arc is initiated in the measurement. The total arcing duration is 7 ms in this case, the peak instantaneous current in the last loop is 2.5 kA and the maximum measured arc voltage reaches above 1 kV.

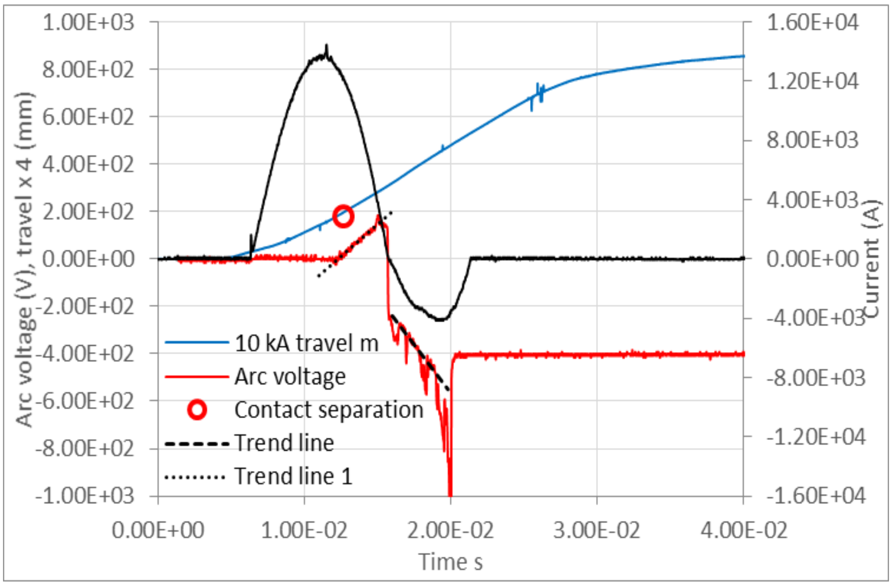

Figure 4.4 Contact travel, current and arc voltage measurement for the 10kA case.

In the verification tests, both the measured current and travel are smoothened and then provided to the simulation in the form of data sheets, interpolation is used between data points. The simulation current together with the predicted arc voltage is compared with the measurement data, the comparison is shown in Figure 4.5. Data from the simulation is matched to the measured data (10 kA case only) by shifting the time base using:

$$t_1 = t_2 - 0.0127$$

where t_1 is time base for measurement and t_2 is the time base for simulation.

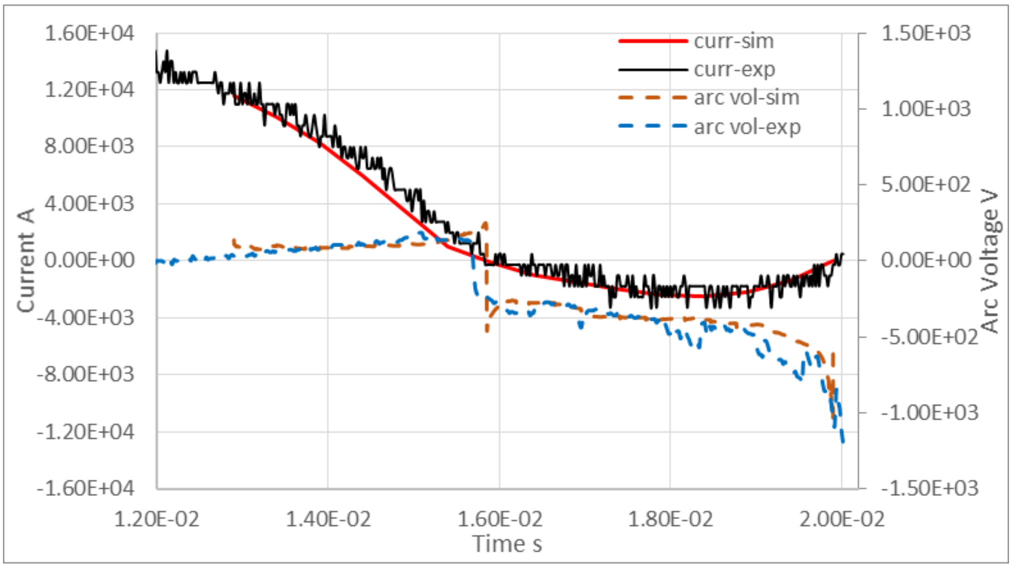

Figure 4.5 Comparison between predicted and measured current and arc voltage.

It can be observed that shortly after contact separation, the both predicted and measured arc voltage increases smoothly. Once the current crosses the zero point, the measured arc voltage is no longer smooth and exhibiting strong fluctuations. However, fluctuations captured by the measurement is not reflected in the calculation. The fluctuation in the measured arc voltage is possibly associated with arc instability at low current. Since arc voltage is closely related to the total energy input from the arc, as an indicator of arc column size and shape, the predicted temperature field is at different instances during the simulation in Figure 4.6 to present a history of the arcing process.

Temperature contours given in Figure 4.6 indicates that when current is relatively low, the arc tends to be thin and long rendering it more susceptible to turbulence cooling. Therefore, in general, it is difficult to measure arc voltage accurately under low current conditions. It has been demonstrated that arc voltage is extremely sensitive to the size of arc column [97] which can vary quite substantially as illustrated in Figure 4.6. In terms of reaction force calculation, the overall pressure distribution in the arc chamber is of greater concern, especially at low current levels where the influence of the arc on pressure variation is limited. Therefore, compared with arc voltage, the predicted pressure in the arc chamber at different locations is of more interest. The comparison between predicted and measured pressure at the aforementioned monitor points are presented in Figure 4.7.

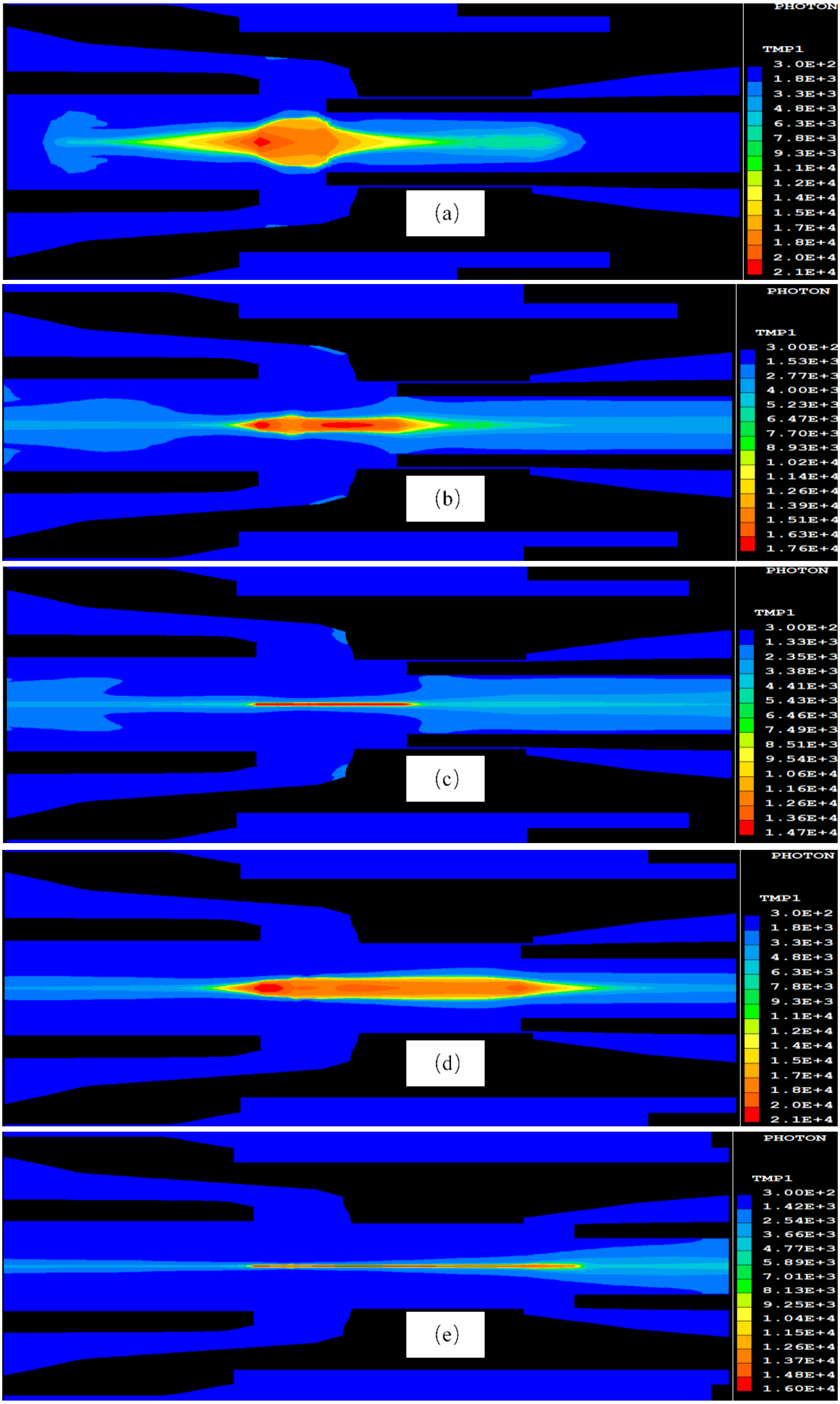
PHOTON
TMP1
3.0E+2
1.8E+3
3.3E+3
4.8E+3
6.3E+3
7.8E+3
9.3E+3
1.1E+4
1.2E+4
1.4E+4
1.5E+4
1.7E+4
1.8E+4
2.0E+4
2.1E+4
(a)
PHOTON
TMP1
3.00E+2
1.53E+3
2.77E+3
4.00E+3
5.23E+3
6.47E+3
7.70E+3
8.93E+3
1.02E+4
1.14E+4
1.26E+4
1.39E+4
1.51E+4
1.63E+4
1.76E+4
(b)
PHOTON
TMP1
3.00E+2
1.33E+3
2.35E+3
3.38E+3
4.41E+3
5.43E+3
6.46E+3
7.49E+3
8.51E+3
9.54E+3
1.06E+4
1.16E+4
1.26E+4
1.36E+4
1.47E+4
(c)
PHOTON
TMP1
3.0E+2
1.8E+3
3.3E+3
4.8E+3
6.3E+3
7.8E+3
9.3E+3
1.1E+4
1.2E+4
1.4E+4
1.5E+4
1.7E+4
1.8E+4
2.0E+4
2.1E+4
(d)
PHOTON
TMP1
3.00E+2
1.42E+3
2.54E+3
3.66E+3
4.77E+3
5.89E+3
7.01E+3
8.13E+3
9.25E+3
1.04E+4
1.15E+4
1.26E+4
1.37E+4
1.48E+4
1.60E+4
(e)

Figure 4.6 The shape of arc column at different instants in the arcing process of the 10 kA case. The simulation time, instantaneous current and maximum temperature in the arc are: (a) 26.59 ms, 8337.6 A, 21000 K (b) 28.19 ms, 797.8 A, 17600 K (c) 28.59 ms, -82.4 A.

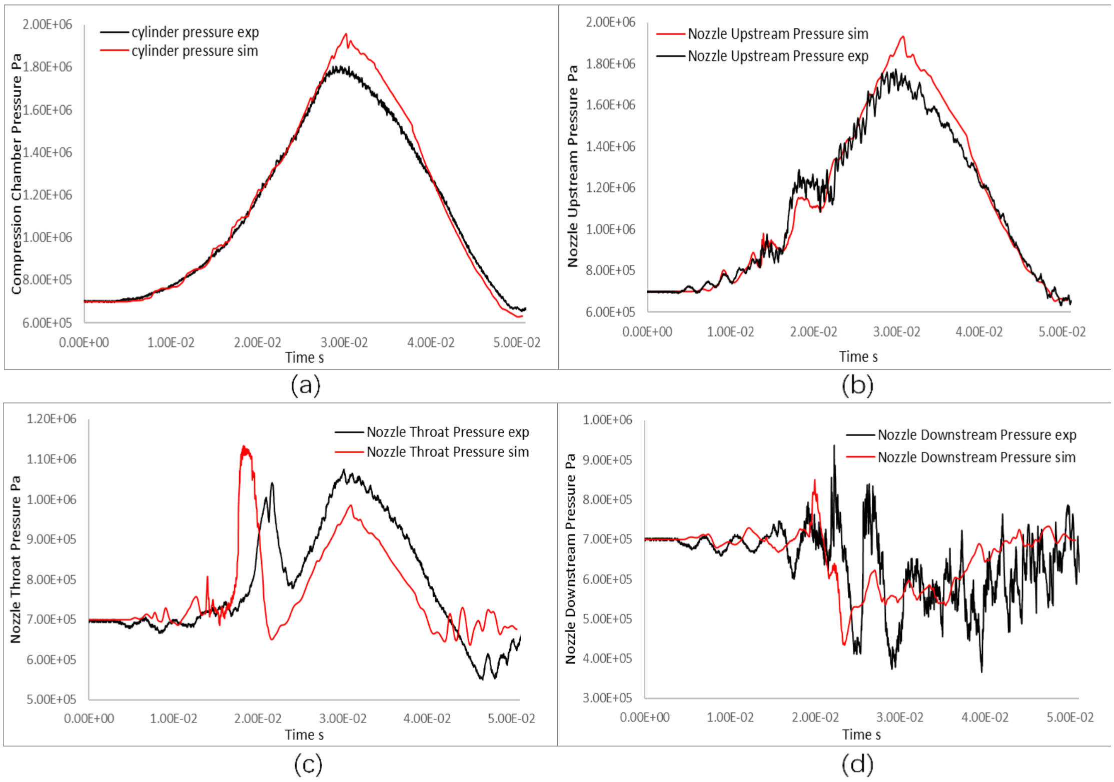

Figure 4.7 Comparison between predicted and measured arc chamber pressure for 10 kA cases: (a) monitor point 1, (b) monitor point 2, (c) monitor point 3, (d) monitor point 4.

Data recorded at monitor point 1 and 2 give a good description of the compression process in the compression chamber. Due to its close proximity to the arc, pressure recorded at point 2 exhibits a mild fluctuation which is absent at point 1. The maximum pressure reached at both points seems to exceed that of the measurement by 0.2 MPa, 18% of the absolute pressure rise. Considering the experimental uncertainties, the agreement is rather reasonable. In addition, the maximum pressure in the simulation is reached at t=31 ms, 2 ms behind the measurement. These discrepancies cannot be attributed to the arc since the difference is observed at both point 1 and 2. The difference is likely caused by the smoothened travel used in the simulation. The sudden surge of local pressure both measured and predicted at point 3 (around t=20 ms) is caused by the downstream contact blocking the nozzle, forming a high-pressure region. Once the contact clears the flat nozzle throat, the stagnant gas is quickly discharged and the local pressure drops. Notice the pressure rise in simulation occurs earlier than in the measurement. This can also be explained by the difference between the smoothened and measured travel.

Figure 4.8 compares the travel originally measured for the 10 kA case against the smoothened one at around t=20 ms (Figure 4.8 (a)) and t=31 ms (Figure 4.8 (b)). It can be observed that around t=20 ms, the smoothened travel pulls slightly ahead of the measured travel, as a result, the contact clears the nozzle throat sooner in the simulation than in the measurement, causing the pressure surge captured at point 3 to appear sooner than in reality. On the other hand, at around t=31 ms, the smoothened contact lags behind the measured travel, delaying the occurrence of maximum pressure in the simulation. Nevertheless, the effect of the smoothened travel is rather limited, since at both nozzle throat and compression chamber, the difference in measured and predicted pressure is small (no more than 0.2 MPa). Although the difference between measured and predicted pressure at point 4 is clearly visible, overall, they contribute very little towards the total reaction force since the absolute pressure change in this region never exceeds 0.3 MPa. Based on the above discussion, it can be concluded that in this case the arc model can predict the pressure variation in the arc chamber to a satisfactory degree.

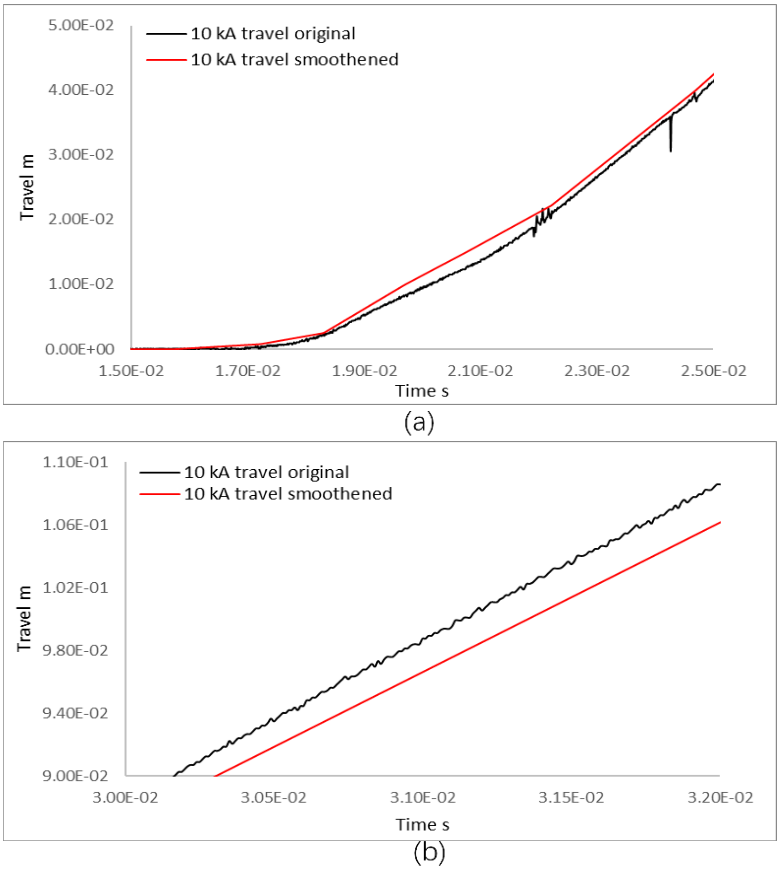

(a)

(b)

Figure 4.8 The smoothened and measured travel curve at t=20 (a) and t=31 (b) ms.

4.1.2 50 kA case

The measured current, contact travel as well as arc voltage for the 50 kA case are shown in Figure 4.9, the contact separation point is also marked in the diagram. The total arcing duration is 19 ms in this case, which is considerably longer than the 10 kA case. The peak instantaneous current in the last loop is 47 kA, also significantly higher than the 10 kA case. The maximum measured arc voltage in this case reaches above 1.5 kV. The predicted arc voltage for the 50 kA case is compared with measurement data in Figure 4.10.

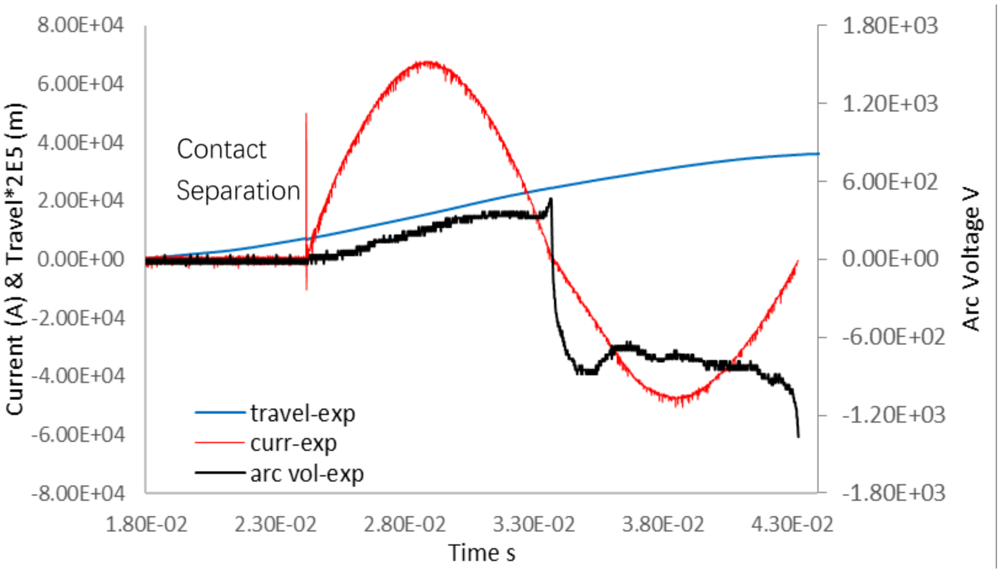

Figure 4.9 Measured current, contact travel and arc voltage for the 50 kA case.

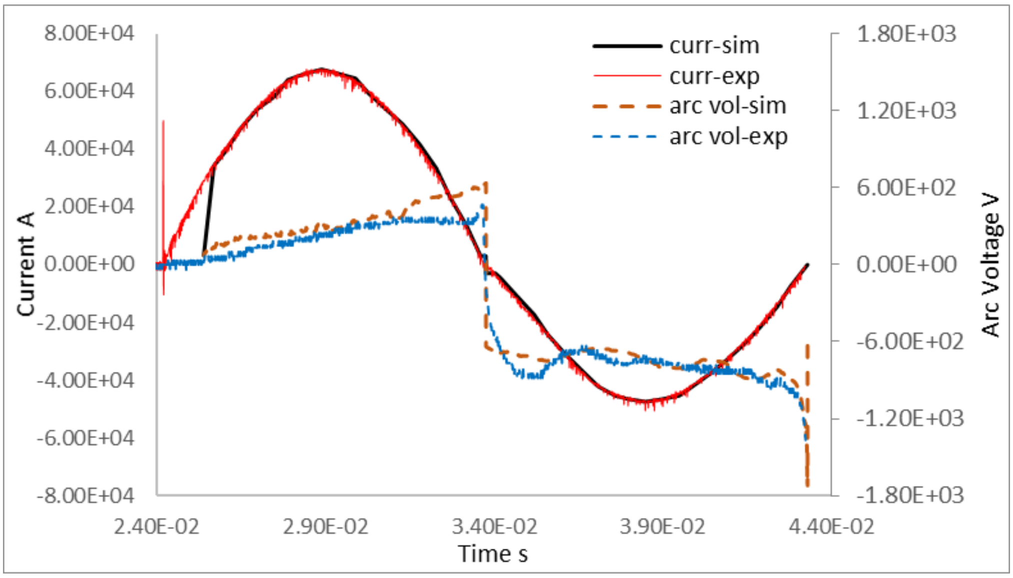

Figure 4.10 Predicted arc voltage and simulation current compared to measurement data for the 50 kA case.

There is a good overall agreement between the prediction and measurement. It can be seen that the arc model overpredicts the arc voltage from t=31 ms to t=34 ms. Using the 5000 K isotherm as the boundary of the arc core, Table4.1 provides the arc radius recorded at different axial locations during this period of time (t=31 ~ t=34 ms).

Table 4.1 1 Arc radius at different axial locations (represented by axial cell numbers) at different instances during the 50 kA high current phase.

Axial location	t=32.65 ms (mm)	t=32.9 ms (mm)	at t=33.15 ms (mm)
z=100	0.0048	0.0040	0.0036
z=110	0.0057	0.0049	0.0044
z=120	0.0063	0.0058	0.0054
z=130	0.0085	0.0080	0.0073
z=140	0.0093	0.0087	0.0076
z=150	0.0097	0.0088	0.0077
z=160	0.0112	0.0100	0.0091
z=170	0.0118	0.0110	0.0100
z=180	0.0180	0.0153	0.0133

Data in Table 4.1 showed that as time progresses, the radius of the arc column is shrinking with the diminishing current. This limits the cross-sectional area of the conducting column, which could potentially lead to the increase of arc voltage. An extinction peak was observed in this case where towards the last current zero the arc voltage increases rapidly. The extinction peak in arc voltage reflects the change of arc resistance with a rapidly decreasing current. Leading up to the thermal interruption process, it is extremely important for the arc model to predict the arc voltage accurately within this period of time. In order to achieve a reasonable arc voltage prediction in the current zero phase, the turbulence parameter is varied according to the instantaneous current, which is linked in general to the relative size of the arc column with respect to the confining nozzle (maybe elaborate?).

Similar to the 10 kA case, temperature fields in the arc chamber are given to provide a description of the arcing history (Figure 4.12). Quickly after being initialized by adding a hot column to the domain, the arc adjusts its temperature field according to the distribution of ohmic heating. When fully established, the arc extends into the hollow contacts under the axial pressure gradient generated by the Lorentz force. At around t=31 ms, the downstream contact clears the nozzle throat, a flow channel is subsequently opened, through which hot gas from within the contact gap is discharged towards downstream. At around t=34 ms, the current crosses its first zero points. At this point, the arc column becomes relatively thin, this is also reflected by the data in

Table4.1. As can be seen, the arc is surrounded by a layer of cold flow at this moment, while the hole of the moving contact is still filled with hot gas. After the first current zero, the arc current increases rapidly and no longer being constrained by the moving hollow contact, radius of the arc column expands drastically towards the downstream region.

Figure 4.11 presents the measured and predicted pressure at four different monitor points (same location as in 10 kA case.) Due to the strong interference of the arc, severe fluctuation in measured pressure can be seen at all locations. Both piezoresistive and optic fibre sensors are used to measure the pressure at nozzle upstream and nozzle throat, which corresponds to monitor point 2 and 3 in the simulation. The arc-induced pressure oscillation has a relatively high frequency ranging from 400 to 800 Hz. Pressure measured by both type of sensors is nearly identical, with very similar oscillation frequency. This indicates that the measured data in the 50 kA reliable and trustworthy.

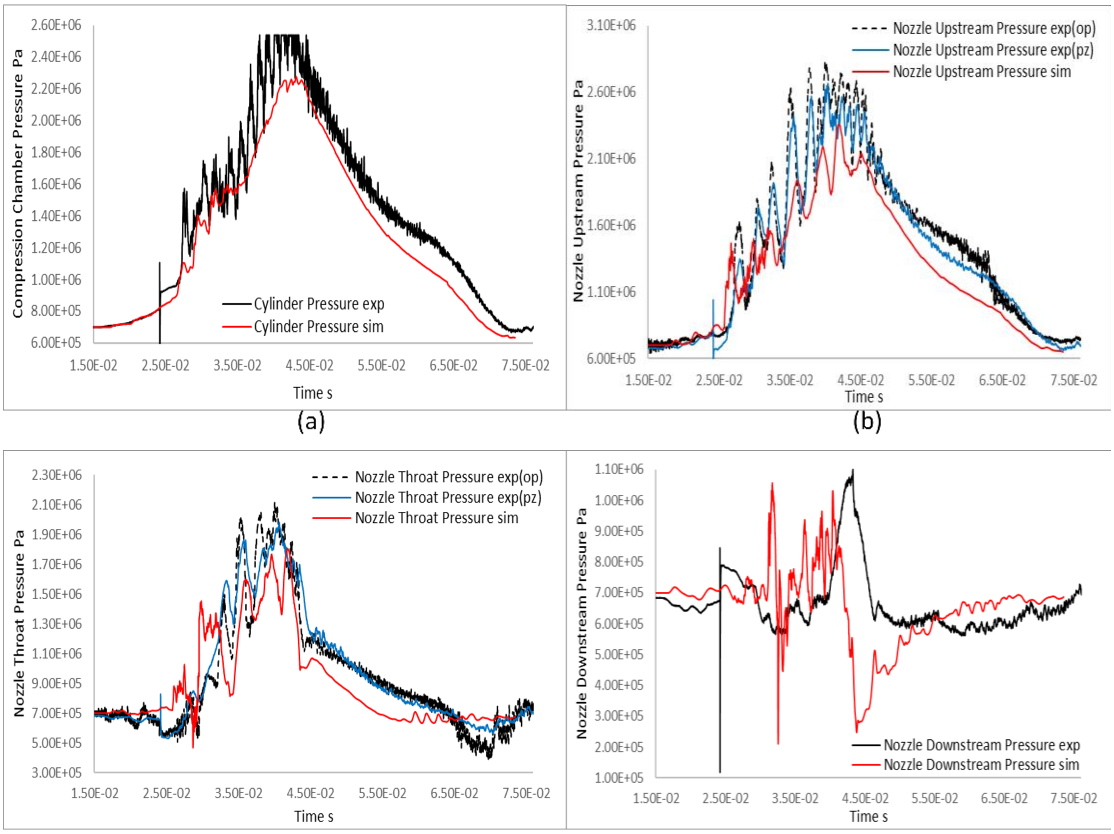

(a) (b)

(c) (d)

Figure 4.11 Comparison between predicted and measured arc chamber pressure for 50 kA cases: (a) monitor point 1, (b) monitor point 2, (c) monitor point 3, (d) monitor point 4.

In the meantime, although the predicted pressure at point 1, 2 and 3 exhibits a similar oscillation frequency, their instantaneous values are consistently lower than the measured pressure. To observe this effect at three different monitor points means the arc model has a tendency to underpredict pressure under high current conditions. This issue will be addressed later in section 4.3.

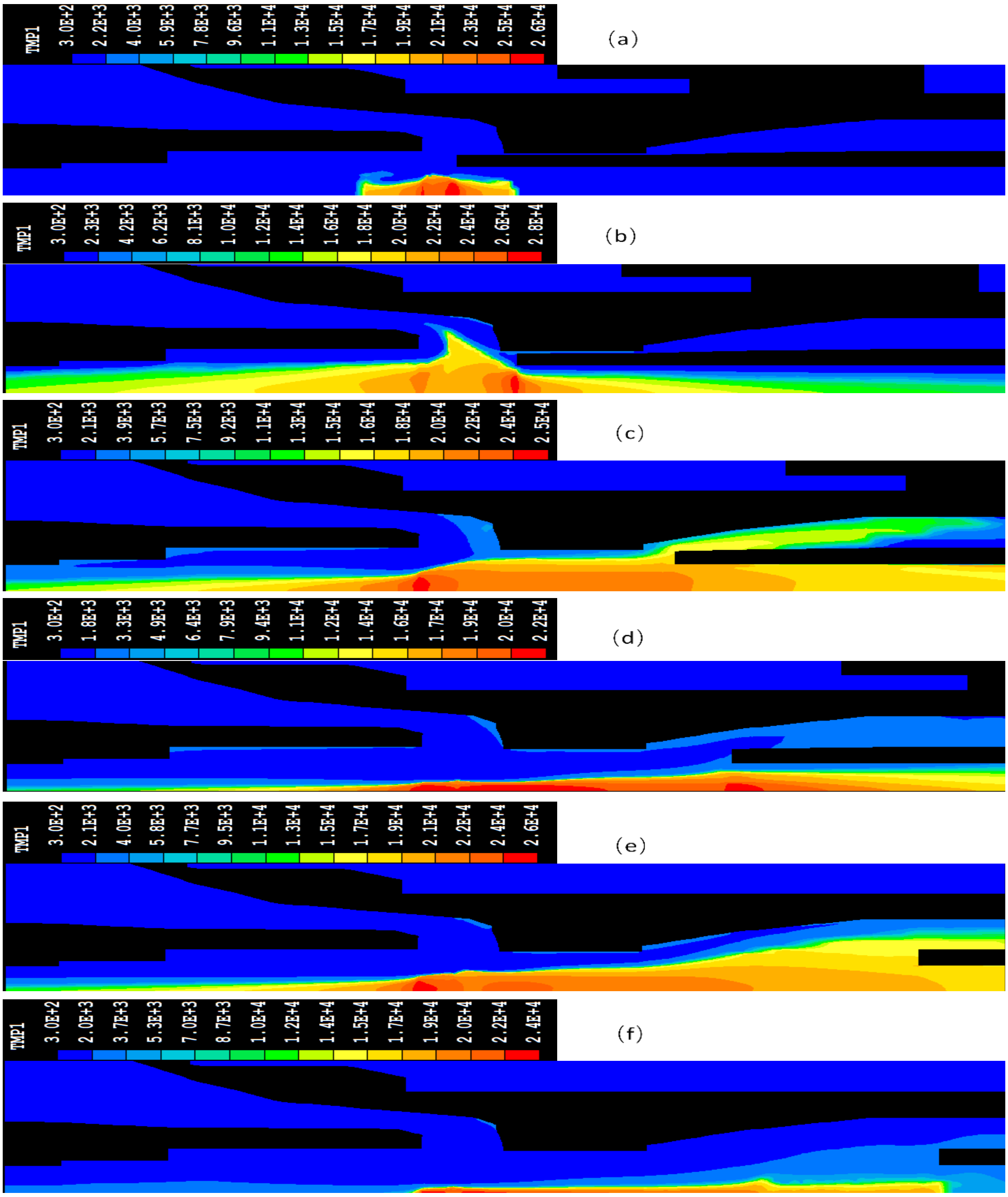

Figure 4.12 The shape of arc column at different instants in the arcing process of the 50 kA case. The simulation time, instantaneous current and maximum temperature in the arc are: (a) 25.80 ms, 23860.8 A, 30000 K (b) 27.65 ms, 57871.1 A, 28000 K (c) 32.15 ms, 39239280.4 A, 25000 K (d) 33.75 ms, 4523.9 A, 22000 K (e) 41.40 ms, -29914.9 A, 26000 K (f) 43.33 ms, -2487.7 A, 23000 K.

4.2 Verification of Reaction Force Calculation

As previously explained, the calculation procedure of reacting force is organized into a subroutine which can be called by the PHOENICS solver during a simulation. To verify this subroutine, a test simulation based on a simple geometry is prepared. In this case, the test case is a replica of the compression chamber typically found in puffer circuit breakers (see Figure 4.13, at this point, the piston is in motion, the pressure wave is visible, propagating from the piston to the stationary wall). The piston is set to move at constant speed to create a compressive effect in the chamber (6 m/s). The initial pressure inside the chamber is set to 0.7 MPa, representing the filling pressure in a full-scale circuit breaker simulation. Since there is no inlet or outlet in the domain, the pressure in the chamber as well as the pressure force recorded on the wall are expected to rise continuously until the piston comes to a stop.

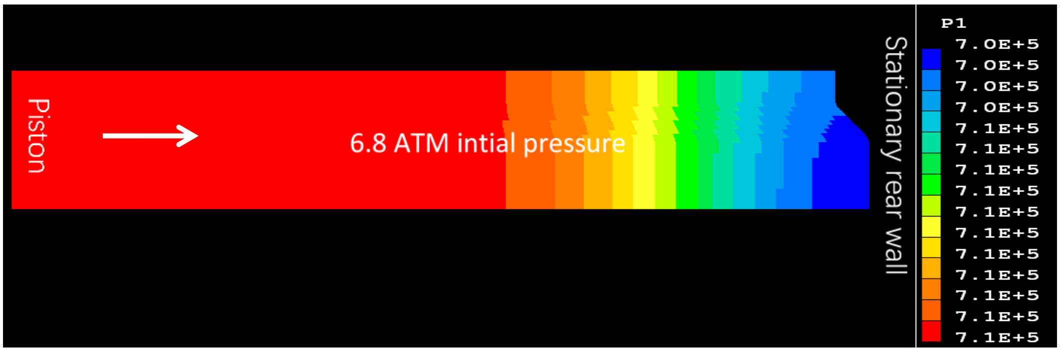

Figure 4.13 Computational and conditions of the reaction force verification case.

Since the area which is subjected to the pressure force is constant and easily calculable, the recorded force on the rear wall can be used to verify the method of reaction force calculation explained in Chapter 2. Figure 4.14 shows the predicted force recorded on the wall surface. The final recorded value of reacting force is a total of 35757.13 N on the surface. With the effective area of the wall known, it is possible to work out a theoretical value of the reacting force based on the pressure recorded on the same wall surface. The theoretical value for the reacting force at the end the simulation is 37693.8 N.

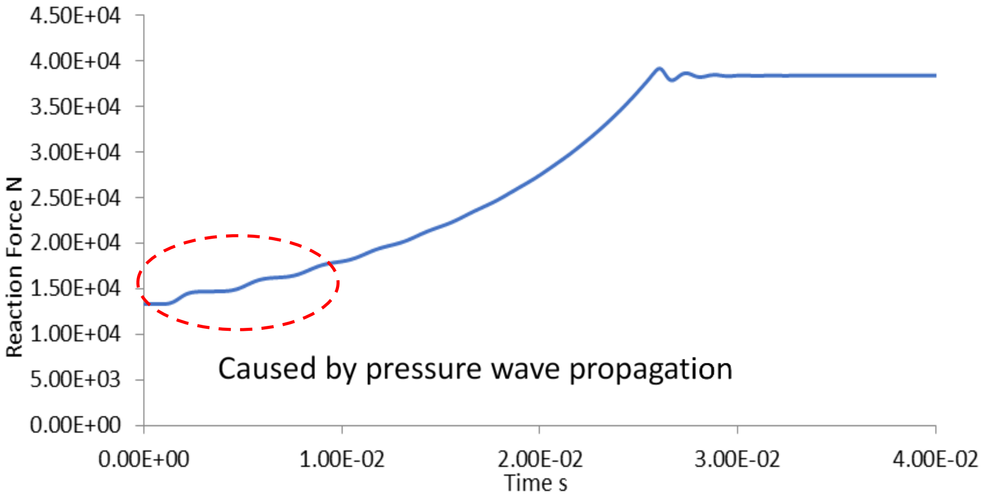

Figure 4.14 Pressure force recorded on the surface of the stationary wall during the test case.

The result provided by the subroutine is reasonable, although minor difference (5%) was found when comparing the calculated and theoretical results. The theoretical value is obtained assuming a uniform pressure distribution on the wall surface, this explains the discrepancy between calculation and theoretical results. Despite this, the simple test proves that the method is capable of estimating the area which should be included in the reaction force calculation satisfactorily.

The pressure distribution in arc chamber has a direct impact on the magnitude of the reacting force. To further verify the reaction force calculation, reaction force obtained in both 10 and 50 kA cases are presented with the pressure prediction (Figure 4.15). The main pressure difference in the arc chamber is located across the main nozzle and is the dominant factor when evaluating the reaction force. In both 10 and 50 kA cases, compared with pressure in the compression chamber (point 1 and 2), the pressure recorded at monitor 4 which represents the nozzle downstream pressure is relatively small and contributes little to the total reaction force. Consequently, the profile reaction force in both cases should closely follow the pressure variation in the compression chamber which can be easily observed in Figure 4.15.

Using the 50 kA case as an example, pressure contours in the arc chamber at different typical instances (marked correspondingly in Figure 4.15) during the arcing process is presented in Figure 4.16. In the cold flow stage (Figure 4.16 (a)), before contact separation, the down-stream contact is blocking the compression chamber exit, as a result, the pressure inside the compression chamber begins to rise while the rest of the arc chamber is still at the uniform filling pressure. During in high current phase (Figure 4.16 (b)), due to the intense heating from the arc, pressure in the arc core exceeds that in the compression chamber. In this stage, pressure in the arc chamber in general, increases rapidly. At the end of the high current phase (Figure 4.16 (c)), both pressure in the arc core and compression chamber reach their peak value. Due to the rapid decrease in current zero stage (Figure 4.16 (d)), the energy input into the arc is diminishing. In the meantime, the arc is subjected to intense turbulence cooling. As a result, pressure in the arc core region falls to a relatively low level (see Figure 4.16 (d) monitor point 2). Finally, after current zero (Figure 4.16 (e) and (f)), pressure in the arc chamber is considerably lower compared with previous stages, which also led to the decrease in reaction force, in the end, the pressure in the arc chamber returns to an almost uniform state, close to the initial filling pressure.

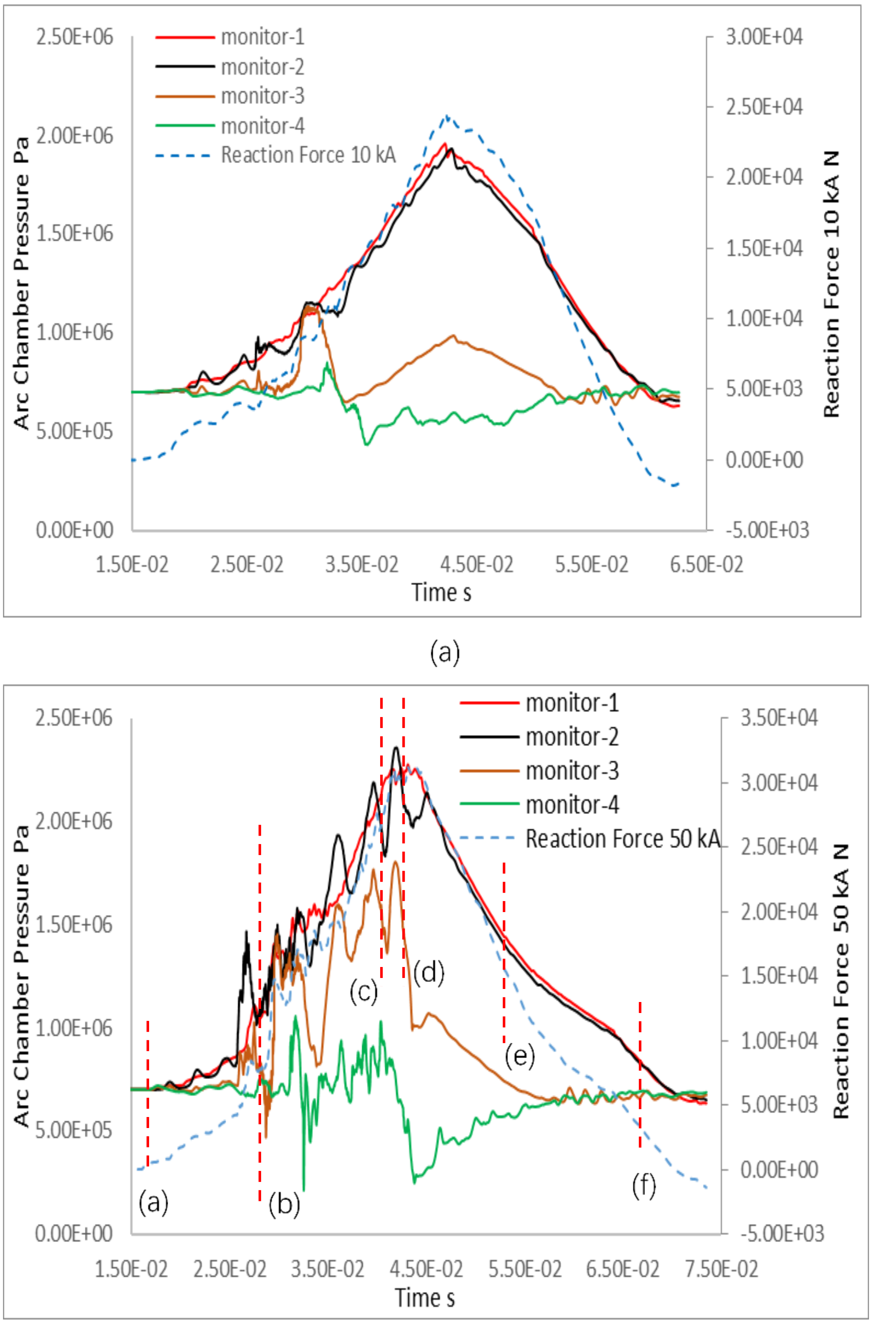

(a)

(b)

Figure 4.15 Reaction force recorded in both 10 (a) and 50 (b) kA cases together with predicted arc chamber pressure at different typical locations.

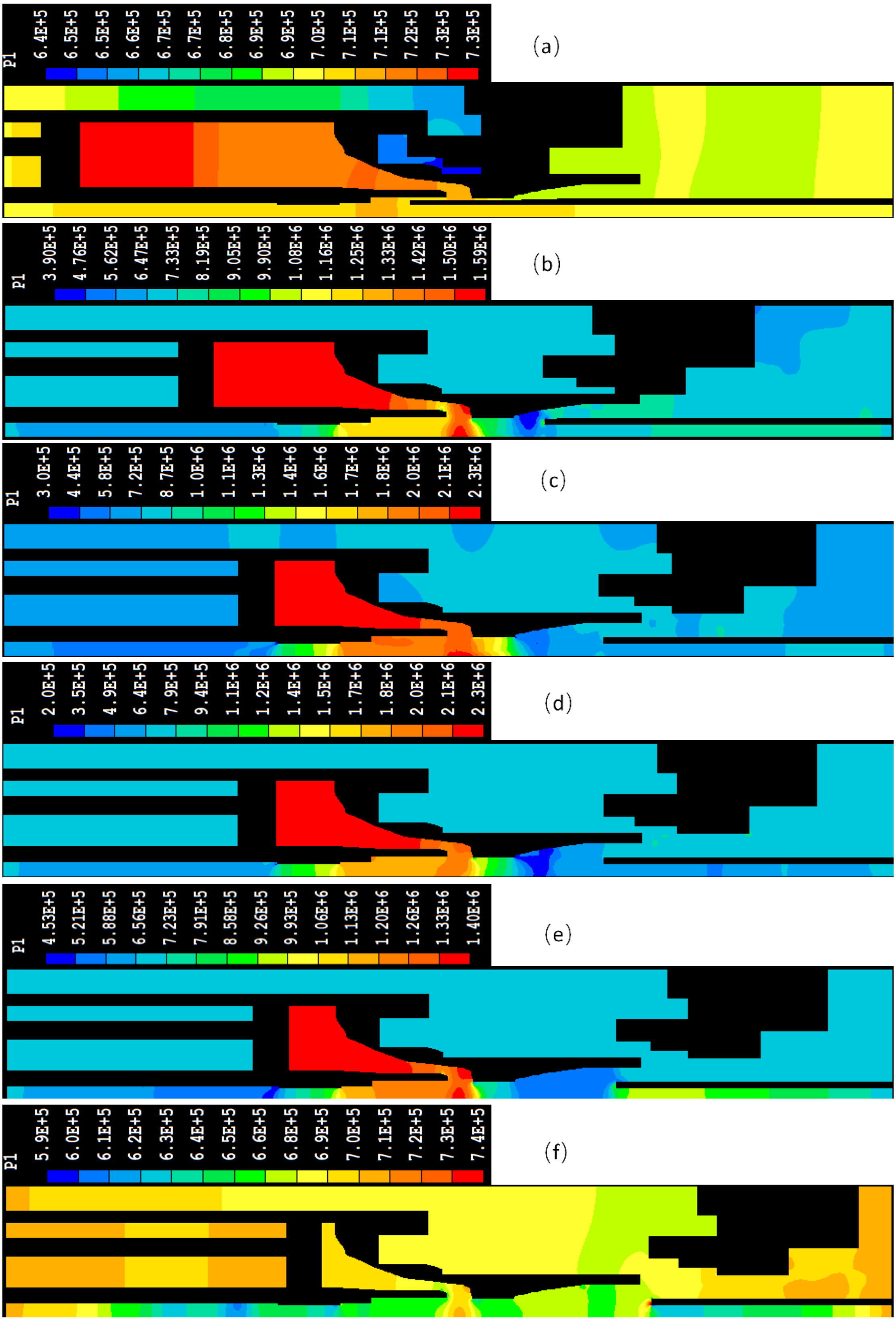

Figure 4.16 Pressure distribution in the arc chamber (50 kA case), the time, maximum pressure in the arc chamber are: (a) 19.5 ms, 0.74 MPa (b) 34.2 ms, 1.59 MPa (c) 43.0 ms, 2.30 MPa (d) 43.5 ms, 2.63 MPa (e) 53.7 ms, 1.41 MPa (f) 70.0 ms 0.74 MPa.

Moments presented in Figure 4.16 describes the pressure change throughout the arcing history, which coincides with the change of recorded total reaction force. On the basis that the arc model is able to predict the pressure variation in the arc chamber under different current levels to a reasonable degree, the reaction force obtained in these verification tests are considered reliable. The calculation method introduced in Chapter 2 can be used in coupled simulation provided the pressure prediction is accurate.

4.3 Verification and Calibration of the Driving Mechanism Model

Based on the model introduced in chapter 2 and 3, coupled simulation for both 10 and 50 kA have been conducted. The initial result differs by a considerable amount from the measured travel curves for both 10 and 50 kA. After comparing the predicted (based on the hydraulic driving mechanism model presented in Chapter 3) and measured travel, it has been determined that calibrations based on measured data are necessary in order to improve coupled simulation results. This section will address the source of the inaccuracy and also offer a method to improve the accuracy of hydraulic driving mechanism model.

4.3.1 The effect of reaction force

As a closed system without considering the interaction with the arc chamber, the driving mechanism model grossly overpredicts the contact travel. Using the 10 kA case as an example, this is reflected by the travel curves presented in Figure 4.17. At around 37 ms, the predicted travel (without reaction force) is ahead of the measured one by 40 mm, which is 18% of the total travel. With the introduction of reaction force, the system experiences more resistance. As a result, a significant improvement can be seen in the predicted travel, the maximum difference is reduced to 30 mm, 13% of the total travel.

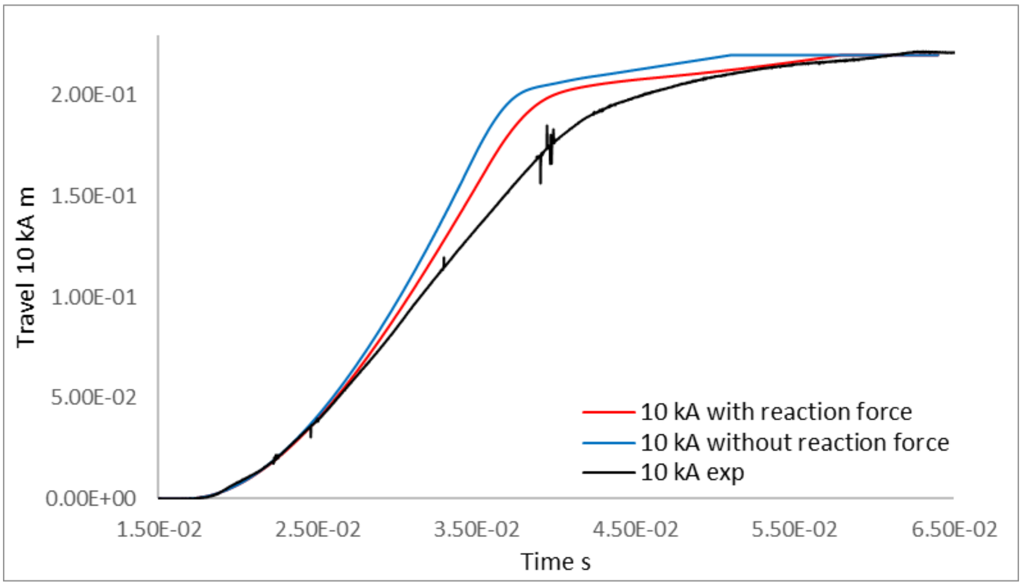

Figure 4.17 10 kA travel curves with and without considering reaction force.

4.3.2 Friction in hydraulic cylinder

During the operation of the hydraulic driving mechanism, not only the movement of mechanical parts, but also the flow of fluid is involved. The flow of hydraulic oil involves complex mechanisms such as viscous friction, which is introduced due to the contact between solid parts and fluid. The total contacting surface area between the fluid and solid in the hydraulic cylinder is difficult to estimate. Furthermore, contacting surfaces between solids also introduce additional sources of friction, for example the rubber seals installed between the piston and cylinder housing. To account for all these sources of friction requires detailed knowledge of the structure of the cylinder, surface conditions and contact area between the piston-rod assembly and hydraulic oil [98]. Consequently, to incorporate all these factors in a simplified 1-D model is problematic. Instead, by assuming the total frictional force is related to the velocity of the piston, a single coefficient is introduced in an attempt to account for the total frictional forces. Doing so will inevitably result in inherent errors that are responsible for the difference between predicted and measured results (see Figure 4.17) being included in the driving mechanism model. To overcome this difficulty, the semi-empirical friction coefficient should be calibrated according to measurement data.

Initially, the friction coefficient for the piston-rod assembly is set to a constant (with a value of 1250 N/(m/s)). Under this condition, the system is underdamped. To compensate the underdamping, the value of the friction coefficient is increased to 1900 N/(m/s). However, a satisfactory result still cannot be obtained, the piston experiences over-damping in the first half of the travel and under-damping in the second half (see Figure 4.18). At this point, it is apparent that such setting (constant friction coefficient) does not reflect true reality, since due to the movement of the piston, the contact area changes constantly. According to the structure of the cylinder and the motion characteristics of the piston itself, it has been found that this coefficient should be divided into two parts, i.e.:

$$B_{v3} = a_f + b_f(x_3) \tag{4.1}$$

where B_{v3} is the viscous friction coefficient for the piston, a_f is the constant part of the coefficient, which represents the constant portion of the friction experienced by the piston. This part of the friction is mainly caused by the relative motion between the touching solid surfaces, such as between the sealing rings and cylinder wall. $b_f(x_3)$ represents the changing part of the coefficient, its value is affected by the movement of the piston, where x_3 is the displacement of the piston. Figure 4.18 depicts several travel curves obtained with different settings of B_{v3}. As can be seen in the diagram, the new coefficient formulated according to Equation (4.1) produces better results that are closer to the measurement.

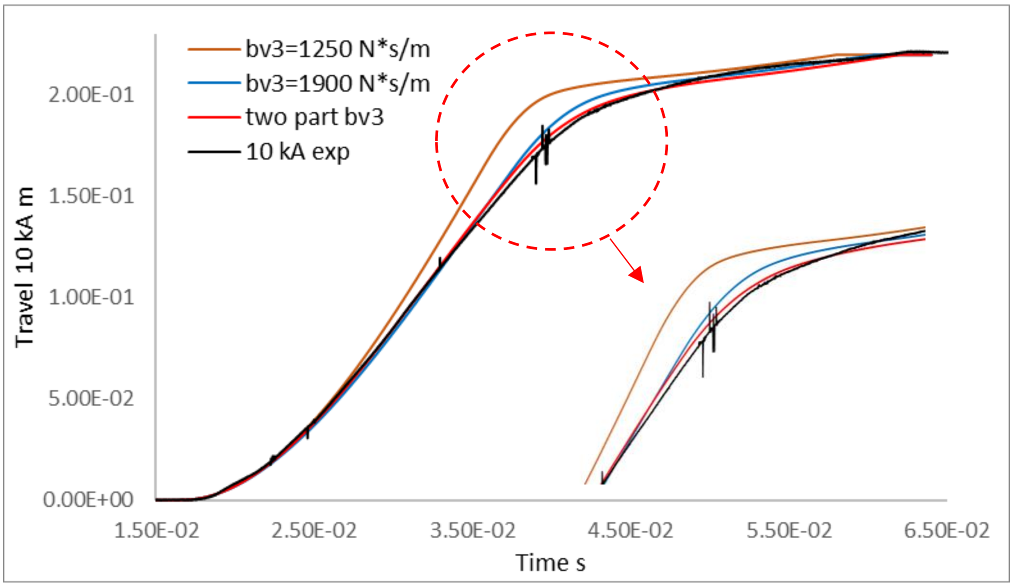

Figure 4.18 Travel curves obtained with different friction coefficients for 10 kA case.

In Figure 4.18, the brown curve represents the travel with original B_{v3} setting (1250 N/(m/s)), for comparison, the blue curve is obtained with a constant B_{v3} with a relatively higher value (1900 N/(m/s)), the red curve represents the optimum setting for B_{v3} and the black curve is the measured travel curve. The new value for B_v is found to be:

$$B_{v3} = 1300 + 9090(x_3)$$

4.3.3 Reaction force calibration

After tuning the s friction coefficient, under 50 kA conditions, the predicted travel still differs rather considerably from the measured travel, this illustrated by Figure 4.19. Considering the arc will have a greater impact on pressure distribution under high current conditions, it is reasonable to conclude that this residual discrepancy stems from the inaccuracy in calculating the pressure distribution in the arc chamber. As can be seen in Figure 4.11, under high current conditions although the measured and predicted pressure share a similar profile, differences between the two curves are still significant. Their instantaneous value can differ as much as 1 MPa in some instances, which is quite substantial. This difference is caused by the error in calculating the instantaneous pressure field in the arc chamber, the cause of which can be hard to determine. In the 50 kA case, the accuracy of pressure prediction is related to:

a) The total energy dumped into the arcing space and size of arc column. This will affect the size of the arc column which could partially and in some extreme cases completely block the flow channel from the compression chamber to downstream.
b) The mass rate of ablated PTFE material. Ablation is a significant factor affecting pressure in the compression chamber at high current. Although not design like an auto-expansion breaker, the ablated vapour in a puffer type circuit breaker still flows back into the compression chamber when pressure the contact gap is high.
c) Change in arc chamber geometry. The PTFE nozzle is subjected to erosion and ablation under high current conditions which resulted in different nozzle diameters. Previous research has indicated that the nozzle diameter can substantially affect the

flow condition in the arc chamber [99][100].

Collectively, these factors introduce uncertainties in pressure prediction. Considering their coupled nature, accurately fine-tuning all relevant parameters to achieve better agreement between measured and predicted pressure is difficult. In addition, implementing a new mechanism that can keep track the change in nozzle diameter (caused by ablation) and adjust the computational domain accordingly is beyond the scope of the current study. Therefore, further calibration is needed to improve the accuracy of coupled simulation model. To account for the difference in calculated and measured pressure, a new coefficient is introduced, i.e. B_r, with this new coefficient, the total reaction force from the arc chamber is:

$$F_r = B_r \int P \cdot dA \tag{4.2}$$

where F_r is the total reacting force, dA is the elementary area, P is the corresponding pressure.

Based on Equation (4.2), several values for B_r are tested, the results are presented in Figure 4.20.

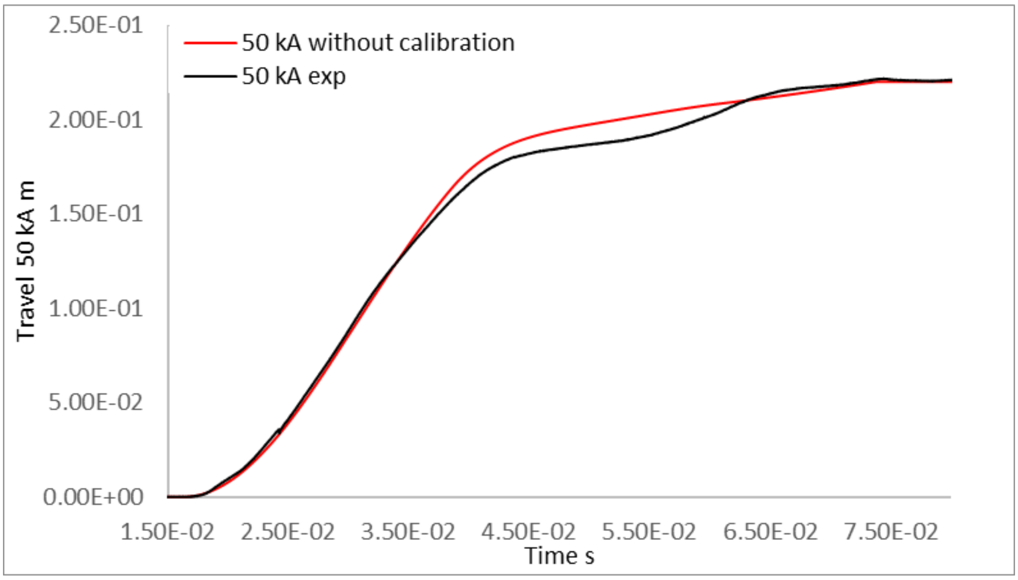

Figure 4.19 Comparison between measured and predicted travel for the 50 kA after friction coefficient adjustment.

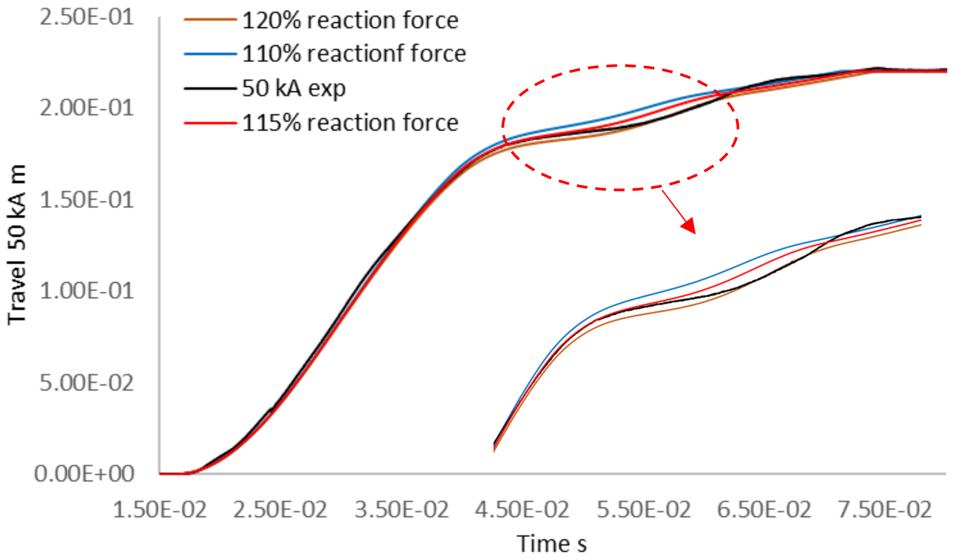

Figure 4.20 50 kA travel curves after the introduction of B_r.

Figure 4.20 shows that considering there is an average 15% - 20% difference in pressure calculation, value for B_r should be selected accordingly, i.e. $B_r = 1.15 - 1.20$. It can be observed that with a 15% artificial increase in the reaction force, difference between the predicted and measured travel is minimized. The maximum difference in travel in this case is 4 mm, 1.8% and 2.0% of the total (220 mm) and instantaneous (198 mm) travel respectively. However, it should be pointed out that the coefficient B_r has no physical meaning. It only represents the difference between the predicted and measured travel. As a temporary solution, $B_r = 1.15$ is used in the parameter study which will be presented in the next chapter. To truly solve this problem and further improve the ability of the coupled model, effort has to be made to include all mechanism that could potentially affect the pressure calculation under high current conditions in the current arc model.

4.4 Conclusion

The validity of the arc model, the method for reaction force calculation and the coupled circuit breaker simulation model were all verified in this chapter.

a) Results including arc voltage and arc chamber pressure obtained via uncoupled circuit breaker simulations (the arc model was implemented in PHOENICS, travel curves in both cases were from measurements and provided to the arc model in the form of user-defined files) were compared with measurements in order to verify the validity of the arc model. It has been found that the arc model is able to predict the pressure change in the arc chamber with reasonable accuracy in under both low (10 kA) and high current (50 kA) conditions. The smoothened travel curves used in these reference simulations have a minor impact on the predicted arc chamber pressure.

b) The method for reaction force calculation was verified by both a simple test (see Section 4.2) and the calculated pressure in both reference cases. It has been found that the main component subjected to high pressure during arc quenching is the main nozzle and the pressure at nozzle upstream and inside the compression chamber has a decisive impact on the total reaction force.

c) Two calibration tests were performed in addition to the reference cases to counter the effect of inaccuracies within both the driving mechanism and the arc model. In these cases, coupled circuit breaker model was used. It has been found that after modifying the frictional coefficient of the piston (in the main hydraulic cylinder), the coupled model was able to obtain satisfactory results under the 10 kA condition. The calculated travel in this case, agrees well with the measured travel (with a maximum error of 1.9% and the maximum difference between measured and predicted travel being 4 mm). A new coefficient (B_r) has to be introduced due to the fact that the arc model tends to under-predict the pressure inside arc chamber under high current conditions (see Figure 4.11). The likely cause of this inaccuracy was explained in Section 4.3.3. After the introduction of this new coefficient, a good agreement between measured and predicted travel can also be achieved under high current conditions.

Chapter 5 Study of a 252 kV Puffer Circuit Breaker with Different Arcing Conditions and Nozzle Geometries

5.1 Introduction

The ultimate design purpose is to produce a circuit breaker for a given rating with best possible interruption capability and least cost. As stated before, in the interruption process a circuit breaker undergoes two interlinked critical processes, i.e. the thermal recovery and dielectric recovery processes. The thermal recovery process is concerned with energy removal from the contact space. A successful thermal recovery will lead an overall decrease of temperature in the contact space. The dielectric recovery process is concerned with the removal of free charges (electrons and ions) from the residual plasma so the gas in the contact space can withstand high system recovery voltage without suffering a breakdown.

Number of factors come into play when determining the interruption capability of a circuit breaker, they can be broadly categorized as:

a) The mechanical aspects (mainly the dynamic characteristics (such as contact travel and speed) of the driving mechanism) is responsible for the position of the moving contact when the current reaches its final zero. The length of the contact gap is an important parameter since it affects the interruption process and the total resistance of the contact space in both high current and post arc period.

b) The arcing history (this includes the electrical parameters such as current waveform and magnitude) is important in determining the conditions at current zero, the total energy dissipated within the arcing space has a significant impact on the distribution of physical parameters such as temperature and pressure through nozzle ablation and self-pressurization of the heating chamber in self-blast circuit breakers.

c) To estimate how effectively energy is being exchanged between the arc and the surrounding flow, the flow condition both prior to and at current zero is needed. The flow condition is in turn affected by the arc, movement of solid objects and arc chamber geometry (this include structural parameters such as nozzle throat length and radius).

Clearly, these factors are closely coupled during the arcing process and a change in any of them could potentially affect others. The aim of this section is to investigate how certain changes in these parameters could affect the performance of the breaker. In addition, finding out what role the reaction force plays during the arcing process.

When the arc approaches its final current zero, the arc column shrinks rapidly due to convective and turbulent cooling. Previous studies have shown that turbulence enhanced energy transfer is an important cooling mechanism in the thermal recovery process [101].

Starting from the solution obtained at the end of the current zero period simulation, the behaviour of the plasma left between the two contacts can be assessed by applying different rates of rise of recovery voltage (RRRV). The post arc current under different RRRVs can be obtained by running a number of simulations. A RRRV can then be found below which the post-arc current will eventually decrease following an initial rise in a time scale of up to 10 μs. This RRRV is called the critical RRRV and is a direct measure of the thermal interruption capability of the circuit breaker under investigation.

To calculate the energy source under a certain recovery voltage, the following steps are used to derive the electric field and Ohmic heating:

1 Calculate the resistance of each slice of the plasma column which is divided by the grid system. This is done by using the following equation:

$$R_{slab} = \frac{\Delta z}{\int_{axis}^{r_{3k}} \sigma 2\pi r dr} \tag{5.1}$$

where Δz is the thickness of one slice of plasma column, integration is performed from the axis to the first point of 3000 K from the axis.

2 The resistance for each slice is added up to form the total resistance of the plasma column between the two contacts.

3 Use Ohm's law to calculate the current that flows through the plasma column.

4 Using the current to calculate the electric field and current density in each slice assuming that a uniform axial electric field applies to the slice because the radial electric field components is negligible in the post-arc phase.

5 Calculate the Ohmic heating and radiation loss to obtain the total energy source term at each cell in the plasma column for the energy conservation equation.

The temperature distribution on the axis between the contacts after current zero is given in Figure 5.1 for 5 instants with a RRRV of 0.5 kV/μs (for a 50 kA case, with long arc duration). The turbulence parameter used in the simulation ($c = 0.15$) is calibrated based on measured arc voltage (the turbulence parameter used in the Prantl Mixing Length model is dependent on nozzle geometry, ideally, for each case, the turbulence parameter should be calibrated with measured data).

In this case the thermal recovery process is successful and temperature in the contact space decreases steadily within 5 μs. Further increase in the applied RRRV will lead to a higher post arc current and if the RRRV is above a threshold value, say above 2.5 kV/μs roughly, the current will rise violently after a period of stable discharge. This can be seen clearly in Figure 5.2 where the post-arc current is given for 6 RRRVs with a 1 kV/μs interval. An applied RRRV below 2.5 kV/μs will lead to a steady decrease in the post-arc current and the contact gap will thermally recover. On the contrary, an applied value of higher than this threshold will eventually lead to a thermal re-ignition and result in thermal failure of the interruption process.

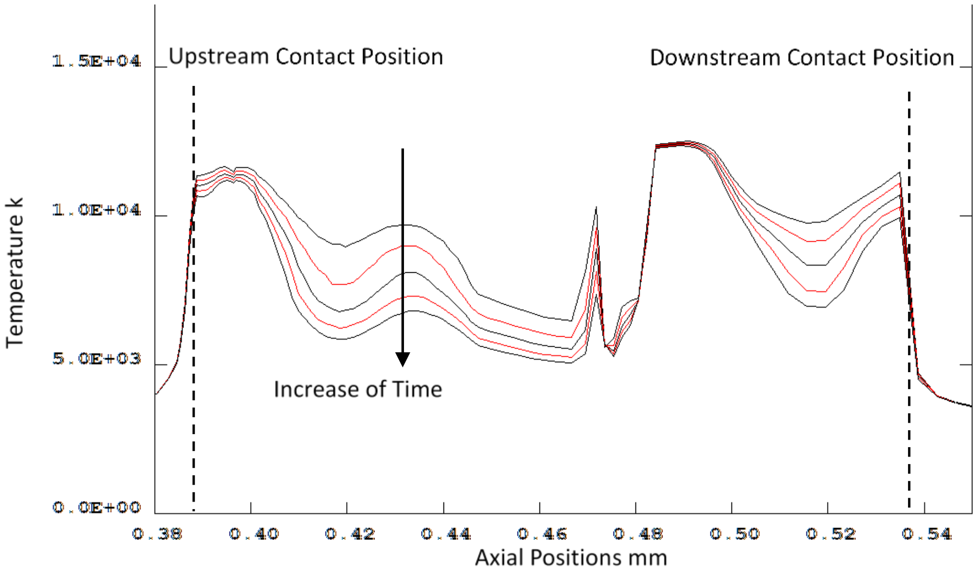

Figure 5.1 Axial temperature distribution in the contact space after current zero for the 50 kA coupled simulation. The applied RRRV is 0.5 kV/μs. From top to bottom: 1 μs, 2 μs, 3 μs, 4 μs and 5 μs.

This shows that the developed simulation model is able to perform the critical RRRV calculation based on solutions from the current zero period simulation. However, it must be noted that the accurate determination of the critical RRRV is still not possible due to uncertainties in the modelling of turbulence under plasma conditions. Prandtl mixing length model and the K-epsilon model both need adjustment to their parameters in order to bring modelling results to agree with temperature measurement. Therefore, to reliably predict the thermal interruption capability of a breaker, data obtained from experiments is needed to perform said calibrations.

For a given design, it is likely that the critical RRRV is not a unique value. Experimental uncertainties or the nature of the problem itself could lead to different critical RRRV values.

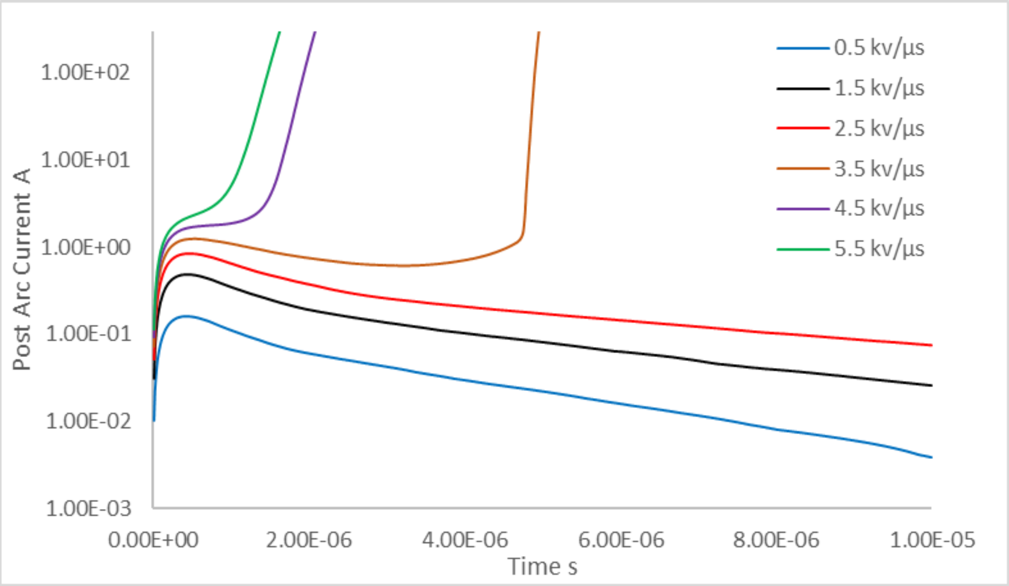

Figure 5.2 Post arc current as a function of time under different applied RRRVs for the 50 kA coupled simulation. The critical RRRV in this case can be identified as 2.5 kV/µs. An applied RRRV above this rate will eventually result in a thermal re-ignition.

5.2 Parameters Under Investigation

To investigate how the interruption capability of a circuit breaker (puffer type) is affected by changes in different parameters, a number of simulations were performed based on the circuit breaker arc chamber introduced in Chapter 4 (see Figure 4.1). To ensure a comprehensive understanding of the arcing process, two main groups of parameters have been modified:

a) Arcing conditions, these include different current levels (10 kA and 50 kA RMS value) and arc durations (17.72, 15.72 and 13.72 ms).

b) Arc chamber structural parameters, these include changes in nozzle flat throat length and nozzle diameter.

5.2.1 Fault current level

The critical RRRV for the 10 kA case is found to be 2.2 kV/µs while in the 50 kA case the circuit breaker is able to withstand a higher RRRV of 3.0 kV/µs. With the same driving mechanism, under different current level (10 and 50 kA), the predicted travel curves differ considerably as demonstrated in Figure 5.3. In both 10 and 50 kA cases, the arc was initiated at the same instance (t=10.60 ms), together with current zero in each case, these are marked by the dashed blue lines in Figure 5.3.

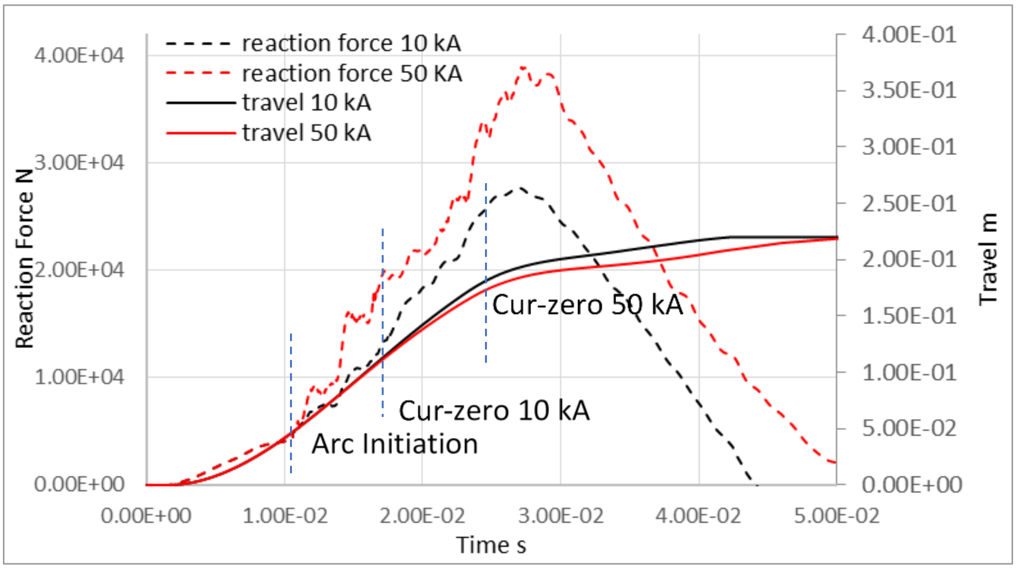

Figure 5.3 Travel and reaction force comparison of 10 and 50 kA coupled simulations with the same driving mechanism.

As can be seen in Figure 5.3, in the first 3~4 ms following arc initiation, the 10 and 50 kA reaction force are both increasing rapidly and the difference between them is relatively small. As a result, the travel curves are nearly identical in this time period. This is because for the 50 kA case, the current has to be ramped up to its instantaneous value from a relatively low starting point (3 kA). After this procedure is completed (in approximately half of a millisecond), the instantaneous current in the 10 and 50 kA cases are quite different. Therefore, after the initial period, differences in travel and reaction force becomes more and more visible. In the 10 kA case, the reaction force reached a peak value of 28 kN at t=29 ms. The maximum reaction force of the 50 kA case is 39 kN which also occurred in the same instance. For these two cases, the maximum difference in reaction force happens to be found at the peak values of the force. Similar disparity can be found in the predicted arc chamber pressure shown in Figure 5.4. The 50 kA case has recorded a higher pressure in all three locations (at monitor point 1, 2 and 3, see Figure 4.2). In the compression chamber, the maximum pressure in the 50 kA case reached 2.4 MPa while in the 10 kA case the maximum pressure at the same location is only 1.9 MPa, pressure at nozzle upstream shows a similar difference.

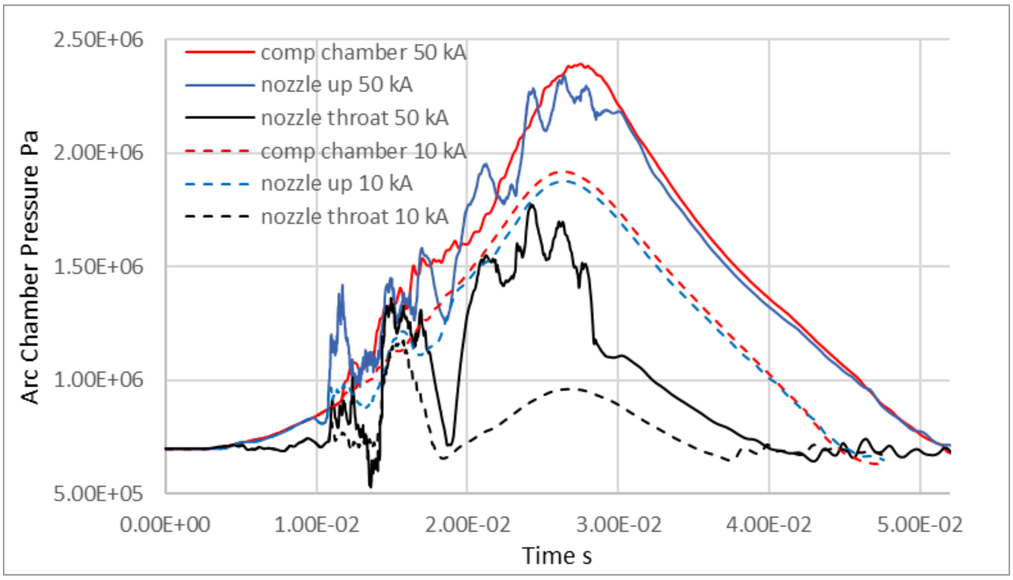

Figure 5.4 Predicted arc chamber pressure at three different locations (compression chamber (comp chamber), nozzle upstream (nozzle up) and nozzle throat) for the 10 and 50 kA cases.

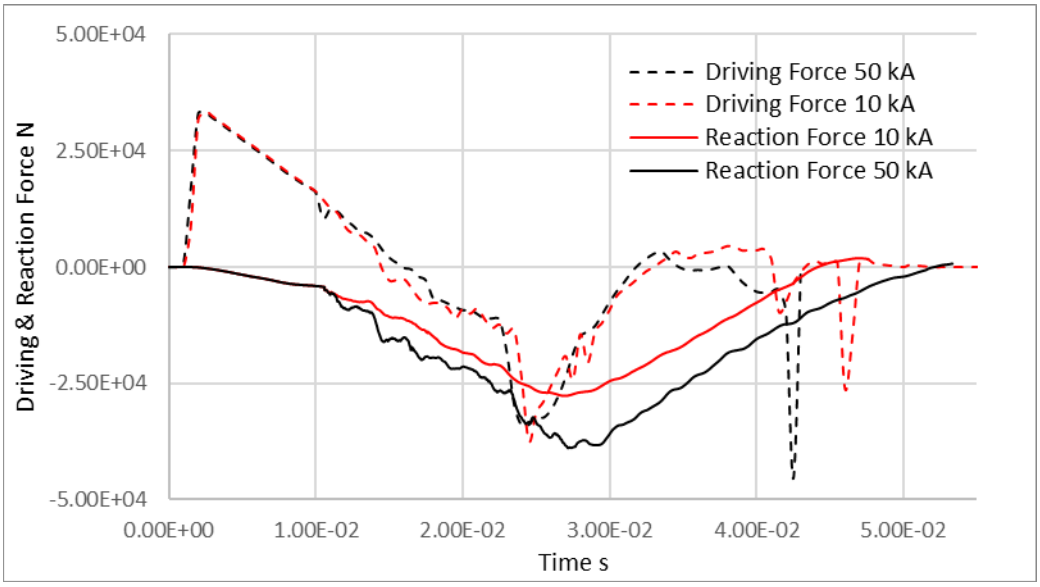

Figure 5.5 Reaction force and driving force for both 10 and 50 kA cases.

Further examining the recorded arc chamber pressure of both cases presented in Figure 5.4, it is clear that the peak of reaction force coincides with the peak upstream pressure (compression chamber and nozzle upstream). This can be easily explained as the high pressure areas in the arc chamber are almost always concentrated at the compression chamber and nozzle upstream area. Therefore, pressure in these areas has a dominant effect on the magnitude of the reaction force making the peak reaction force occurring at the same time as the peak pressure. The maximum difference in travel does not appear at the same time as reaction force. In fact, the maximum difference between the two travels is 14 mm which occurred at t=38 ms.

The reaction force recorded in each case is also compared with the driving force (output of the driving mechanism, which is the net force (this includes the reaction force itself, as a result, the difference between the driving force and reaction force in Figure 5.5 can be considered as the positive force that is actually pushing the piston toward the end of travel) exerted on the piston in the hydraulic cylinder) provided by the driving mechanism, as shown in Figure 5.5. In Figure 5.5, the reaction force is shown as negative since for the majority of the time, the total net reaction force is in the opposite direction of piston movement. It can be seen that in both cases, the driving mechanism produces similar outputs expect in the cushioning process (from 24 to 50 ms in Figure 5.5). For example, at t=42 ms, the piston has a higher speed during the cushioning process in the 50 kA case (at around t=42 ms, the piston speed in the 50 kA case is 1.9 m/s while in the 10 kA case it is 1.5 m/s) and a higher negative force is produced correspondingly (at around t=42 ms).

Initially (the first 10 milliseconds in both simulations), the reaction force is small compared with the driving force of the driving mechanism. The maximum driving force reached in both cases by the driving mechanism is 36 kN, at this moments, the reaction force is below 200 N in both cases. As a result, for the first 15 ms or so, the reaction force in both cases has little impact on the travel, even though visible difference in reaction force can be spotted between the two cases (see Figure 5.3). From 35 ms to 42 ms, a large difference in driving force can be seen between the two cases. During this period of time, the 10 kA has a smaller reaction force and a larger driving force. Consequently, travel in these two cases also starts to differ significantly in this period. So it can be said that it is within this period of time, in which the reaction force is comparable to the positive force driving the piston, disparity in the reaction force can lead to significant difference in travel as well.

The higher pressure build up at nozzle upstream (see Figure 4.2) in the 50 kA case can be attributed to the higher fault current. Figure 5.6 compares the temperature distribution in the arc chamber for both cases at t=15.15 ms. Notice at this moment, the moving hollow contact (see Figure 4.1) is still inside the nozzle, combined with the presence of the arc, the nozzle is effectively blocked. The pressure builds up at nozzle upstream for both cases at this moment, but due to the higher current in the 50 kA case, both ohmic heating and ablation are considerably stronger than the 10 kA case. Consequently, at this stage in the 50 kA case, the flow is essentially reversed and hot gas from the arc core region flows back into the compression chamber, thus creating a much higher pressure rise in the compression chamber. Figure 5.7 provides the axial component of the gas velocity at the exit of the compression chamber (the position of the exit marked in Figure 5.6). It can be seen in the 10 kA case, the flow is rather stagnant at this point and the axial speed of the outflow is barely visible. This is because in the 10 kA case, Ohmic heating provided by the arc is much less effective so no visible backflow is generated. In the meantime, the pressure in the arc region (1.22 MPa measured at monitor point 2) is slightly higher than the pressure inside the compression chamber (1.18 MPa measured at monitor point 1), combined with the fact that the downstream contact is still within the nozzle flat throat, a significant outflow also cannot be established at this moment. On the other hand, the flow direction is clearly reversed in the 50 kA, indicating a strong backflow entering the compression chamber.

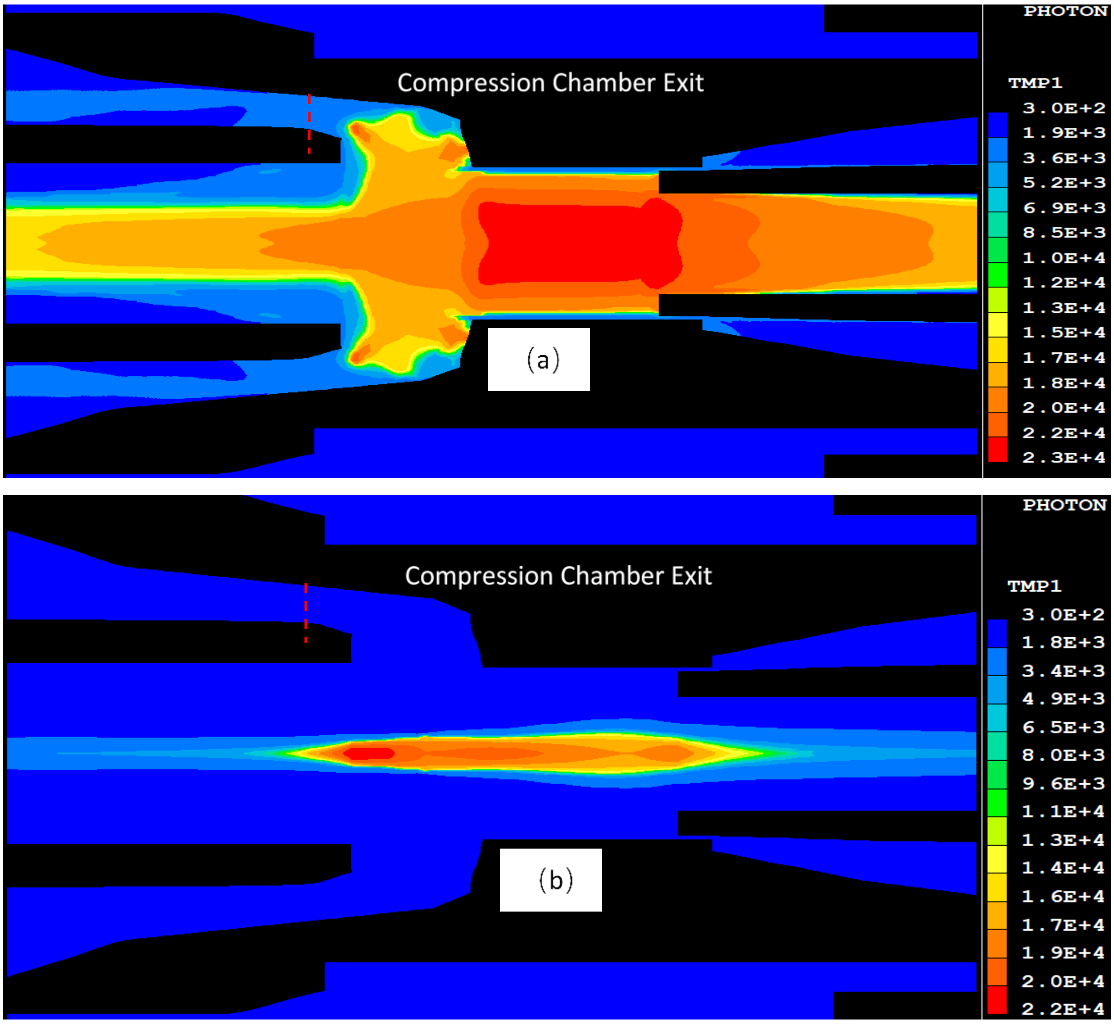

Figure 5.6 Temperature contour of the arc for both 50 (a) and 10 (b) kA cases taken at t=15.15 ms, the instantaneous current for 10 and 50 kA cases are 2044.1 and 61443.1 A respectively.

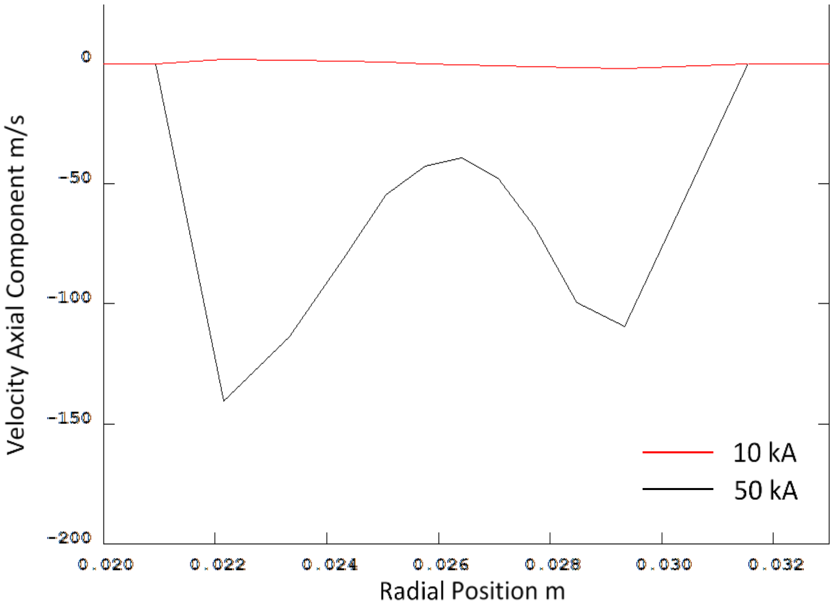

Figure 5.7 The axial component of flow velocity at the exit of compression chamber for both 10 and 50 kA cases, t=15.15 ms.

Another cause for the higher pressure at upstream in the 50 kA case is that due to significantly higher current, the arc radius is larger compared with the 10 kA case. As a result, the arc blocks off the flow channel more effectively in the 50 kA case. Figure 5.8 presents the temperature contour of the arc for both 10 and 50 kA cases taken at t=16.10 ms. At this moment, the downstream contact had cleared the nozzle throat in both cases. In the meantime, due to the large radius, the arc completely occupies the nozzle in the 50 kA case and the gas accumulated at upstream cannot be easily discharged. Figure 5.9 provides the axial component of flow velocity at the exit of compression chamber at this instance.

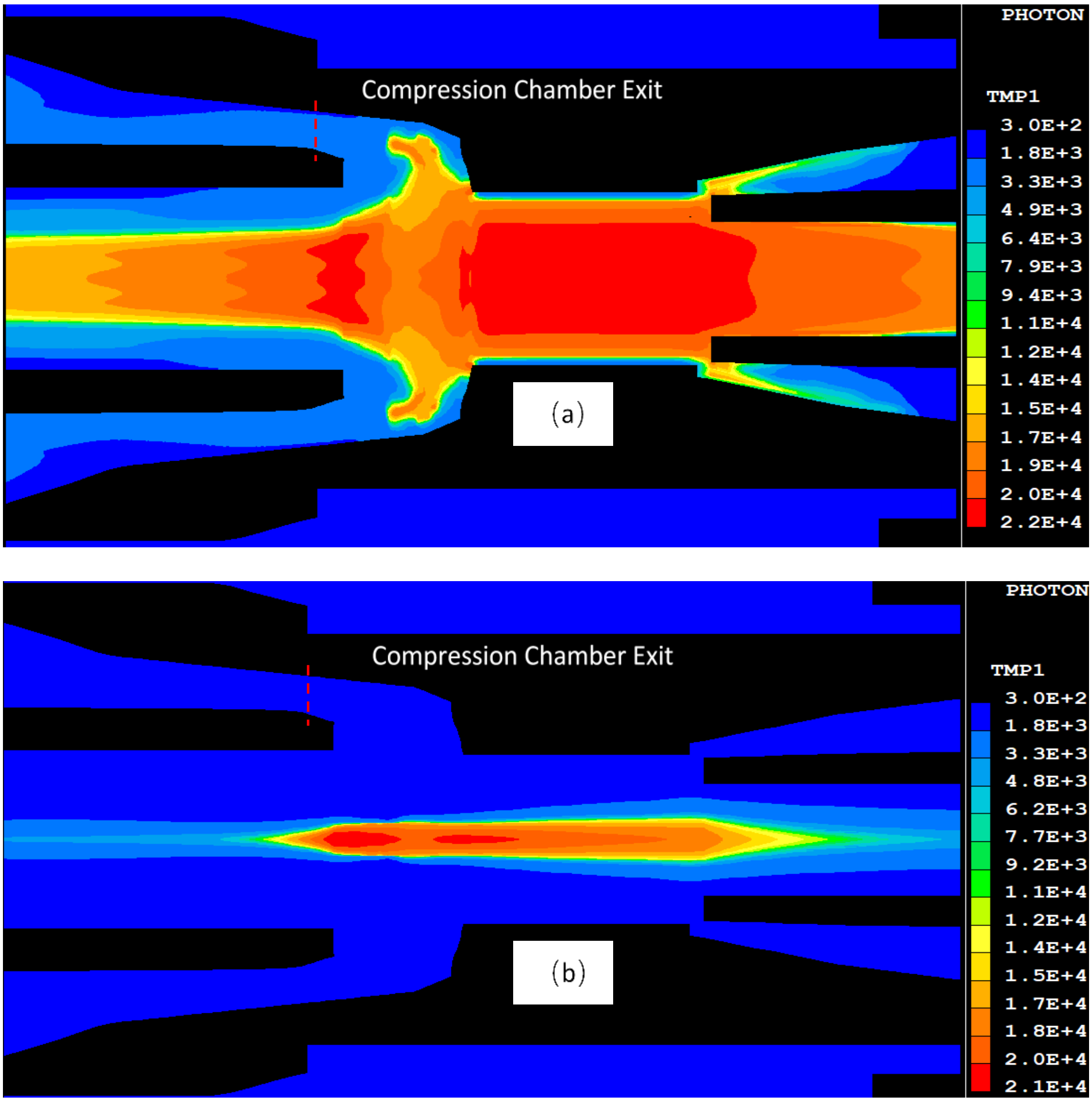

Figure 5.8 Temperature contour of the arc for both 50 (a) and 10 (b) kA cases taken at

t=16.10 ms, the instantaneous current for 10 and 50 kA cases are -2498.2 and 51004.3 A respectively.

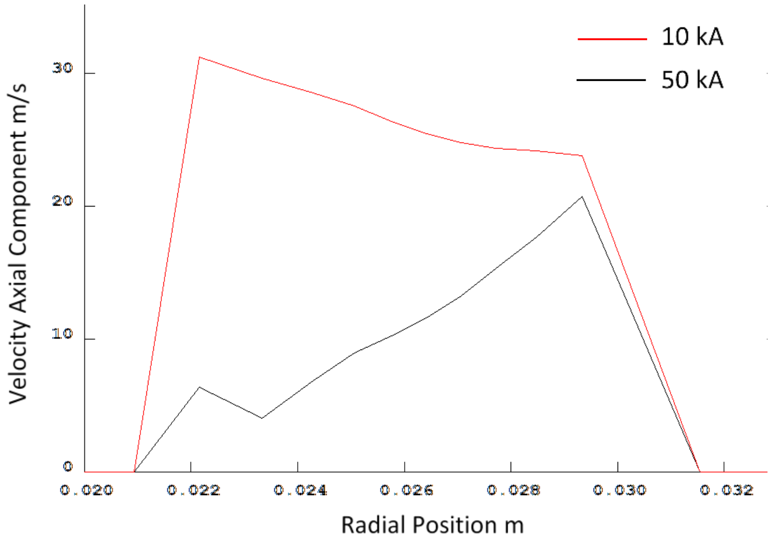

Figure 5.9 The axial component of flow velocity at the exit of compression chamber for both 10 and 50 kA cases, t=16.10 ms.

At this point, although an outflow has been established in both cases, due to the arc severely clogging the flow channel at downstream, the outflow in the 50 kA case is considerably smaller than that of the 10 kA case. Collectively, these mechanisms lead to a much higher pressure build-up at the upstream of the nozzle in the high current case.

In the 50 kA case, due to the higher current, at current zero, temperature in the contact space is higher than the 10 kA case. This is demonstrated in Figure 5.10, where the axis temperatures at current zero in both cases are given.

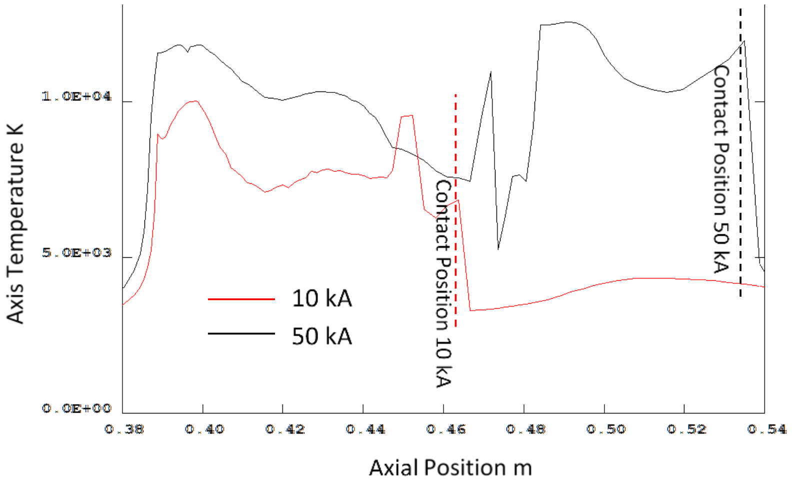

Figure 5.10 Axis temperature at current zero for 10 and 50 kA cases. Note the different downstream contact positions.

Axis temperature in the 10 kA case at current zero does not exceed 10000 K, whereas in the 50 kA case, a higher residual temperature in the contact space is observed. This indicates a higher conductivity distribution along the axis in the 50 kA case, which can be seen in Figure 5.11.

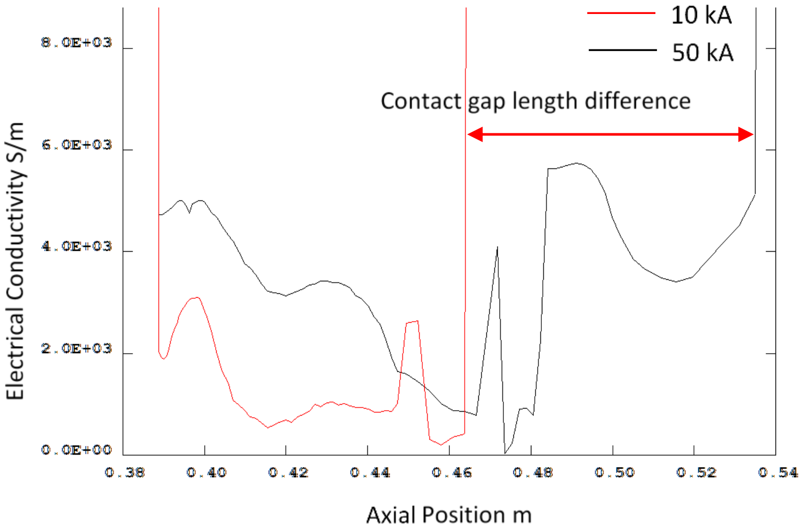

Figure 5.11 Axis temperature at current zero for 10 and 50 kA cases.

The spikes seen in both axis temperature and conductivity near the downstream contact is caused by the contact obstructing the path of the flow, creating a stagnated region (in which axial flow are severely restricted, result in a higher axis temperature and conductivity) in front of the contact.

Since arc durations are different in these cases (7.0 and 17.72 ms for 10 and 50 kA respectively), length of the contact gap at final current zero is also different (see Figure 5.11). As a result, the gap in 50 kA case has a higher overall resistance and is able to withstand a higher applied voltage. Moreover, the fact that arc duration is longer in the 50 kA case has allowed the pressure to reach a higher value at the upstream of the main nozzle. This is reflected in Figure 5.12, where the axis pressure of both cases is compared.

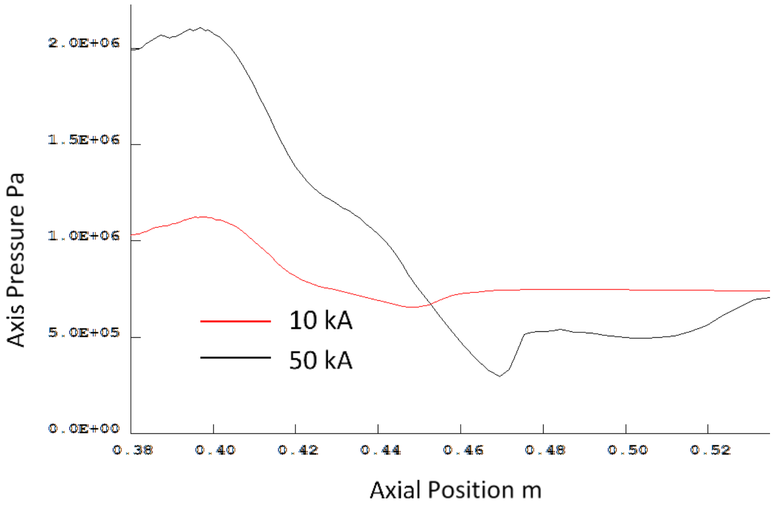

Figure 5.12 Axis pressure at current zero for 10 and 50 kA cases.

Evidently, at current zero, the 50 kA case has a doubled upstream pressure when compared to the 10 kA case. This contributes towards a higher axial flow velocity, as shown in Figure 5.13.

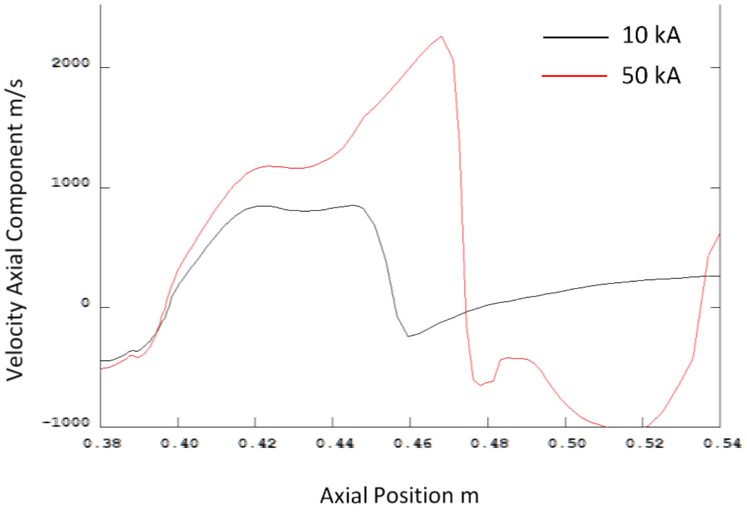

Figure 5.13 Axis velocity (axial) at current zero for 10 and 50 kA cases.

Since during current zero phase, the arc is normally burning in axially dominant flow [13], higher axial flow velocity can help the gap to cool down more effectively. Therefore, in addition to the longer contact gap, the 50 kA case also benefited from a higher upstream pressure which also contributes to a higher critical RRRV.

5.2.2 Arc duration

A circuit breaker needs to perform different switching duties in their service with different arc durations. Therefore, it is important to see, with the same current level (in terms of RMS value) how variation in arc duration can affect the performance of a circuit breaker. The standard test current (used in the verification test presented in chapter 4) waveform, together with modified current waveforms for the medium and short arc duration cases are presented in Figure 5.14. Being the same as the 50 kA case in the current level comparison, RRRV for the long arc duration case is 3.0 kV/µs, the RRRV for both medium and short arc duration cases is 2.7 kV/µs. For all three cases, the arc chamber geometry is identical to the one used in the verification tests, with the same filling pressure of 0.7 MPa, maximum contact travel of 220 mm and a 40 mm initial overlap between the contacts.

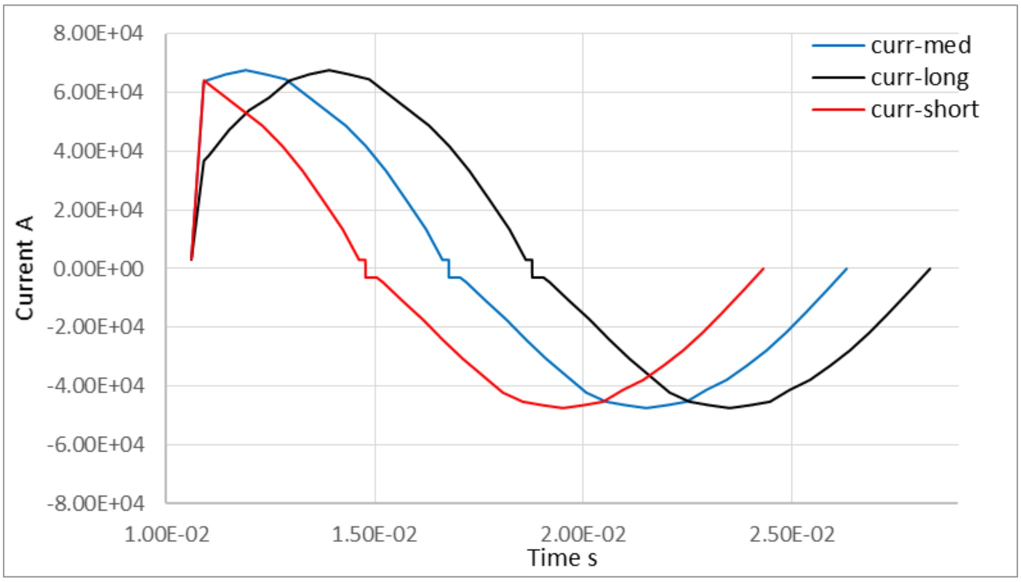

Figure 5.14 Current waveforms used in the arc duration study, duration for the long, medium and short arc cases are: 17.72, 15.72 and 13.72 ms.

The reaction forces recorded in all three cases are shown in Figure 5.15. For easy analysis, instead of time, the reaction force from each case is plotted against its corresponding travel. It can be observed in Figure 5.15 that the reaction force from all three cases generally behave similarly throughout the entire travel with clear and significant differences can be observed between 85~140 and 180~190 mm of travel. For the first section (80~140 mm), the travel in all cases is nearly identical as shown in Figure 5.16. In this stage, the reaction force is smaller than the driving force provided by the driving mechanism so difference in travel is small (this is reflected in Figure 5.19)

Consequently, the compression motion in each case is expected to produce similar pressure rise and difference in reaction force should be attributed to the arc.

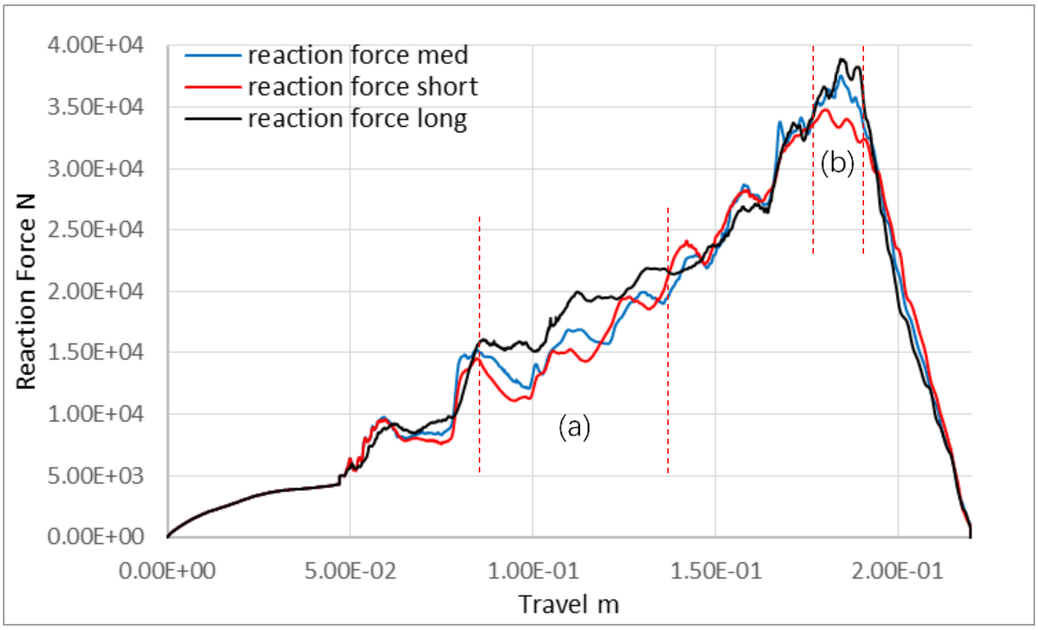

Figure 5.15 Reaction force plotted against travel for the long, medium and short arc duration cases. Two sections of travel in which the recorded reaction force is different are marked in the diagram.

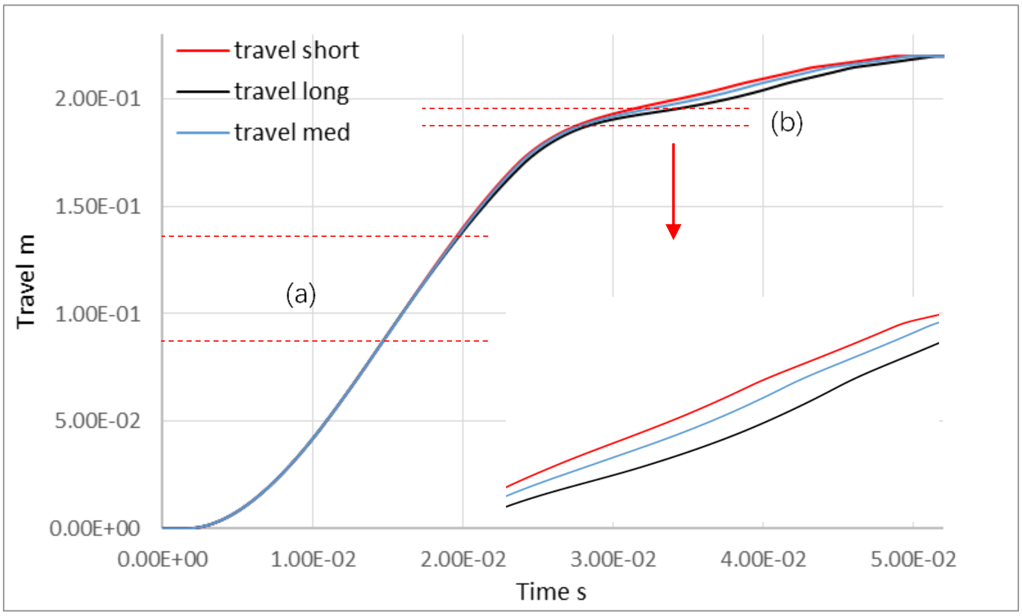

Figure 5.16 Travel curves for the long, medium and short arc duration cases. Two sections of travel in which the recorded reaction force is different are marked in the diagram.

By further examining the pressure rise in the arc chamber in all three cases, it can be seen that during this time period (section (a) in Figure 5.15), the instantaneous pressure in the long arc case is slightly higher (see Figure 5.17). It has been established in previous discussion that pressure oscillation in the compression chamber under the high current condition is a result of energy-related process and pressure wave propagation. In fact, by comparing the arc current during this stage, it is clear that the long arc duration case has a relatively higher current which resulted in a higher pressure in the compression chamber and ultimately the total reaction force. Immediately after this period (section (a) in Figure 5.15), at 145 mm travel, the instantaneous current in long arc case is 18153.4 A, much lower than both 46228.7 A in the medium and 44627.2 A in the short arc case, and the reaction force in medium and short arc case are both higher than the long arc case. This proves that the difference in reaction force in this period of time is caused by the variation of instantaneous current in different cases.

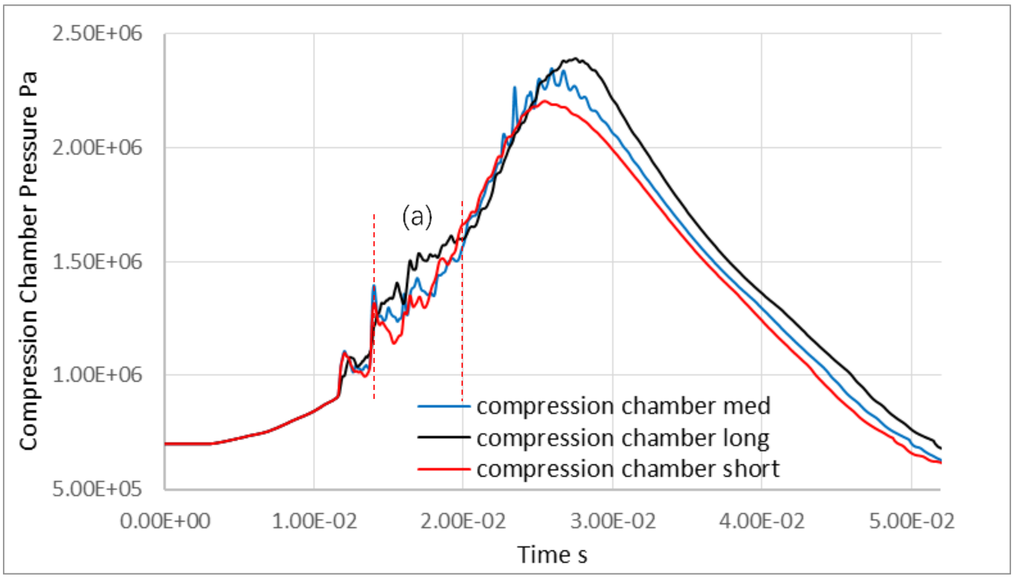

Figure 5.17 Pressure rise in the arc chamber for long, medium and short arc duration cases.

As for the second section, from 180 to 190 mm travel, it can be seen that the peak reaction force in all cases occurs at roughly the same point, in terms of travel, but as shown in Figure 5.16, at this stage, the travel in different cases are no longer close enough that the discrepancy can be ignored. So, plotting the reaction force against time (see Figure 5.18), the difference at their peak values can be more conveniently studied.

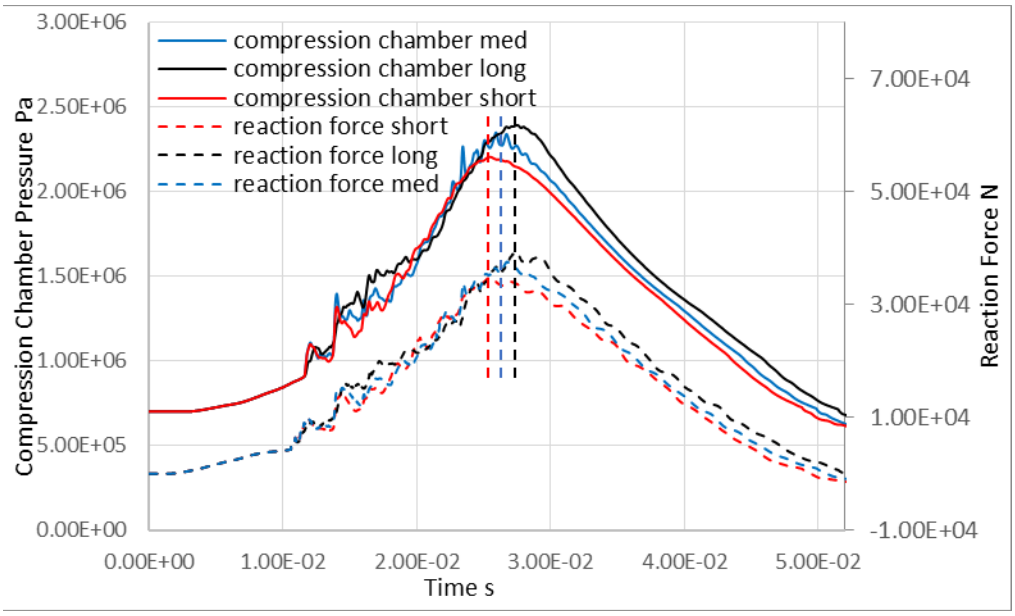

Figure 5.18 Reaction force for long, medium and short arc duration cases plotted against time, together with compression chamber pressure.

Also presented in Figure 5.18 is the compression chamber pressure in all cases. Notice the peak reaction force coincides perfectly with the peak chamber pressure. The difference in the maximum compression chamber pressure is rooted in the arc duration. The peak pressure for long, medium and short arc cases happened at 27.5, 26.0 and 25.5 ms respectively. Instances at which peak pressure appear is closely linked to the current zero point. Figure 5.20 shows the temperature contour for all three cases at t=24.3 ms. At this instance, the short arc case has reached current zero (Figure 5.20 (c)) and the arc becomes radially thin. This allows gas to be discharged through the nozzle nearly unimpeded. Although the compression in this case has not stopped, after a brief delay, a clear flow channel to the downstream eventually led to the pressure decrease in the compression chamber. In the meantime, for the long (Figure 5.20 (a)) and medium (Figure 5.20 (b)) arc cases, the instantaneous current has yet to reach current zero, and arc in both cases still occupies a large portion of the nozzle throat leading to a high pressure region blocking the flow to downstream. This explains the delay of peak pressure occurrence in longer arc duration cases and as the compression motion continues, a slightly higher maximum pressure is achieved in these cases as well. All these factors contribute to the difference in maximum pressure between all three cases.

On the other hand, from Figure 5.19, it can be seen that the reaction force is comparable to the positive driving force, so the difference in pressure in section (b) is enough to cause the travel in all three cases to differ.

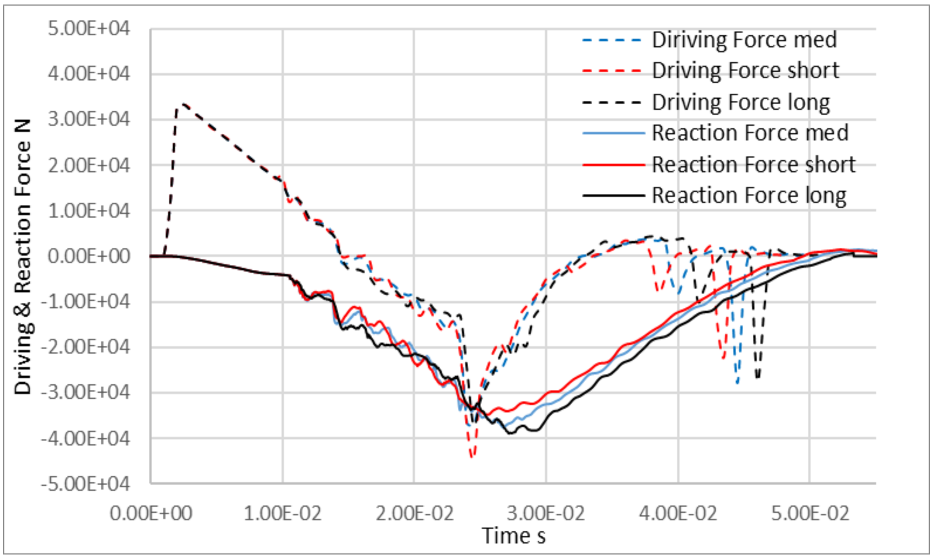

Figure 5.19 Reaction force and driving force for long, medium and short arc duration cases.

To conclude, the difference in reaction force in the second section (section (b) in Figure 5.15) is caused by nozzle clogging by arc column in the long and medium (to a lesser extent) cases and in this time period, the value of reaction force has risen to a sufficient level so difference in travel is also observed in this section.

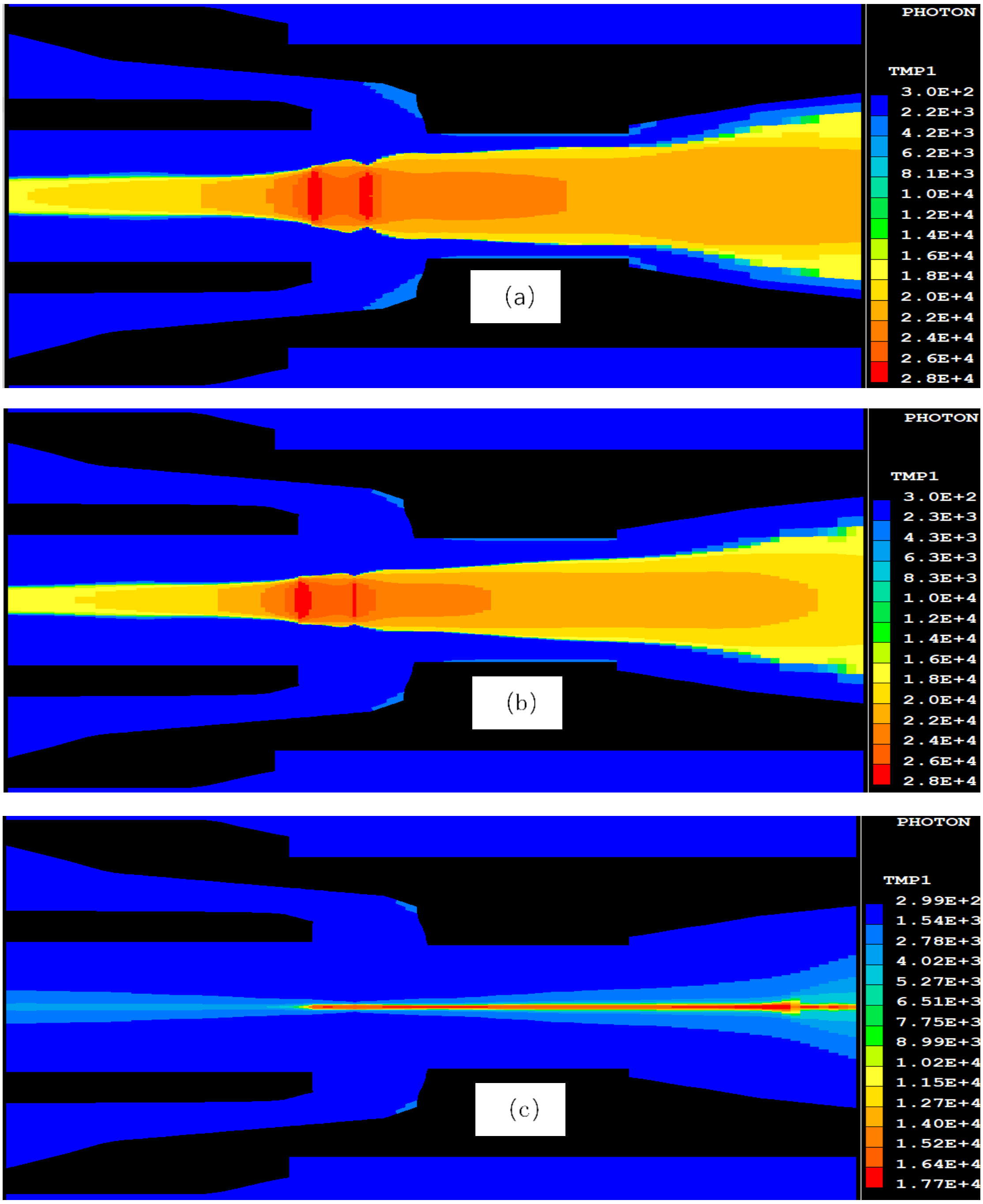

Figure 5.20 Comparison of temperature contour in the nozzle for long, medium and short arc duration cases at t=24.3 ms. (a) long arc duration, (b) medium arc duration, (c) short arc duration.

The critical RRRV not only depends on the pressure in the nozzles but also on the length of the arc column. In terms of length of the contact gap at current zero, due to the longer arc duration, the downstream contact is allowed to travel for a longer time in the long arc duration case. Although this process is somewhat impeded by the fact that the long arc duration also produces the strongest reaction force which resists the contact movement. Nevertheless, at current zero, in the long arc duration case, the downstream contact managed to achieve a travel distance of 187.46 mm, longest among all three cases. Naturally, the medium arc duration case ranks second in terms of gap length, which is 182.84 mm and the short arc duration case reached a gap length of 174.07 mm.

Figure 5.21 shows the recorded pressure at nozzle throat (monitor point 3) for all cases when approaching current zero. The short arc duration case has the lowest pressure (1.35 MPa) in the contact gap immediately before current zero, while in medium and long arc duration cases the recorded pressure is similar at around 1.50 MPa.

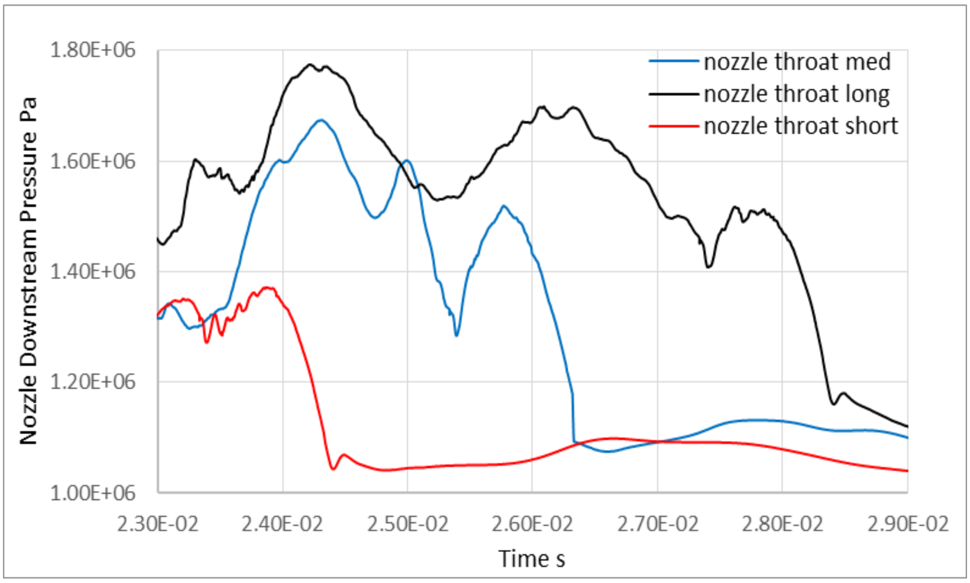

Figure 5.21 The pressure at nozzle throat immediately before current zero for long, medium and short arc duration.

Figure 5.22 shows the axis pressure distribution for all cases at the exact current zero. Along the axial direction, the long arc duration has the highest pressure in the contact gap while the short arc duration case produces the lowest. Together, Figure 5.21 and Figure 5.22 gives a general sense of how pressure is distributed in the contact gap before and at current zero.

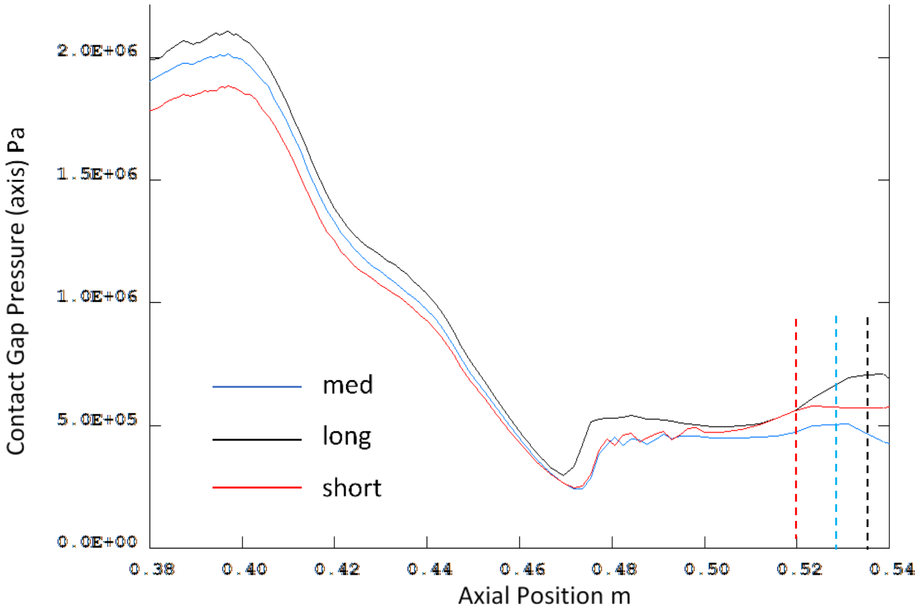

Figure 5.22 Axis pressure distribution for the long, medium and short arc duration cases at current zero. The dashed lines mark the tip of the downstream contact in each case.

Although the pressure in the arc chamber cannot be considered as uniformly distributed, pressure wave propagation often causes variation in local pressure. However, based on the above results, it can be concluded that the longest arc duration leads to the highest overall pressure in the contact gap, combined with the longest contact gap length, both factors contributes to the superior critical RRRV of the long arc duration case. Despite the difference in contact gap pressure mentioned earlier, with a 2 ms difference in total arcing time between each case, the overall pressure as well as the total reaction force are not drastically different between each case.

5.2.3 Shape of the nozzle

Change of shape of the nozzle will alter the flow field at current zero and therefore the interruption capability of the breaker. With the same current, simulations presented in this chapter are designed to identify the effect of such changes.

5.2.3.1 Length of nozzle flat throat

The change of nozzle length is illustrated in Figure 5.23. In order to form a comparison, two cases were conducted with both the nozzle throat lengthened and shortened by the same amount (15 mm). The original length of the flat nozzle throat is 45 mm. Apart from the length of the nozzle flat throat, the rest of parameters (including arcing current) are kept identical to those in the 50 kA long arc duration case mentioned in Section 5.2.2. The travel and reaction force recorded in the 50 kA long arc duration case are used as references.

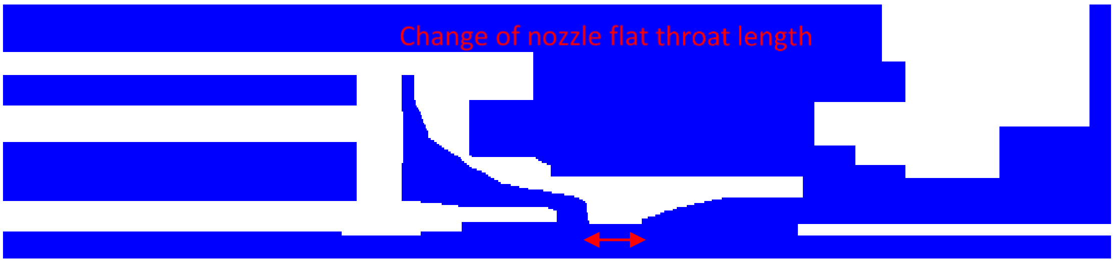

Figure 5.23 Demonstration of change of nozzle length.

The reaction force and contact travel with both lengthened and shortened nozzle are presented in Figure 5.24.

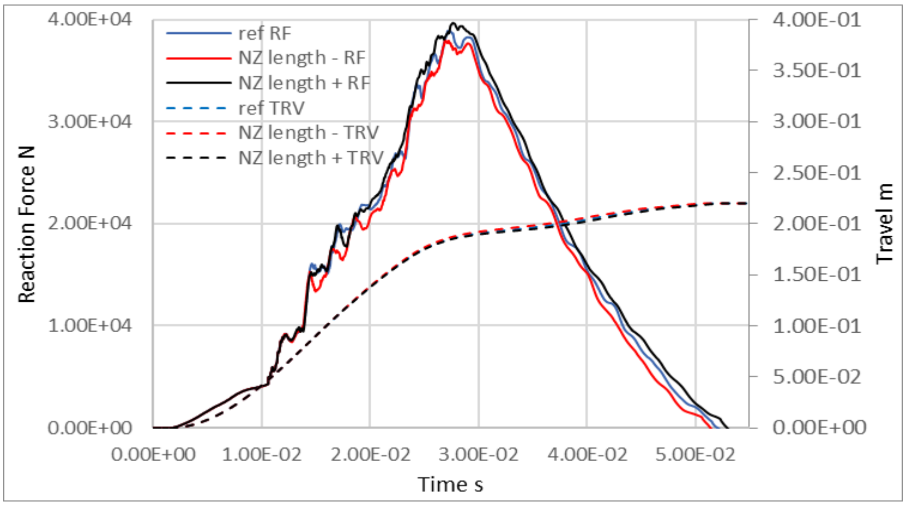

Figure 5.24 Reaction force and travel with the nozzle (NZ) flat throat lengthened (NZ +) and shortened (NZ -) by 15 mm.

The comparison reveals little difference between two cases both in terms of travel and reaction force. Up until current zero, the difference in travel between the two cases is 2.1 mm, with the short nozzle case (189.0 mm at current zero) pulling ahead of the long nozzle case (186.9 mm at current zero). Reaction force between the two cases differed by 2.6 kN at the peak, which is insignificant considering the peak values are well above

35 kN in both cases.

Variation in the length of the nozzle throat does not affect pressure build up at nozzle upstream in a significant way, and the reaction force remains close to each other in the two cases thought out the simulation. Figure 5.25 and Figure 5.26 give a broad picture of the upstream pressure distribution (monitor point 1 and 2) for both cases.

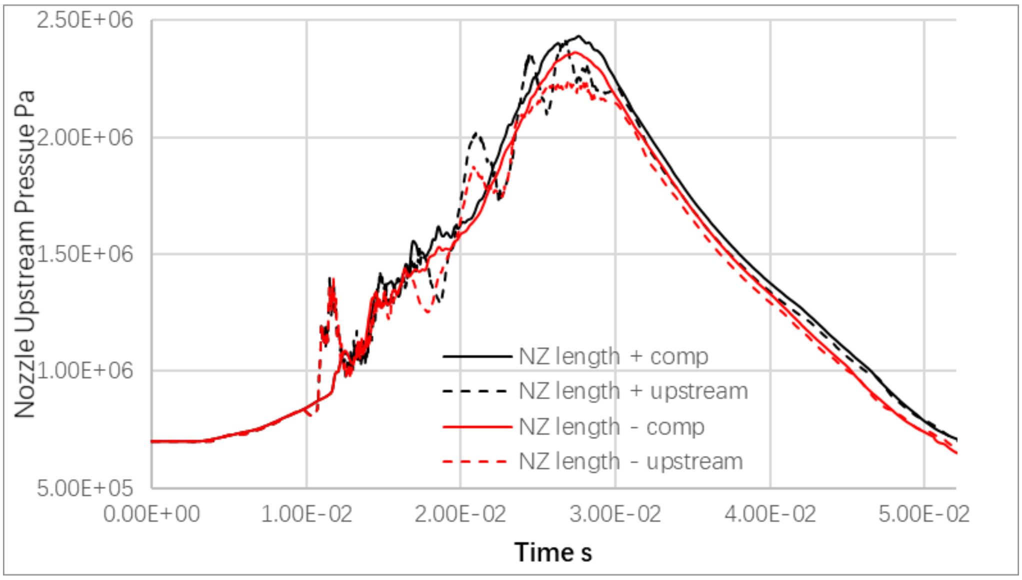

Figure 5.25 The pressure at nozzle upstream for both long and short nozzle cases.

Pressure recorded at monitor points 1 and 2 (Figure 5.25) show little difference between the two cases. However, at a location close to the arc (point 2), it can be seen that pressure fluctuations in the long nozzle case are stronger than the short nozzle case. This is again observed in Figure 5.26, in which temperature contours at t=21.0 ms for both cases are shown together with isobars showing the pressure in regions surrounding the arc. As in the long nozzle case, region immediately surrounding the arc has a relatively high pressure of 2.1 MPa whereas in the short nozzle case, the surrounding gas pressure is 1.9 MPa, also can be seen in Figure 5.26 is that due to a short nozzle, compared with the other case, the arc is allowed to expand in the radial direction sooner and the section of arc inside the nozzle assumes a thinner profile which allows a wider flow channel.

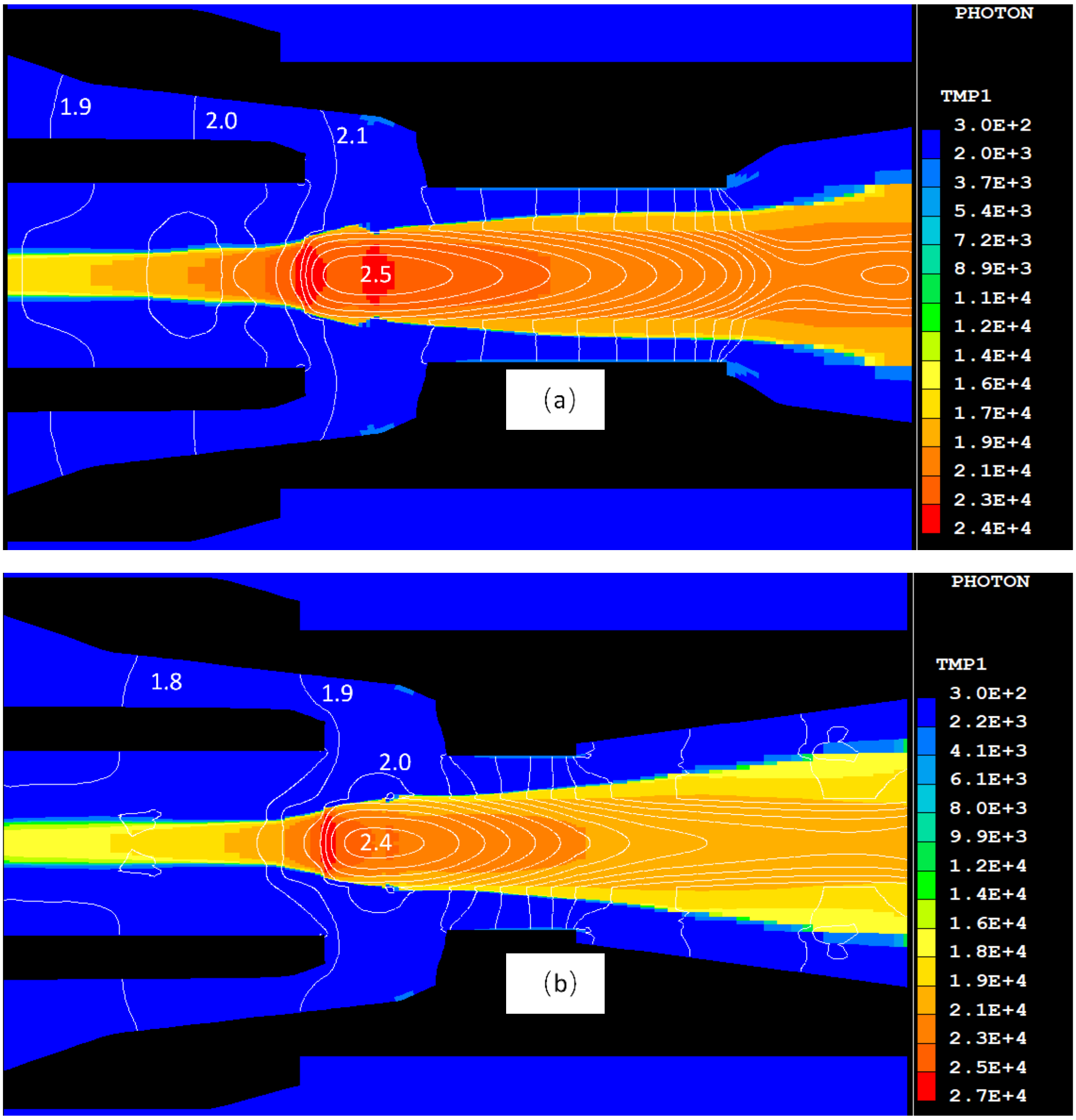

Figure 5.26 Temperature contour for the long (a) and short (b) nozzle cases at t=21.0 ms together with isobars spaced at 1 MPa.

Apart from the pressure difference at upstream, pressure in the nozzle throat is also affected by the length of the nozzle as shown Figure 5.27. Two peaks in pressure are visible at the throat. The first is caused by the contact blocking the nozzle. To demonstrate this, the exact moment when the downstream contact clears the nozzle throat in both cases are marked by dashed lines in Figure 5.27.

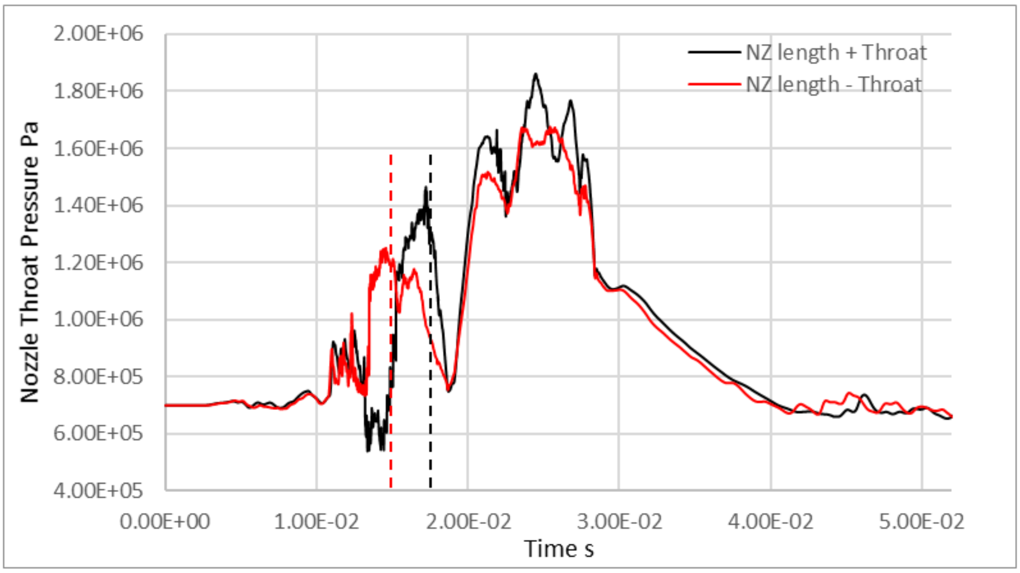

Figure 5.27 Pressure at nozzle throat for long and short nozzle cases. Dashed lines mark the moments when downstream contact clears the nozzle flat throat in each case.

The difference in nozzle length has led to the contact clearing the nozzle throat at different times in these cases. Thus, the first peak pressure appears at different times accordingly. The second peak pressure corresponds to the peak current (47 kA at t=23.5 ms) in the last half cycle, at which point a slightly higher pressure peak is recorded in the long nozzle case.

In terms of interruption capability, critical RRRV for the long nozzle case is 2.5 kV/µs while RRRV for the short nozzle case is 3.2 kV/µs. At current zero, although both cases have almost the same upstream and downstream pressure (on the axis) as shown in Figure 5.28 (a), a shorted nozzle led to a faster pressure drop along the axis. As a result, with a shorted nozzle, average axial velocity (Figure 5.28 (b)) in the nozzle is also considerably higher. In this way, a stronger axial flow which is more effective at carrying momentum and energy to the downstream is established in the short nozzle case. As shown in 0, both axial temperature (Figure 5.28 (c)) and conductivity (Figure 5.28 (d)) are lower in the nozzle section for the short nozzle case. This lead to the difference in critical RRRV observed in these two cases.

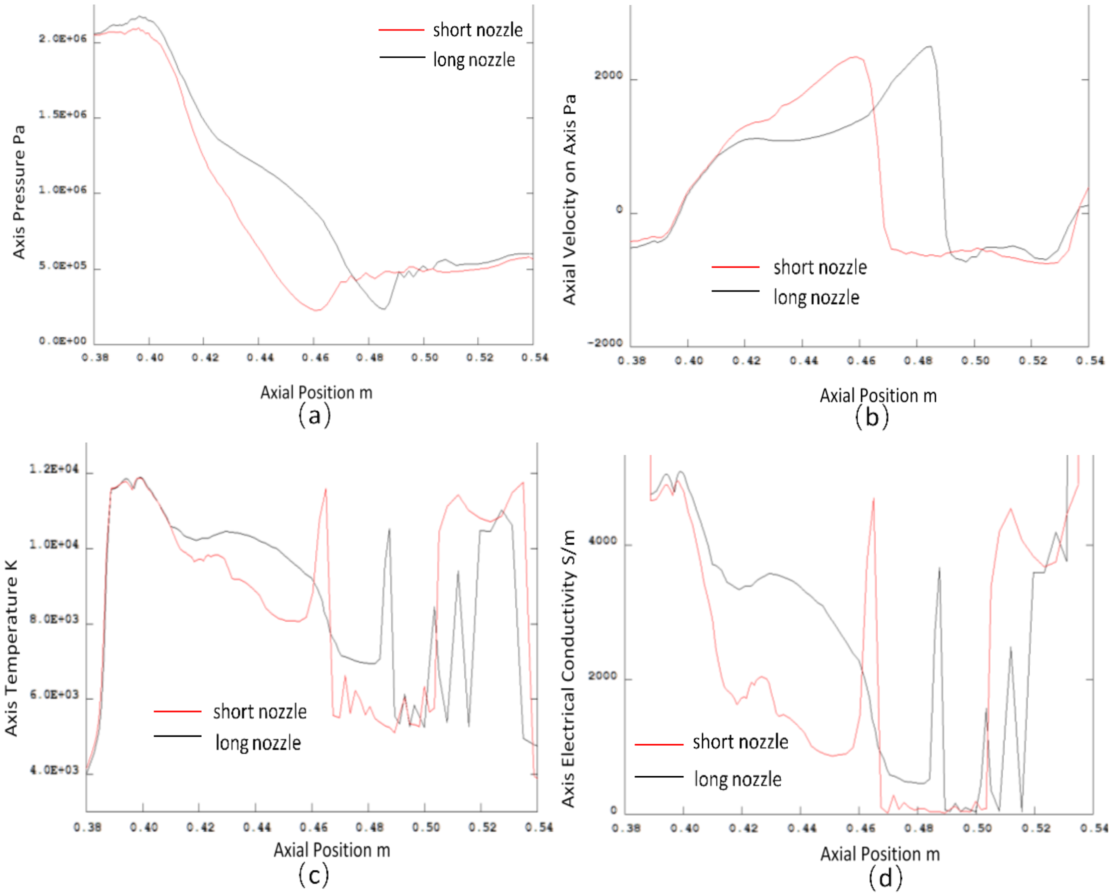

Figure 5.28 Axial pressure (a), velocity (b), temperature (c) and conductivity (d) for the long and short nozzle cases at current zero.

To conclude, the change in nozzle length has little impact on the pressure build up process at nozzle upstream. As a result, the two cases have similar total reaction force and contact travel. On the other hand, the length of the nozzle does impact the pressure discharge process. A short nozzle leads to a quicker discharge and ultimately a stronger axial flow in the nozzle flat throat which helps to create a favourable flow condition at current zero. As a result, the short nozzle case has a higher critical RRRV than the long nozzle case.

5.2.3.2 Nozzle throat radius

The change of nozzle length is illustrated in Figure 5.29. Two cases have been carried out with the nozzle radius increased 2 mm and also decreased by the same amount. The original radius of the nozzle is 15.5 mm. Apart from the nozzle radius, the rest of parameters (including arcing current) are kept identical to those in the 50 kA long arc duration case mentioned in Section 5.2.2. The travel and reaction force recorded in the 50 kA long arc duration case are used as references.

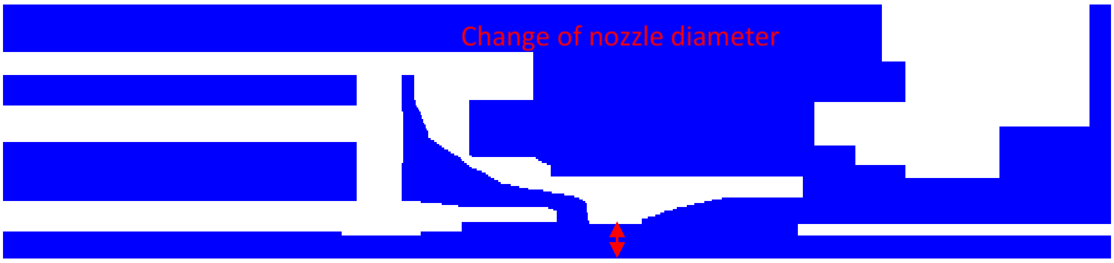

Figure 5.29 Demonstration of change of nozzle radius.

Travel together with reaction force obtained from both cases are presented in Figure 5.30.

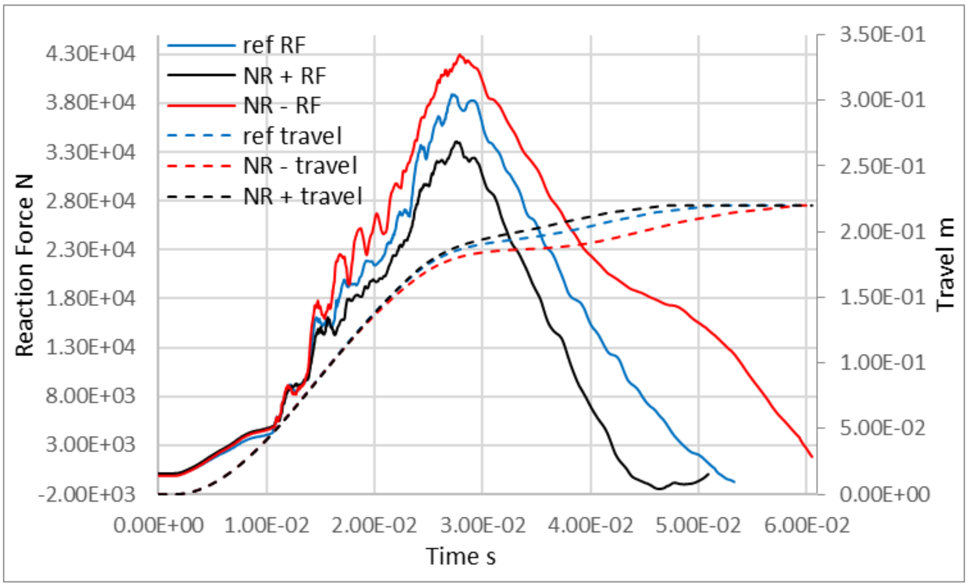

Figure 5.30 Travel and reaction force obtained with nozzle radius (NR) increased by 2 (NR+) mm as well as decreased 2 (NR -) mm.

As can be seen in Figure 5.30, increasing the nozzle radius results in a substantial decrease in total reaction force as vice versa. It is interesting to see that with a smaller nozzle radius, after achieving maximum reaction force, due to the slower pressure discharge process in the small nozzle radius case, the reaction force

In addition, the difference in reaction force has also led to a noticeable difference in travel. The difference in reaction force can be attributed to several aspects: Firstly, Figure 5.31 gives the comparison of pressure distribution inside the nozzle for both large (Figure 5.31 (a)) and small (Figure 5.31 (b)) nozzle radius at t=15.15 ms. 5000 and 18000 K isotherms are also given in the diagram to give a description of the shape of the arc at this instance. As can be seen in the case with small nozzle radius, marked by the 5000 K isotherm, a considerable amount of hot gas flows back into the compression chamber. Such phenomenon is not observed in the wide nozzle case.

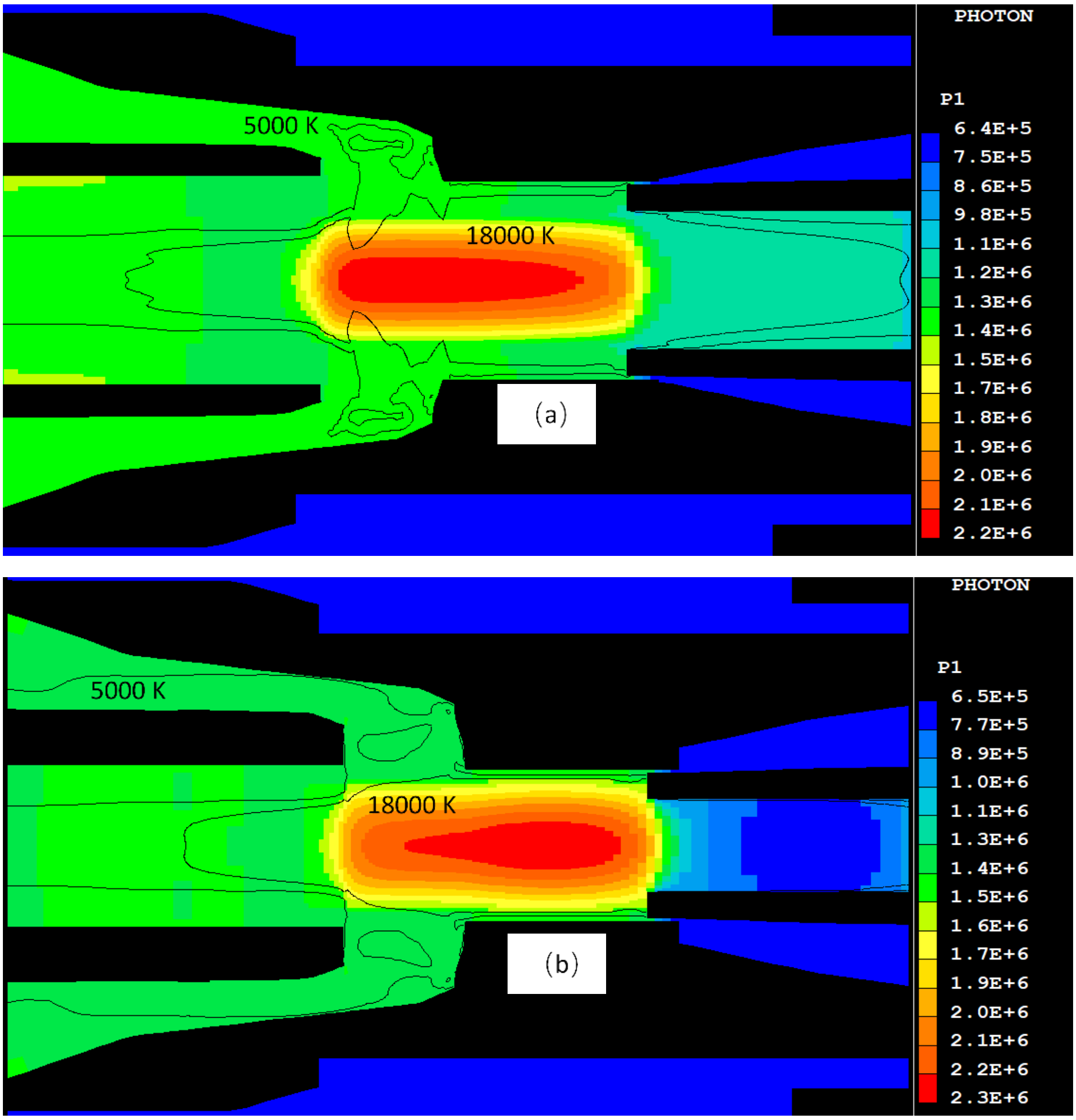

Figure 5.31 Pressure distribution in the nozzle for both wide (a) and narrow (b) nozzle cases at t=15.15 ms together with 5000 and 18000 K isotherms marking the shape of the arc and its surrounding flow.

Secondly, Figure 5.32 shows the comparison of pressure distribution inside the nozzle for both large (Figure 5.32 (a)) and small (Figure 5.32 (b)) nozzle radius at t=17.65 ms. 5000 and 20000 K isotherms are also given in the diagram to give a description of the shape of the arc at this instance. As can be seen in the diagram, a wider nozzle undoubtedly lead to a wide flow channel through which gas can be discharged from upstream to downstream more easily.

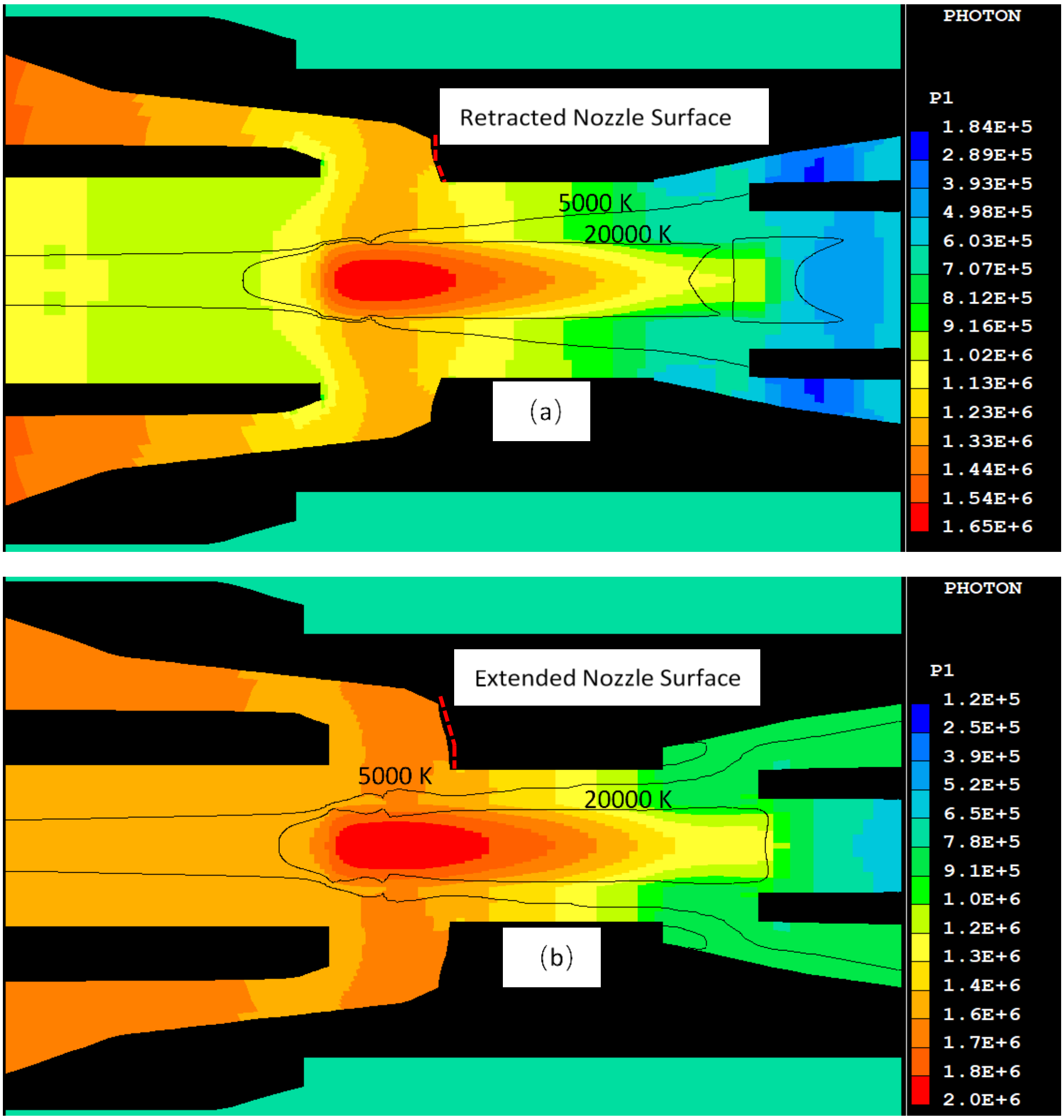

Figure 5.32 Pressure distribution in the nozzle for both wide (a) and narrow (b) nozzle cases at t=17.65 ms together with 5000 and 20000 K isotherms marking the shape of the arc and its surrounding flow.

Figure 5.33 gives the Mach number at a typical nozzle cross-section for both cases.

Clearly, with a larger nozzle radius, not only is the flow generally stronger in the axial direction, between the arc thermal boundary and the nozzle surface, a stronger external flow can be established.

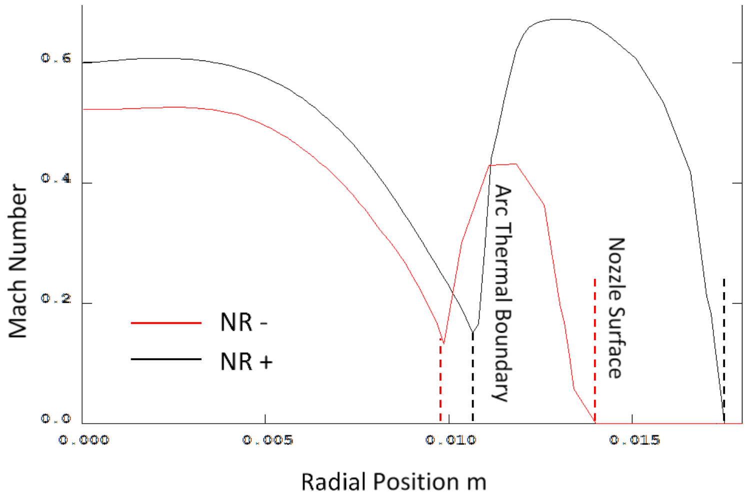

Figure 5.33 Mach number in the radial direction at a typical nozzle cross-section for both large and small nozzle radius at t=17.65 ms.

Together, as shown in Figure 5.34, these factors have resulted in a higher pressure at both compression chamber and nozzle throat in the small nozzle radius case.

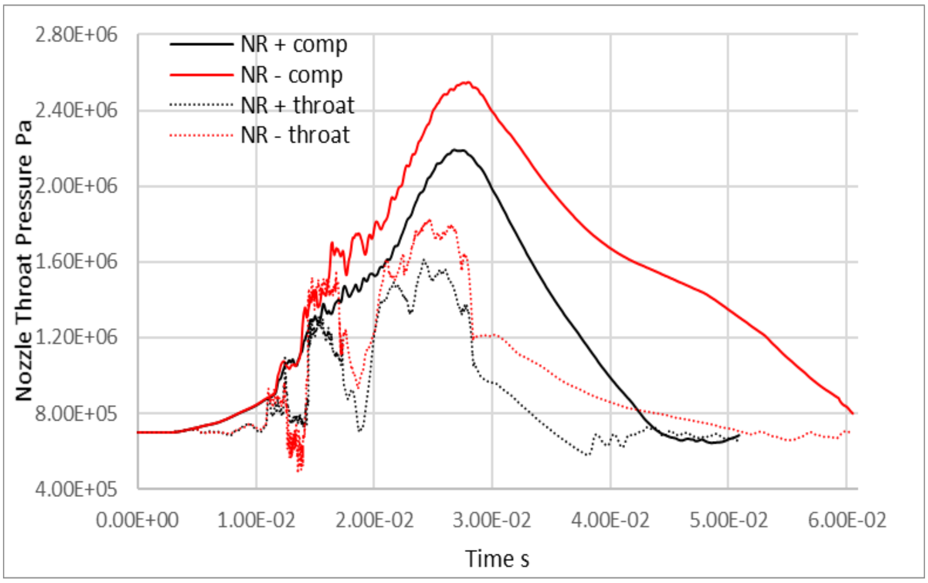

Figure 5.34 Pressure recorded in the compression chamber and at nozzle flat throat for both large and small nozzle radius cases.

One additional factor that contributes to the higher reaction force (Figure 5.30) in the small nozzle radius case is the fact that reducing the nozzle diameter while maintaining other structural parameters requires more solid surface being introduced into the computation domain. In other words, the surface must be extended in the negative radial direction, pushing the nozzle surface closer to the axis (marked by red dashed lines in Figure 5.29). In doing so, the area subjected to the high pressure region is effectively enlarged when radius nozzle is reduced. With a 2 mm decrease in nozzle radius, the increased area (on each side of the nozzle) can be calculated:

$$A_{increase} = \pi {r_{original}}^2 - \pi(r_{original} - \Delta r)^2 \tag{5.2}$$

Plug in the original nozzle radius (15.5 mm) and the change in nozzle radius (2 mm) the increase in nozzle surface area on one side of the nozzle is 182.21 mm^2. Similarly, with a 2 mm increase in nozzle radius, area subtracted from the original nozzle surface area is:

$$A_{decrease} = \pi(r_{original} + \Delta r)^2 - \pi {r_{original}}^2 \tag{5.3}$$

which is calculated to be 207.34 mm^2. In total, the difference in nozzle surface area between the two cases is 389.55 mm^2. To perform a simple estimation, at t=16.75 ms, assuming this area is subjected to a uniform pressure of 1.62 MPa (average of the two case) and on the other side of the nozzle, the same amount of surface is subjected to a uniform pressure of 0.80 MPa (average of the two cases, close to filling pressure), the net force exerted on the nozzle due to this newly introduced additional surface area is roughly 311.64 N. Compared with the difference of reaction force at this instance (instantaneous reaction force is 17.9 kN and 19.5 kN for the large and small nozzle radius cases respectively, the difference is hence 1.6 kN), the difference of reaction force caused by varying nozzle surface area amounts to 19.5% of the total difference. Although a fairly rough estimation, this proves indicates that the difference in reaction force between the two cases is mainly caused by the different flow field resulted from change in the shape of the nozzle rather than the additional area introduced by reducing the nozzle radius.

Critical RRRV recorded for the small nozzle radius case is 3.3 kV/μs, an improvement from the 3.0 kV/μs recorded in the reference case while the critical RRRV for the large nozzle case deteriorates to 2.4 kV/μs. With a higher recorded reaction force, in the small nozzle radius case, distance travelled until current zero is 181.63 mm, 8.67 mm shorter compared with the 190.30 mm distance with a large nozzle radius. Despite the shorter contact gap having an adverse effect on the critical RRRV, with a small nozzle radius, the critical RRRV is increased when compared to the reference case. This can be explained by examining the flow field in both cases at current zero. Figure 5.35 shows the pressure distribution as well as axial velocity on the axis for both cases at current zero.

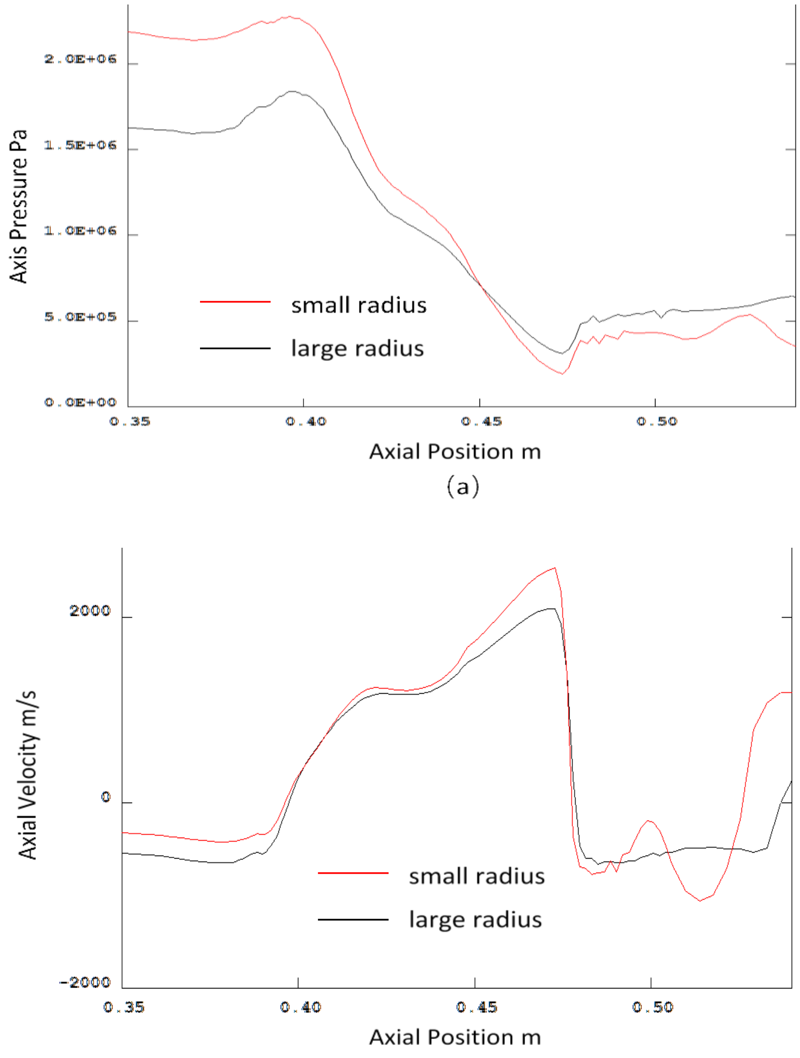

(a)

(b)

Figure 5.35 Pressure (a) and velocity (b) (axial component) on the axis at current zero.

With a smaller nozzle radius, a clear disparity in upstream pressure can be observed. Consequently, the axial velocity component in the small nozzle radius case is higher than the large nozzle radius case, the difference is most prominent towards the end of nozzle flat throat. Similar to the conclusion drawn in the nozzle throat length study, a stronger axial flow in this case also enhances the energy and momentum transfer in the arcing space thus effectively limiting the residual temperature within the gap.

5.3 Conclusion

The coupled circuit breaker model has been used to study a 252 kV puffer circuit breaker (coupled with a ZF-11-252 (L)/CYTA hydraulic driving mechanism, details in Chapter 3) under various arcing conditions as well as with different nozzle geometries. The studies indicate that:

a) Even in the 10 kA case where reaction force is relatively small, the maximum predicted reaction force managed to exceed 25 kN, which is comparable to the maximum driving force the driving mechanism can provide (36 kN). Near the beginning of the travel (usually the first 10 or 15 ms), the magnitude of the reaction force is insignificant when compared to the driving force. As a result, even if other conditions cause the reaction force to vary, no significant change in travel was observed in any cases. This is because the peak driving force is achieved very quickly, usually just several milliseconds from the start of the simulation while the reaction force is related to the pressure build-up process in the arc chamber. However, when the reaction force rises to a similar magnitude as positive driving force (total driving force take away reaction force), the change in arcing conditions and nozzle geometries come into play. A difference in reaction force at this stage could potentially lead to very different travel characteristics.

b) In the current level comparison (10 kA and 50 kA), the 50 kA case has seen significantly higher reaction force than the 10 kA case. This is the result of much higher energy input in the 50 kA. The 50 kA case has a higher critical RRRV (3.0 kV/μs) than the 10 kA case (2.2 kV/μs) despite having a much higher axial temperature at current zero. The superior critical RRRV in the 50 kA cases can be attributed to a higher axial pressure and a longer contact gap.

c) In the arc duration comparison ((17.72 ms for long, 15.72 ms for medium and 13.72 ms for short arc duration), the difference in arc duration was created by shifting the current waveform. Therefore, the value of the peak current is the same for all three cases. With a 2 ms difference in arc duration, all three cases recorded very similar reaction forces and travels. The initial discrepancy in reaction force between all three cases was caused by the difference in instantaneous current. It has also been found that a shorter arc duration tends to reduce the critical RRRV, with both medium and short arc duration cases having a critical RRRV of 2.7 kV/μs. The longer arc duration has resulted in a higher axial pressure at current zero as well as a longer contact gap. The combination of these two factors is responsible for the difference in critical RRRV between the long duration and other cases.

d) Chang in length of the nozzle throat has no obvious effect on both reaction force and travel. Therefore, length of the contact gap at current zero in both cases is almost identical. However, the critical RRRV for short nozzle (3.2 kV/μs) is higher than the long nozzle (2.5 kV/μs). Considering the nozzle upstream pressure in both cases at current zero is similar, a shorter nozzle creates a stronger axial flow in the nozzle. The section of the arc with in the nozzle is more sufficiently cooled in the short nozzle case, thus the axial temperature and conductivity are lower. This is likely the cause of the short nozzle case having a higher critical RRRV.

e) Change in the nozzle throat radius has a great impact on the overall pressure distribution in the arc chamber. Consequently, the recorded reaction force and travel show a visible difference between the large and small nozzle radius cases. Enlarging the nozzle limits the pressure build-up at nozzle upstream and leads to a lower overall reaction force and faster travel.

Chapter 6 Conclusion and Future Work

6.1 Major Contributions and Conclusion

The major achievements of this research project regarding coupled circuit breaker simulation are listed below:

a) A mathematical model which describes the opening operation of a hydraulic driving mechanism was established. Important hydraulic components including the control valves (pilot and main valves) and the main hydraulic cylinder are all considered in the mathematical model. The model developed was capable of predicting the dynamic behaviour (piston travel, speed and pressure change in the cylinder) of the driving mechanism during circuit breaker opening operations. Based on the developed model, sensitivity studies have also been conducted and the key parameters that play important roles in defining the dynamic characteristics of the driving mechanism were identified.

b) Based on the grid structure in PHOENICS and the geometrical feature of the circuit breaker arc chamber, an integral method was developed to calculate the reaction force imposed by high pressure gas in the arc chamber. This method relies on the Liverpool arc model to provide prediction of pressure distribution in the arc chamber and is integrated into the Liverpool arc model as a subroutine.

c) A dedicated solver for the hydraulic driving mechanism governing equations was developed. The solver utilizes the four-order Runge-Kutta method to solve the governing equations iteratively and is coded in C++ to take advantage of open source resources.

d) An interface between the arc model solver (the arc model was implemented in PHOENICS) and the driving mechanism solver (coded in C++) which facilitates information exchange in a coupled circuit breaker simulation was also developed.

e) Results obtained in coupled simulations and measurements were studied and compared. Based on the comparative studies, two calibration tests have been performed. The main source of inaccuracy within the driving mechanism model was identified as the frictional coefficient of the piston inside the main hydraulic cylinder, a modified frictional coefficient which accounts for all sources of frictions has been introduced and its value calibrated based on measured travel. Another new coefficient has also been introduced to account for the inaccuracy in the predicted arc chamber pressure distribution under high current conditions.

f) The coupled circuit breaker model was used in a number of simulation cases to study the change in reaction force with regard to different arcing conditions and nozzle geometries. Furthermore, in these cases, the interruption capability (in terms of RRRV) of the circuit breaker under study were recorded and analyzed.

With a newly designed solver and interface included, the coupled circuit breaker model successfully incorporates the driving mechanism into the existing Liverpool arc model. With this accomplishment, instead of a pre-defined travel profile, the true dynamic motion characteristics of the moving components can be reflected in future circuit breaker simulations (based on the coupled circuit breaker model). The reaction force, an important parameter involved in the interaction between the arc and the driving mechanism, can be taken into consideration during the design and optimization process of prototype driving mechanisms and interrupters. In this way, effectiveness and usefulness of the Liverpool arc mode can be fully exploited.

In the sensitivity study presented in Chapter 3, it has been found that the system is most sensitive to any changes in system pressure and piston rod side area while any change in the load mass can also impact the dynamic characteristics of the system considerably. On the other hand, other parameters that are not related (although the load can be considered external, it is connected to the piston via a linkage system, thus considered as related to the cylinder) to the main hydraulic cylinder (such as those related to the main valve and pilot valve, despite having no significant impact on the cylinder) have little impact on the behaviour of the main hydraulic cylinder. This indicates that the difference in flow rate between different levels of components (in this sense, a tiered control hierarchy, for example the pilot valve can be considered as controlling the operation of the main valve, thus being a level below) are too large for change in these parameters to be noticed (in the piston travel and speed). Consequently, any attempt to modify the dynamic behaviour of the system should be focused on the main hydraulic cylinder.

The calibration tests in Chapter 4 have proven that even when the current is relatively low (10 kA), the reaction force still has a visible impact on the travel profile (refer to Figure 4.17). Further studies in Chapter 5 showed that the reaction force has a comparable magnitude to that of the positive driving force provided by the driving mechanism. It is because the peak driving force and reaction force occurred at different stages in the simulation that initially the impact of reaction force on the travel characteristics are small and can be ignored. However, when the pressure at nozzle upstream reaches its peak, the reaction force is also at its maximum. It is at this stage, any factor that alters the reaction force will also in turn affect the travel characteristics and ultimately, the length of contact gap at current zero.

It has also been confirmed in Chapter 5 that the arc duration and current level will affect the pressure build-up process in the arc chamber. In general, longer arc duration and higher current level could lead to higher reaction force (albeit through different mechanisms). However, this does not necessarily indicate an inferior critical RRRV compared with short arc duration and low current level situations. The problem is of a complicated nature and the combined effect of both factors should be examined carefully. On the other hand, in terms of nozzle geometry, lengthening the nozzle flat throat has little impact on the overall reaction force, the same can be said for shortening the nozzle throat. The section of the arc with in the nozzle is more sufficiently cooled in the short nozzle case, thus the axial temperature and conductivity are lower contributing towards a higher critical RRRV. Change in the nozzle throat radius has a great impact on the overall pressure distribution in the arc chamber. Although having a higher overall reaction force, with a smaller nozzle radius, a higher critical RRRV (compared with large nozzle radius) is observed.

6.2 Future Works

The future works regarding this research project can be divided into two main sections. Further improvement on the coupled circuit breaker model and its universal applicability could be valuable future work topics. In the meantime, with the current coupled model, study regarding the interaction between the arc and driving mechanism can be expanded to include more design parameters and arcing conditions.

6.2.1 Further improvements on the coupled circuit breaker model

Improvement of the coupled circuit breaker model can be looked at from multiple different perspectives. Firstly, due to the complexity of the device itself and limited time and computational resources, an empirical coefficient was used in the driving mechanism model to model the frictional force on the cylinder level. Further investigation into the matter is needed. A model which is accurate and based on the fundamental processes involved in the friction between different components and fluid can potentially be established. Such model could be applied to other driving mechanisms (with different design parameters) without the need of calibration. Secondly, it has been noticed in Chapter 4 (see Figure 4.11) that the arc model has the tendency to under-predict arc chamber pressure under high current conditions. It has been theorized that the cause of this discrepancy is due to ablation-induced nozzle enlargement and inaccuracies embedded in PTFE mass flow rate prediction. If all factors related to this discrepancy mentioned in Chapter 4 can be incorporated into the arc model, it would eliminate the need to perform the second calibration test and increase the accuracy of the coupled model on a fundamental level. Thirdly, at the moment, parameters regarding the driving mechanism model were provided to the simulation via user-defined files. This approach is not intuitive and requires the user to be familiar with the system. A user-friendly interface could improve the user experience with the coupled circuit breaker modelling platform (which is based on the coupled circuit breaker model).

6.2.2 More research topics

With the current coupled circuit breaker, more researches can be done to provide additional information that could be used in circuit breaker design. For example, the reaction force can be calculated under more current levels. Ideally, a threshold value can be found beyond which the reaction force will have a large enough impact on the travel, so it cannot be ignored. To further this work, several tasks need to be completed:

a) A consensus with design engineers has to be reached, so a certain level of deviation from the standard measured no-load travel (used as a reference) can be considered as the threshold.
b) An interval with which the arcing current is changed has to be decided, an optimum choice will both save computational time and, in the meantime, preserve enough resolution of subtle changes in travel and reaction force can still be spotted.
c) Simulations with different arcing current levels has to be performed and results analyzed.
d) In the case that no such threshold can be found, the correlation between current level, travel characteristics and the performance of the breaker can still be studied.

Furthermore, with CO_2 mixture being used as arc quenching medium in newly design circuit breakers, it is necessary to examine how pressure rise in the arc chamber could affect the travel characteristics with the introduction of these new gases, and ultimately, how this relates to the performance of the circuit breaker:

a) In order to perform simulation with a different arc quenching medium, its material properties such as electrical and thermal conductivity, has to be obtained before the simulation can be started. Normally, this can be done through calculation and then, ideally, the result should be verified by experiment.
b) Once the material properties of the new gas are obtained, it is necessary to decide which parameters to record during the simulation. As the most important information in the pressure build-up process in the arc chamber, so we also need to determine at which locations pressure should be monitored.

c) The arcing process must be studied thoroughly so the key parameters of the new gas that causes the pressure build-up process to be different from that of the SF_6 can be identified.

d) This process can be repeated for different gases.

References

[1] MacLeay I, “60th Anniversary: Digest of United Kingdom Energy Statistics”, *The Stationery Office*, 2009

[2] Andersson G, Donalek P, Farmer R, Hatziargyriou N, Kamwa I, Kundur P, Martins N, Paserba J, Pourbeik P, Sanchez-Gasca J and Schulz R, “Causes of the 2003 Major Grid Blackouts in North America and Europe, and Recommended Means to Improve System Dynamic Performance”, *IEEE Transactions on Power Systems*, Vol. 20, pp. 1922-1928, 2005

[3] Blower R W, “Distribution Switchgear”, *London Collins*, 1986

[4] Ryan H M, “High Voltage Engineering and Testing”, *IET*, 1994

[5] Garzon R D, “High Voltage Circuit Breakers: Design and Applications”, *CRC Press*, 2002

[6] NIAYESH K, “Power Switching Components: Theory, Applications and Future Trends”, *Cham Switzerland Springer*, 2017

[7] “Breakers AL. Application Guide”, *Zürich Switzerland ABB*, 2009

[8] IEC 62271-100, “High Voltage Switchgear and Control Gear Part 100: Alternating Current Circuit Breakers”, 2012

[9] Trencham H, “Circuit Breaking”, *Butterworths Scientific Publications*, 1953

[10] Flurscheim C H, “Power Circuit Breaker Theory and Design”, *IET*, 1982

[11] Saxena S, Ali M, Singh A and Gandhi K, “Various Types of Circuit Breakers Used in Power System for Smooth Working of the Transmission Line”, *MIT International Journal of Electrical and Instrumentation*, Vol. 2, pp. 106-111, 2012

[12] Nakanishi K, “Switching Phenomena in High-voltage Circuit Breakers", 1991

[13] Jones G R and Fang M T C, “The Physics of High-power Arcs”, *Reports on progress in physics*, Vol. 43, pp.1415, 1980

[14] Kutnjak Z, Rožič B, Pirc R and Webster J G. “Wiley Encyclopedia of Electrical and Electronics Engineering”, *John Wiley & Sons*, 2015

[15] Haddad A and Doug F W, “Advances in High Voltage Engineering”, *IET*, Vol. 40, 2004

[16] Stewart S, “Distribution Switchgear”, *IET*, Vol. 46, 2004

[17] Yan J D, Fang M T C and Hall W, “The Development of PC Based CAD Tools for Auto-expansion Circuit Breaker Design”, *IEEE Transactions on Power Delivery*, Vol. 14, pp. 176-181, 1999

[18] Fletcher P L and W Degen, “A Summary of the Final Results and Conclusions of the Second International Enquiry on the Reliability of High Voltage Circuit-Breakers”, *IET*, pp. 24-30, 1995

[19] Heinemann L and Chi H X “Technology Benchmark of Operating Mechanisms for High Voltage Switchgear”, *ABB AG Mannheim Germany*, 2011

[20] Liu W, Xu B, Yang H, Zhao H and Wu J, “Hydraulic Operating Mechanisms for High Voltage Circuit Breakers: Progress Evolution and Future Trends”, *Science China Technological Sciences*, Vol. 54, pp. 116-125, 2011

[21] Doddannavar R, Barnard A and Ganesh J, “Practical Hydraulic Systems: Operation and Troubleshooting for Engineers and Technicians”, *Newnes*, 2005

[22] Indragandhi V, Kumar L A and Vishnumoorthy K, “Methods of Operating Mechanisms of High Voltage Circuit Breakers: An Overview”, *2017 International Conference, IEEE*, 2017

[23] Harald F, “High Voltage Circuit Breakers: Trends and Recent Developments”, *Erlangen Germany Siemens*, 2011

[24] Jiuming X, Dengyue S, Weiguo X, Dezhi W and Shanzhong D, “Optimization Design for the Over-travel Rod Spring of the Vacuum Circuit Breaker through the Improved Genetic Algorithm”, *Journal of Chemical and Pharmaceutical Research*, Vol. 6, pp. 602-611, 2014

[25] Bizjak G, Zunko P, Povh D, “Circuit Breaker Model for Digital Simulation Based on Mayr's and Cassie's Differential Arc Equations”, *IEEE Transactions on Power Delivery*, Vol. 10, pp.1310-1315, 1995

[26] Rong M, Yang F, Wu Y, Murphy A B, Wang W, and Guo J, “Simulation of Arc Characteristics in Miniature Circuit Breaker”, *IEEE Transactions on Plasma*

Science, Vol. 38, pp.2306-2311, 2010

[27] Trepanier J Y, Zhang X D, Pellegrin H, and Camarero R, "Application of Computational Fluid Dynamics Tools to Circuit Breaker Flow Analysis", *IEEE transactions on power delivery*, Vol. 10, pp.817-823, 1995

[28] Reichert F, Petchanka A, Freton P and Gonzalez J J, "Modelling and Simulation of SF_6 High Voltage Circuit Breakers: An Overview on Basics and Application of CFD Arc Simulation Tools", *Plasma Physics and Technology,* Vol. 4, pp. 213-224, 2017

[29] Shimmin D W, Jones G R and Ali S M, "Transient Pressure Variations in SF6 Puffer Circuit Breakers", *Journal of Physics D: Applied Physics,* Vol. 23, pp. 533, 1990

[30] Seeger M, Tepper J, Christen T and Abrahamson J, "Experimental Study on PTFE Ablation in High Voltage Circuit Breakers", *Journal of Physics D: Applied Physics*, Vol. 39, pp. 5016, 2006

[31] Tanaka Y, Yamachi N, Matsumoto S, Kaneko S, Okabe S and Shibuya M, "Thermodynamic and Transport Properties of CO_2, CO_2-O_2, and CO_2-H_2 Mixtures at Temperatures of 300 to 30,000 K and Pressures of 0.1 to 10 MPa", *Electrical Engineering in Japan*, Vol. 163, pp. 18-29, 2008

[32] Kieffel Y, Biquez F and Ponchon P, "Alternative Gas to SF_6 for Use in High Voltage Switchgears: g3", *CIRED Paper,* Vol.230, 2015

[33] Lee Y S, Ahn H S, Park S W and Lee J H, "Coupled Simulation of Gas Flow and Dynamic Analysis for Stroke Calculation in Circuit Breaker", *Electric Power Equipment-Switching Technology (ICEPE-ST)*, pp. 203-206, 2011

[34] Xu B, Ding R, Zhang J, Sha L and Cheng M, "Multiphysics-coupled Modeling: Simulation of the Hydraulic Operating Mechanism for a SF_6 High-voltage Circuit Breaker", *IEEE/ASME Transactions on Mechatronics*, Vol. 21, pp. 379-393, 2016

[35] Lee Y S, Bang B H, Ahn H S, Choi J U and Park SW, "Coupled Simulation of Flow and Dynamic Analysis for Prediction of the Performance in GIS", *Electric Power Equipment-Switching Technology (ICEPE-ST)*, pp. 1-4, 2013.

[36] Chen X, Ma Z and Siarry P, "Theoretical and Experimental Study on the Opening

Characteristic of Puffer Circuit Breakers", *IEE Proceedings-Electric Power Applications*, Vol. 147, pp. 141-145, 2000

[37] Ruchti C B and Niemeyer L, "Ablation Controlled Arcs", *IEEE Transactions on Plasma Science,* Vol. 14, pp. 423-434, 1986

[38] Rieder W, "Circuit breakers Physical and Engineering Problems I Fundamentals", *IEEE Spectrum*, Vol. 7, pp. 35-43, 1970

[39] Gross B, Grycz B and Miklossy K, "Plasma Technology", *London Iliffe Books*, 1968

[40] Kunkel W B, "Plasma Physics in Theory and Application", *McGraw-Hill New York*, 1966

[41] Pei Y Q, "Computer Simulation of Fundamental Processes in High Voltage Circuit Breakers Based on an Automated Modelling Platform", *PhD Thesis*, *University of Liverpool*, 2014

[42] Boulos M I, Fauchais P and Pfender E, "Thermal Plasmas: Fundamentals and Applications", *Springer Science & Business Media*, 2013

[43] Fang M T C and Lin W Y, "Current Zero Behavior of a Gas-blast Arc. Part 1: Nitrogen", *IEE Proceedings A (Physical Science, Measurement and Instrumentation, Management and Education)*, Vol. 137, pp. 175-183, 1990

[44] Tanaka Y, Nakano T, Hao S, Tomita K, Inada Y, Kumada A, Hidaka K, Fujino T, Suzuki K and Shinkai T, "Fundamental Studies on Switching Arcs-Experimental and Numerical Approaches", *Electric Power Equipment-Switching Technology (ICEPE-ST)*, pp. 1-10, 2017

[45] Zhang J F and Fang M T C, "A Comparative Study of SF_6 and N_2 arcs in Accelerating Flow", *Journal of Physics D: Applied Physics*, Vol. 21, pp. 730, 1988

[46] Lewis E, "Current Zero Spectroscopy of a High Power SF_6 Circuit Breaker Arc", *Gas Discharges and Their Applications 1985,* pp. 31-34, 1985

[47] Griem H R, "Plasma Spectroscopy", *McGraw Hill New York*, 1964

[48] Hinz K P, "Optical Diagnostics of SF_6 High-current Discharges", *Journal of Physics D: Applied Physics*, Vol. 19, pp. 2381, 1986

[49] Ahmethodzic A, Kapetanovic M, Sokolija K, Smeets R P and Kertész V, "Linking

a Physical Arc Model with a Black Box Arc Model and Verification", *IEEE Transactions on Dielectrics and Electrical Insulation*, Vol. 18, 2011

[50] Gustavsson N, "Valuation and Simulation of Black-box Arc Models for High-Voltage Circuit-Breakers", *Thesis*, 2004

[51] Smeets R P and Kertesz V, "Evaluation of High-voltage Circuit Breaker Performance with a New Validated Arc Model", *IEE Proceedings-Generation, Transmission and Distribution*, Vol. 147, pp. 121-125, 2000

[52] Cassie A M, "Arc Rupture and Circuit Severity; A New Theory", *CIGRE Paper 102*, pp. 1-14, 1939

[53] Mayr O, "Contribution to the Theory of Static and Dynamic Arcs", *Arch Elektrotech*, Vol. 37, pp. 588-608, 1943

[54] Skifstad J G and Murthy S N, "Analysis of Arc-heating Phenomena in a Tube", *IEEE Transactions on Nuclear Science*, Vol. 11, pp. 92-103, 1964

[55] Schlichting H, Gersten K, Krause E, Oertel H and Mayes K, "Boundary-layer Theory", *McGraw Hill New York*, 1955

[56] Swanson B W and Roidt R M, "Boundary Layer Analysis of an SF_6 Circuit Breaker Arc", *IEEE Transactions on Power Apparatus and Systems*, Vol. 3, pp. 1086-1093, 1971

[57] Chan S K, Fang M T C and Cowley M D, "The DC Arc in a Supersonic Nozzle Flow", *IEEE Transactions on Plasma Science,* Vol. 6, pp. 394-405, 1978

[58] Lowke J J and Ludwig H C, "A Simple Model for High Current Arcs Stabilized by Forced Convection", *Journal of Applied Physics*, Vol. 46, pp. 3352-3360, 1975

[59] Cowley M D, "Integrated Methods of Analyzing Electric Arcs: I. Formulation", *Journal of Physics D: Applied Physics*, Vol. 7, pp. 2218-2231, 1974

[60] Chan S K, Cowley M D and Fang M T C, "Integral Methods of Analyzing Electric Arcs: III Shape Factor Correlation for Low Radiation and Laminar Flow", *Journal of Physics D: Applied Physics*, Vol. 9, pp. 1085, 1976.

[61] Fang M T C and Brannen D A, "Current-zero Arc Model Based on Forced Convection", *IEEE Transactions on Plasma Science,* Vol. 7, pp. 219-219, 1979

[62] Hermann W, Kogelschatz U, Niemeyer L, Ragaller K and Schade E, "Investigation

on the Physical Phenomena Around Current Zero in HV Gas Blast Breakers", *IEEE Transactions on Power Apparatus and Systems,* Vol. 95, pp. 1165-1176, 1976

[63] Hermann W, Kogelschatz U, Niemeyer L, Ragaller K and Schade E, "Experimental and Theoretical Study of a Stationary High-current Arc in a Supersonic Nozzle Flow", *Journal of Physics D: Applied Physics*, Vol. 7, pp. 1703, 1974

[64] Ragaller K, Egli W and Brand K P, "Dielectric Recovery of an Axially Blown SF_6 Arc after Current Zero Part II: Theoretical Investigations", *IEEE Transactions on Plasma Science*, Vol. 10, pp. 154-162, 1982

[65] Schade E and Ragaller K, "Dielectric Recovery of an Axially Blown SF_6 Arc after Current Zero Part I: Experimental Investigations", *IEEE Transactions on Plasma Science*, Vol. 10, pp. 141-153, 1982

[66] Fang M T C and Zhuang Q, "Current-zero Behavior of an SF_6 Gas-blast Arc I: Laminar Flow. *Journal of Physics D: Applied Physics*, Vol. 25, pp. 1197, 1992

[67] Fang M T C, Zhuang Q and Guo X J, "Current-zero Behavior of an SF_6 Gas-blast Arc II: Turbulent Flow", *Journal of Physics D: Applied Physics,* Vol. 27, pp. 74, 1994

[68] Ernst K A, Kopainsky J G and Maeher H H, "The Energy Transport Including Emission and Absorption in N_2 Arcs of Different Radii", *IEEE Trans*, Vol. PS-1, pp. 3, 1973

[69] Chen Y S and Kim S W, "Computation of Turbulent Flows Using an Extended k-epsilon Turbulence Closure Model", 1987

[70] Launder B E and Spalding D B, "The Numerical Computation of Turbulent Flows", *Numerical Prediction of Flow Heat Transfer Turbulence and Combustion*, pp. 96-116, 1983

[71] Yakhot V S, Orszag S A, Thangam S, Gatski T B and Speziale C G, "Development of Turbulence Models for Shear Flows by a Double Expansion Technique", *Physics of Fluids A: Fluid Dynamics*, Vol. 4, pp. 1510-1520, 1992

[72] Yan J D, Nuttall K I and Fang M T C, "A Comparative Study of Turbulence Models for SF_6 Arcs in a Supersonic Nozzle", *Journal of Physics D: Applied Physics*, Vol.

32, pp. 1401, 1999

[73] Hermann W, Kogelschatz U, Ragaller K and Schade E, "Investigation of a Cylindrical Axially Blown High-pressure Arc", *Journal of Physics D: Applied Physics*, Vol. 7, pp.607, 1974

[74] Lowke J J and Liebermann R W, "Predicted Arc Properties in Sulfur hexafluoride", *Journal of Applied Physics,* Vol. 42, pp. 3532-3539, 1971

[75] Zhang J F, Fang M T C and Newland D B, "Theoretical Investigation of a 2 kA DC Nitrogen Arc in a Supersonic Nozzle", *Journal of Physics D: Applied Physics*, Vol. 20, pp. 368, 1987

[76] Zhang J L, Yan J D, Murphy A B, Hall W and Fang M T C, "Computational Investigation of Arc Behavior in an Auto-expansion Circuit Breaker Contaminated by Ablated Nozzle Vapor", *IEEE Transactions on plasma science*, Vol. 30, pp. 706-719, 2002

[77] Fang M T C, Kwan S and Hall W, "Arc-shock interaction inside a supersonic nozzle", *IEEE transactions on plasma science*, Vol. 24, pp. 85-86, 1996

[78] Zhang Q, Yan J D and Fang M T C, "Current Zero Behaviour of an SF_6 Nozzle Arc under Shock Conditions", *Journal of Physics D: Applied Physics*, Vol. 46, 2013

[79] Shayler P J and Fang M T C, "Radiation Transport in Wall-stabilised Nitrogen Arcs", *Journal of Physics D: Applied Physics,* Vol. 11, pp. 1743, 1978

[80] Liebermann R W and Lowke J J, "Radiation Emission Coefficients for Sulfur-hexafluoride Arc Plasmas", *Journal of quantitative spectroscopy and radiative transfer*, Vol. 16, pp. 253-264, 1976

[81] Fang M T C, Yan J D, Kwan S and Hall R, "Application of CFD Packages for the Simulation of Gas Blast Arcs", *XII International Symposium on Physics of Switching Arc*, Brno: Local Organization Committee, Vol. 2, pp. 13-22, 1996

[82] Hermann W and Schade E, "Radiative Energy Balance in Cylindrical Nitrogen Arcs", *Journal of Quantitative Spectroscopy and Radiative Transfer*, Vol. 12, pp. 1257-1282, 1972

[83] Murphy A B, "A comparison of Treatments of Diffusion in Thermal Plasmas",

Journal of Physics D: Applied Physics, Vol. 29, pp. 1922, 1996

[84] Murphy A B and Kovitya P, "Mathematical Model and Laser-scattering Temperature Measurements of a Direct-current Plasma Torch Discharging into Air", *Journal of applied physics*, Vol. 73, pp. 4759-69, 1993

[85] Shang J J, "Computational electromagnetic-aerodynamics", J*ohn Wiley & Sons*, 2016

[86] Information regarding the open source library "Boost" can be found at: http://www.boost.org/

[87] PHOENICS is the name of a commercial CFD package developed by CHAM UK, Online help available at: http://www.cham.co.uk/phoenics/d_polis

[88] Watton J, "Fundamentals of Fluid Power Control", *Cambridge University Press*, 2009

[89] McCloy D and Martin H R, "Control of Fluid Power: Analysis and Design", *Ellis Horwood Ltd, Chichester Sussex England, New York Halsted Press*, 1980

[90] Merritt H E, "Hydraulic Control Systems", *John Wiley & Sons*, 1967

[91] Blackburn J F, "Fluid Power Control", *Mit Press*, 1969

[92] Borghi M, Cantore G, Milani M and Paoluzzi R, "Analysis of Hydraulic Components Using Computational Fluid Dynamics Models", *Proceedings of the Institution of Mechanical Engineers, Part C: Journal of Mechanical Engineering Science*, Vol. 212, pp. 619-629, 1998

[93] Von Mises R, "The Calculation of Flow Coefficient for Nozzle and Orifice", *VDA*, Vol. 61, pp. 21-23, 1917

[94] Stone J A, "Discharge Coefficients and Steady-state Flow Forces for Hydraulic Poppet Valves", *Journal of Basic Engineering*, Vol. 82, pp. 144-154, 1960

[95] Topham D R, "The Aerodynamics of Electric Arcs in Axial Flow", *PhD Thesis*, 1970

[96] Jianying Z, Yujing G and Hao Z, "Pressure and Arc Voltage Measurement in a 252 kV SF_6 Puffer Circuit Breaker," *Plasma Science and Technology*, Vol. 18, pp. 490, 2016

[97] Yan J D, Han S M, Zhan Y Y, Zhao HF and Fang M T C, "Computer Simulation

of the Arcing Process in High Voltage Puffer Circuit Breakers with Hollow Contacts", *18th Symposium on Physics of Switching Arcs*, *Bmo Czech Republic*, pp. 99-108, 2009

[98] DeWit C C, Olsson H, Astrom K J and Lischinsky P, "A New Model for Control of Systems with Friction", *IEEE Transactions on Automatic Control*, Vol. 40, pp. 419-425, 1995

[99] Yoshioka Y, Natsui K I and Tsukushi M, "A Method and Applications of a Theoretical Calculation for On-load Pressure Rises in Puffer Type Gas Circuit Breakers", *IEEE Transactions on Power Apparatus and Systems*, Vol. 3, pp. 731-737, 1979

[100] Kim J B, Yeo C H and Yoshioka Y, "Effects of Various Factors on Gas Blast Characteristics of Auto-expansion Type Gas Circuit Breaker", *IEEE Transactions on Power Delivery*, Vol. 25, pp. 1538-1546, 2010

[101] Tuma D T, "A Comparison of the Behavior of SF_6 and N_2 Blast Arcs Around Current Zero", *IEEE Transactions on Power Apparatus and Systems*, Vol. 6, pp. 2129-2137, 1980